

An Investigation on the Influence of Stumbling Loads on  
Femoral Fracture Risk, using a Novel Gradient Enhanced Quasi-  
Brittle Finite Element Model

by

Ifaz T. Haider

A thesis submitted to the Faculty of Graduate and Postdoctoral Affairs in  
partial fulfillment of the requirements for the degree of

Doctor of Philosophy

in

Mechanical Engineering

Carleton University

Ottawa, Ontario

© 2016, Ifaz T. Haider

## Abstract

Stumbling is associated with large hip contact forces, but it remains unclear whether these events contribute to osteoporotic hip fracture risk. We hypothesized that stumbling may increase risk, either causing fracture directly, or damaging the femur leaving it susceptible to future loading. This hypothesis can be tested *in-silico*, but previously published finite element (FE) models are susceptible to large errors in predicted fracture load and pattern. We developed and validated a novel gradient enhanced quasi-brittle damage model, for improved fracture prediction, and used the model to assess the influence of stumbling on fracture risk. Preliminary FE models were used to explore relevant physics and boundary conditions (BC's) needed to accurately model the femur in fall and stumbling configurations. The study investigated the influence of different BCs, viscoelasticity, inertial dynamics, and biphasic (pore fluid) effects; the potential importance of these phenomenon had been discussed, but not well-explored, in literature. After implementation, the gradient enhanced quasi-brittle damage model was validated through experimental testing. Average fracture load prediction error was 9.6%, compared to 10%-20% errors reported in previous models and fracture pattern was correctly predicted for all cases, compared to the 60-80% accuracy of previous models. This validated model predicted that four of six specimens had a moderate risk of fracture due to stumbling alone, and risk increased significantly with simulated advanced osteoporosis. The model also predicted compaction of the subcapital region, a pattern consistent with impacted fractures observed in clinical settings. Finally, we investigated if progressive damage accumulation from combinations of stumble and fall could increase fracture risk. Most specimens were resilient to accumulated damage and only one experienced reductions in strength (5-15%) from repeat loading. However, two specimens

experienced moderate (20-30%) increase in fracture load, for some load cases; this was a novel finding. In these cases, initial damage accumulation caused the load to be more evenly distributed upon subsequent loading events. These results suggest that stumbling alone can result in hip fracture and therefore future preventative intervention strategies may be more effective if they target both fall and stumbling induced fractures.

## Acknowledgements

I would like to thank my supervisors Dr. Hanspeter Frei and Dr. John Goldak for their continued guidance, encouragement, and support in this work. I have learned a lot working with these two exceptional researchers, and this project would not have been possible without them. I would also like to thank Dr. Andrew Speirs, who also provided invaluable guidance throughout this project.

I would like to thank the staff at Carleton University. In particular, David Raude and Steve Truttmann for their assistance and guidance on using the material testing equipment safely and efficiently. Thanks to Alex Proctor and Ian Lloy, who manufactured the test fixture used in Chapter 5 and advised me on its design. I would also like to thank the IT staff, Neil MacFayden and Bruce Johnston, who helped me recover from a particularly devastating hard drive failure.

Finally, I would like to thank staff at the Ottawa Hospital and the University of Ottawa for their invaluable support in this project. Thank you to thank Claudine Séguin and Shannon Goodwin at the Division of Clinical and Functional Anatomy, who helped us acquire the cadaveric specimens used in this research. Thanks to Dr. Paul Beaulé, who consulted with us on the alignment techniques discussed in Chapter 4, and also collaborated with us on two exciting projects. While not reported in this thesis, these projects yielded valuable experience that helped me with this work.

A final thanks to the Department of Mechanical and Aerospace Engineering, at Carleton University, who provided me with scholarships and teaching opportunities, and to the Natural Sciences and Engineering Research Council of Canada, who funded this work.

## Table of Contents

Abstract.....	I
Acknowledgements.....	III
Chapter 1: Introduction.....	1
1.1. Objectives and Structure of the Thesis.....	4
Chapter 2: Theory and Background.....	7
2.1. The Mechanical Environment of the Hip.....	7
2.1.1. Anatomy of the Hip Joint.....	7
2.1.2. Fall loads and Hip Fracture Risk .....	9
2.1.3. Hip Contact Forces .....	11
2.1.4. Estimation of Muscle Forces .....	16
2.2. Behaviour and Material properties of Bone .....	19
2.2.1. Structure and Composition of Bone.....	19
2.2.2. Mechanical Properties of Bone.....	21
2.2.3. Damage accumulation in bone.....	24
2.2.4. Osteoporosis and its Diagnosis .....	26
2.3. Computer Modelling of the Proximal Femur.....	27
2.3.1. An overview of patient-specific FE modelling.....	28
2.3.2. A Biphasic Model of Bone .....	29
2.3.3. Modelling Dynamic Effects.....	31
2.3.4. A Gradient-Enhanced Damage Model for Bone.....	33
Chapter 3: Simulation of Fall Loading: Impact of BCs and Multiphysics Effects on In-Vitro Investigations of Femoral Fracture Strength.....	38
3.1. Introduction .....	38
3.2. Methods.....	40
3.2.1. Developing a Specimen-Specific FE model .....	40
3.2.2. Effects of Different Fall Boundary Conditions.....	41
3.2.3. Multiphysics Effects .....	42
3.3. Results .....	45
3.3.1. Effects of Different Fall Boundary Conditions.....	45
3.3.2. Multiphysics Effects .....	47

3.4.	Discussion .....	50
3.4.1.	Effects of Different Fall Boundary Conditions.....	51
3.4.2.	Multiphysics Effects .....	52
Chapter 4: Simulation of Physiological Loading: Impact of Muscle Forces and Femoral Alignment on In-Vitro Investigations of Femoral Fracture Strength in Stumbling Configuration .....		55
4.1.	Introduction .....	55
4.2.	Methods.....	57
4.2.1.	Influence of Muscle Forces.....	57
4.2.2.	Influence of Femoral Alignment Errors.....	60
4.3.	Results .....	64
4.3.1.	Influence of Muscle Forces.....	64
4.3.2.	Influence of Alignment Errors .....	65
4.4.	Discussion .....	69
4.4.1.	Influence of Muscle Forces.....	69
4.4.2.	Influence of Alignment Errors .....	70
Chapter 5: Development and Validation of a FE model to predict bone fracture using a Quasi-brittle damage model.....		74
5.1.	Introduction .....	74
5.2.	Methods.....	76
5.2.1.	Developing a Specimen-Specific FE model .....	76
5.2.2.	Experimental Validation .....	78
5.3.	Results .....	81
5.4.	Discussion .....	89
Chapter 6: Investigation of Risks due to Physiological loading and Damage Accumulation .....		93
6.1.	Introduction .....	93
6.2.	Methods.....	95
6.2.1.	Stumbling Loads and the Effects of Worsening Osteoporosis .....	95
6.2.2.	Effects of Previous Damage Accumulation on Fracture Load and Pattern .....	97
6.3.	Results .....	97
6.3.1.	Stumbling Loads and the Effects of Worsening Osteoporosis .....	97
6.3.2.	Effects of Previous Damage Accumulation on Fracture Load and Pattern .....	99

6.4. Discussion .....	104
6.3.3. Stumbling Loads and the Effects of Worsening Osteoporosis .....	104
6.3.4. Effects of Previous Damage Accumulation on Fracture Load and Pattern .....	105
Chapter 7: Summary .....	109
7.1. Summary of Contributions to the Field.....	113
7.2. Future work .....	115
References.....	117
Appendix A: Verification of the Gradient Enhanced Quasi-Brittle Finite Element Code .....	139
Appendix B: Mesh Sensitivity .....	166
Appendix C: Visualized Damage Patterns from Repeated Loading Scenarios .....	168

## List of Tables

Table 1 Mean and standard deviation (SD) of neutral femoral alignment angles measured from 9 implanted patients. ....	15
Table 2 Anisotropic Viscoelastic Properties of Bone .....	23
Table 3 Summary of simulations performed their objectives, and model parameters.....	44
Table 4. Twenty seven trials used to investigate the effect of small alignment errors on fracture load.....	62
Table 5 Effects of alignment error on FE computed fracture load for specimen 2 and 3.....	66
Table 6 Comparison between experimentally measured and FE predicted fracture load.....	81
Table D-1 Summary of predicted forces, in muscles that cross the hip.. ....	174
Table D-2 Summary of predicted forces, in muscles that do not cross the hip.. ....	176

## List of Figures

Figure 1 Radiograph of an atypical fracture. ....	2
Figure 2 The human hip. ....	8
Figure 3 The proximal femur. ....	9
Figure 4 Typical orientation of a femur during a sideways fall.....	10
Figure 5 Boundary conditions commonly used to represent fall loading. ....	11
Figure 6 Peak hip contact forces and normalized load profile from Bergman et al. ....	12
Figure 7 Hip contact forces from stumbling. ....	12
Figure 8 Femur coordinate system used for <i>in-vivo</i> measurement of hip contact forces.. ....	13
Figure 9 Coordinate system of the left femur as defined by Bergmann et al. ....	15
Figure 10 A typical link-segment model for the lower extremity. ....	17
Figure 11 The microstructure of cortical bone.. ....	20
Figure 12 Microstructure of trabecular bone. ....	21
Figure 13 Experimental investigation of viscoelasticity.....	23
Figure 14 Images of micro damage in cortical bone.....	24
Figure 15 Results of a tensile test of trabecular bone.. ....	25
Figure 16 Finite element model of a femur. ....	29
Figure 17 Minimum principal strain for three boundary conditions.....	45
Figure 18 Maximum principal strains for Case I.....	46
Figure 19 Minimum principal strains for Case I.....	46
Figure 20 Failure loads and peak maximum and minimum principal strains for three BC cases investigated. ....	47
Figure 21 Normalized time history of peak maximum principal strain, located at the inferior aspect of the femoral head.. ....	48

Figure 22 Minimum principal strains from trabecular viscoelasticity model compared to linear elastic model. ....	49
Figure 23 Anatomical model with muscle insertion points and load directions. ....	59
Figure 24 Distribution of minimum principal strain due to stumbling loads.. ....	65
Figure 25 Average femoral AV, AD and FL angles achieved by visual orientation, compared to target angles. ....	67
Figure 26 Average and peak errors due to visual alignments. ....	68
Figure 27 Experimental Setup. ....	79
Figure 28 Correlation between measured and predicted fracture loads.....	82
Figure 29 Experimentally determined fracture pattern and corresponding load-displacement measurement. ....	83
Figure 30 Cadaveric specimen 1 before and after testing.....	84
Figure 31 Experimentally determined fracture pattern compared to FE predicted fracture pattern for Specimen 2.. ....	84
Figure 32 Experimentally determined fracture pattern compared to FE predicted fracture pattern for Specimen 3. ....	85
Figure 33 Experimentally determined fracture pattern compared to FE predicted fracture pattern for Specimen 4.. ....	85
Figure 34 Experimentally determined fracture pattern compared to FE predicted fracture pattern for Specimen 5. ....	86
Figure 35 Experimentally determined fracture pattern compared to FE predicted fracture pattern for Specimen 6. ....	86
Figure 36 Comparisons of CT scans before fracture, after fracture, and FE predicted fracture patterns.....	88
Figure 37 Risk of fracture during stumbling for specimens at original and degraded bone density levels.. ....	98
Figure 38 FE predictions of fracture load compared to T-score estimated with vBMD measured at the femoral neck.....	99
Figure 39 Percent difference in fracture load for binary loading cases compared to their equivalent single-event load case.....	100
Figure 40 Pattern of damage distribution from load Case S compared to Case S-S for Specimen 6.....	101
Figure 41 Pattern of damage distribution from load Case F compared to Case S-F for Specimen 5.....	102
Figure 42 Patterns of damage accumulation after the first stumbling event of Case S-S.....	103
Figure A- 1 Dimensions and BCs of simulated test coupon used for code verification. ....	140
Figure A-2 Damage evolution pattern predicted by the gradient-enhanced FE code implemented in this thesis compared to previously published simulation results.....	141

Figure B-1 Specimen 6 modeled with three different mesh densities. ....	166
Figure B-2 Influence of mesh refinement on FE predicted fracture load. ....	167
Figure C-1 Damage accumulation patterns for Specimen 1. ....	168
Figure C-2 Damage accumulation patterns for Specimen 2. ....	169
Figure C-3 Damage accumulation patterns for Specimen 3.. ....	170
Figure C-4 Damage accumulation patterns for Specimen 4. ....	171
Figure C-5 Damage accumulation patterns for Specimen 5. ....	172
Figure C-6 Damage accumulation patterns for Specimen 6. ....	173
Figure E-1 Equipment used for specimen alignment.....	178
Figure E-2 Schematic representation of landmark selection.. ....	179

## Chapter 1: Introduction

Osteoporosis is a metabolic disease characterised by low bone mineral density and increased bone fragility in patients. In Canada, osteoporosis affects approximately one in four women and one in eight men over the age of 50 [1]. These patients have a high risk of suffering osteoporotic fractures, which lead to an increased mortality risk and a decreased quality of life. The rate of complications is particularly high in hip fractures compared with other types of fracture and 20-35% of all patients die as a result of comorbidities within the first year. 20-60% of the patients suffering an osteoporotic hip fracture are unable to recover baseline function within the first year [2] and after six years, approximately 30% of hip fracture patients remain bedridden [3]. For women, osteoporotic fractures result in more hospitalized days than heart attack, breast cancer, or diabetes [3]. Based on 2007 data, direct and indirect costs of osteoporosis and osteoporotic fractures in Canada was estimated at \$2.3 billion, and is likely to rise as the population ages [4].

To help combat the dangers of osteoporotic fracture, patients who are identified at risk are most commonly treated with bisphosphonates. These medications bind to hydroxyapatite crystals in the bone and inhibit their breakdown [5], [6]. However, as with most other pharmacological treatment options, bisphosphonates are associated with side effects such as hypocalcaemia and osteonecrosis of the jaw [7]. In addition, while bisphosphonate therapy is effective at maintaining bone mass and reducing short term risk of bone fractures [8], long term use of these medications have been shown to increase the risk of suffering atypical fractures, i.e., fractures occurring in what are normally the strongest sections of the bone (Figure 1) [9], [10]. The pathophysiology of these fractures is not fully understood, but it is hypothesized that extended use of bisphosphonates inhibits bone repair, allowing microdamage to accumulate and thus weaken the bone.



Figure 1 Radiograph of an atypical fracture. Fracture occurred at the femoral shaft (white circle), which is typically the strongest part of the bone. Image adopted from [10]

The presence of these side effects highlight the need to more accurately identify individuals who would benefit most from such treatments, i.e., those at most immediate risk of suffering an osteoporotic fracture. This can be challenging, however, as the likelihood of suffering a fracture is dependent on a number of factors including bone strength, the likelihood of suffering a fall, and the severity of the fall. In Canada, clinicians rely on statistical algorithms to predict fracture risk. These tools rely largely on patient areal bone mineral density (aBMD), which is currently the clinical gold standard for evaluating bone strength [11]. However, aBMD alone is inadequate at predicting fracture risk and approximately 44% of hip fractures occur in patients who would not be classified as high risk [12]. Many other factors influence strength, such as the shape of the bone, distribution of bone tissue, properties of bone tissue, and loading history.

Three dimensional continuum finite element (FE) models are able to better account for all of these factors, and have been shown to increase the accuracy of the prediction compared to predictions made using aBMD alone [13], [14]. However, FE modelling for the prediction of bone

fracture load remains an area of current research. Linear elastic models are often used because they can be simulated quickly, but can result in large errors between measured and predicted fracture load (up to 45%) [15], [16]. Nonlinear models perform better, but there is no apparent consensus in the literature regarding the best material/failure model to use [17]–[19].

In addition to understanding factors which contribute to bone strength, it is also necessary to understand situations which may cause bone to fail. The majority of the research has been focused on falls as the primary cause of fracture [20]–[26]. This is because most fractures are ‘associated’ with a fall, based on patient interviews or questionnaires [27], [28], and it is assumed that the patient falls and then breaks their hip from the impact. However, large forces occur in activities other than fall. For example, stair climbing may result in peak forces to up 330 percent bodyweight (%BW) [29], while stumbling may result in forces as high as 850 %BW [30]. If the patient is osteoporotic, it may be possible for these high loads to cause a spontaneous fracture, i.e., a fracture with no blunt force trauma, causing them to fall afterwards from pain or loss of joint stability. Based on the literature, it is unclear how commonly this occurs, if at all. Patient questionnaires cannot reliably answer this question; fractures and falls occur very quickly and it is difficult to perceive which occurred first. This is compounded by the fact that many elderly patients experience mild delirium and memory loss following a fracture, and are unable to accurately recall the sequence of events leading up to the fracture [31].

While observational clinical studies cannot accurately determine the prevalence of spontaneous fractures, biomechanical modelling can still be used to determine whether such fractures are possible at all. A recent study by Viceconti et al. [31] used linear FE models to predict whether spontaneous fractures were possible due to walking loads. This study predicted fracture only when the patient had both extreme osteoporosis and extreme neuromotor degradation.

However, no studies have looked at fracture risk from more extreme physiological events, such as stumbling.

Stumbling loads may also contribute to fracture risk even if the event itself does not result in immediate failure of the bone. Recent material level studies have demonstrated that the structural response of bone is history dependent [32], [33]. As bone is subject to loading, it suffers damage in the form of progressive microstructural cracking. This causes reductions in stiffness and, if damage is significant, reductions in peak load bearing capability. While healing mechanisms exist to repair this damage over time, it is plausible that repeated loading events can occur before significant repair [34]. Thus, it is plausible that a high load event may leave the bone unbroken, but damaged, and susceptible to subsequent loading events. However, this phenomenon has not been explored at the organ level.

## **1.1.Objectives and Structure of the Thesis**

The objective of this thesis is to develop and validate a novel FE model for the prediction of bone fracture, and to use that model to explore the importance of physiological loading on hip fracture risk. It is hypothesized that physiological loading may play an important role, either by causing a spontaneous fracture directly, or by damaging the femur so that it is more susceptible to fracture from subsequent loading events. The remainder of the thesis is organized as follows:

Chapter 2 details the background theory related to the study. This includes an introduction to relevant human anatomy and biomechanics, as well as detailed description of the modelling techniques investigated in future chapters.

Chapter 3 describes the first research task, which was a preliminary simulation study of factors that may influence FE modelling of femora in a fall configuration. This includes a study on the importance of physiologically realistic BCs, as well as the influence of multiphysics effects on simulated fracture loads. The goal of this work was to ensure that the *in-vitro* models developed and used in future chapters represented the *in-vivo* condition during a fall.

Chapter 4 is a second preliminary study, this time intended to explore issues associated with FE modelling of femora under physiological loads. This chapter looked at two factors that were not well explored in the literature: (I) the effects of muscle forces on FE prediction of fracture load, and (II) the sensitivity of fracture load predictions to specimen alignment errors. Again, the purpose of this work was to ensure that future *in-vitro* tests and models, in physiological load configurations, were accurate representations of the *in-vivo* condition.

Chapter 5 used the results of these preliminary investigations in order to develop and validate a model for the prediction of femoral fracture load and fracture pattern. Specimen-specific FE models were developed and validated through experimental testing. FE predicted fracture load and pattern was compared to experimental findings, and the overall performance of the model was compared to similar studies in the literature.

Chapter 6 adopted the final model developed and validated in Chapter 5, in order to study the circumstances surrounding hip fracture. This chapter investigated the plausibility of suffering a spontaneous fracture, and the influence of previous damage accumulation on fracture pattern and fracture risk from subsequent high risk events (stumbling and fall).

Finally, Chapter 7 summarizes the important outcomes and conclusions from the previous chapters' works. In particular, the contents of this chapter describes how the findings of this

thesis have advance the field of research. The thesis concludes with recommendations for future work.

## **Chapter 2: Theory and Background**

Before further discussion of the proposed research, a brief introduction to human anatomy and biomechanics, and a review of the current literature is presented. This chapter is divided into three sections. Section 2.1 describes the mechanical environment of the femur, it provides a brief overview of relevant anatomy and discusses important loading conditions such as fall, physiological hip contact forces, and muscle loads. Section 2.2 then describes the behavior of bone as a material, and how that behavior is modelled mathematically. Finally, section 2.3 describes how the information from the previous sections can be combined in order to develop realistic FE models of bone. This section describes techniques that are commonly used in the literature, but also provides detailed descriptions of all computational techniques used in this thesis, many of which are not yet commonly used for modelling bone.

### **2.1. The Mechanical Environment of the Hip**

#### **2.1.1. Anatomy of the Hip Joint**

The hip joint, shown in Figure 2, connects the torso to the legs. This synovial ball and socket joint provides the wide range of motion required for human locomotion. The joint is also responsible for the transfer of weight from the upper body to the supporting ground. As a simple joint, the hip involves interaction of two bones: the acetabulum and the femur, or thigh bone.

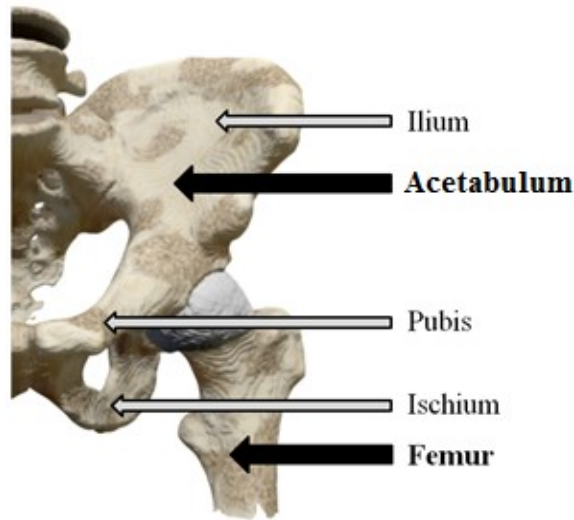


Figure 2 The human hip.

The convex aspect the hip joint is formed by the femur, shown in Figure 3; most 'hip' fractures occur at the femur, making this bone the focus of this investigation. The femur is a long, strong bone which provides structural support for the thigh. Like all other long bones, it consists of a cylindrical shaft (diaphysis) and two rounded ends (epiphyses). The proximal epiphysis begins at the head, which forms the  $\frac{2}{3}$ <sup>rd</sup>s spherical region that mates with the acetabulum. Two protrusions, the greater and lesser trochanter, provide attachment points for tendons and leverage for thigh muscles to rotate the femur. The head is connected to the shaft of the femur through the neck, which is on average approximately 1.5 cm long and forms an angle of approximately  $125^\circ$  with the shaft, but varies from subject to subject. The shaft, as the name suggests, is the long cylindrical section which forms the body of the femur. The distal epiphysis, which forms part of the knee joint, will not be discussed in detail as it is not relevant to hip fracture [35]–[37].

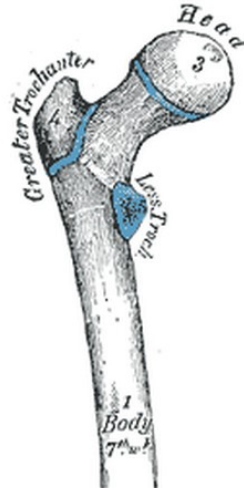


Figure 3 The proximal femur. Image modified from [35]

### 2.1.2. Fall loads and Hip Fracture Risk

As mentioned in the introduction, hip fracture is typically associated with blunt force trauma caused by falling. Studies have shown that configuration of the femur during a fall has a large impact on the predicted fracture load [38]. Thus, in order to get relevant results from finite element models or *in vitro* testing, it is necessary to understand which types of falls are most dangerous and how the femur is oriented during those falls.

Survey studies of hip fracture patients have identified a number of factors which contribute to fracture risk. Falls that result in an impact on the greater trochanter increase risk by up to 48 times, and sideways falls have 3 times greater risk versus falls in all other directions. In addition, the risk of fracture is up to three times lower when the patient is able to break their fall by impacting the hand or knee first [22], [39].

The typical configuration of a sideways fall places the shaft of the femur at a  $10^\circ$  angle with the ground, and the head rotated  $15^\circ$  as shown in Figure 4 [40], [41]. Peak forces may be as

high as 8.5 kN for a 57 kg patient [42], though this will vary greatly from case-to-case depending on body weight, thickness of trochanteric soft tissue [24], [43] stiffness of the ground, and protective behaviour of the patient [44], and muscle activation [25].

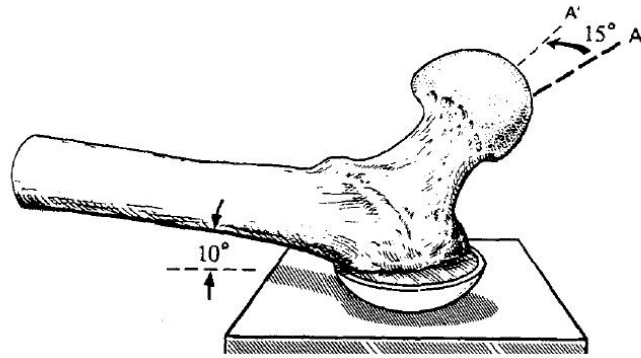


Figure 4 Typical orientation of a femur during a sideways fall. Image modified from [40].

While the orientation and loads during a fall are well documented, there is little agreement in the literature on appropriate boundary conditions (BC's) needed in order to replicate the conditions of a fall, *in-vitro*. Boundary conditions are typically applied to the greater trochanter (GT), femoral shaft (FS) and femoral head (FH), and three commonly used cases are shown in Figure 5 below. Case I was adopted from Keyak et al. [45] where the FS and GT were fully constrained to rotation and translation, while the FH was loaded. Case II was adopted from Courtney et al. [40] where the FS was only free to rotate in the coronal plane and translate along the shaft axis in the coronal plane. Finally, case III was adopted from Roberts et al. [46] and de Bakker et al. [21], where the FS was only free to rotate and translate in a cranio-caudal direction in the coronal plane. The FH was only free to rotate in the coronal plane and load was applied to the GT. It is difficult to determine which of the three cases best represent the *in-vivo* condition during a fall, and to the best of the author's knowledge no study has compared differences in fracture estimates due to differences in selected boundary conditions.

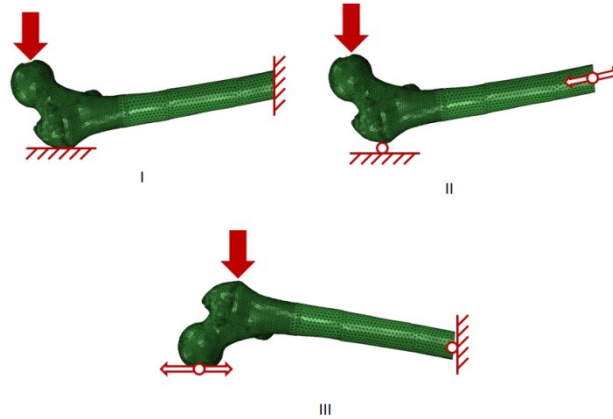


Figure 5 Boundary conditions commonly used to represent fall loading. (I) the FS and GT fully constrained to rotation and translation, while the FH is loaded; (II) the FS only free to rotate in the coronal plane and translate along the shaft axis in the coronal plane. (III) the FS free to rotate and translate in the cranio-caudal direction in the coronal plane, the FH free to rotate in the coronal plane, with load applied to the GT.

### 2.1.3. Hip Contact Forces

In addition to fall loading, bones are also subject to large loads during routine activities. The hip contact, or bone-on-bone, force has been studied in great detail by Bergman et al. [29] who collected data from telemetric hip implants from four subjects performing a number of routine activities such as walking, sitting, standing, and stair climbing. To the best of the author's knowledge, this is the most comprehensive collection of *in-vivo* contact force data, and is the most commonly cited source for loading directions and magnitudes used *in-vitro* studies of the proximal femur [47]–[49].

As shown in Figure 6 below, the highest contact forces from voluntary activities occurred during stair climbing, with peak forces of approximately 330% bodyweight (BW), varying cyclically with each step.

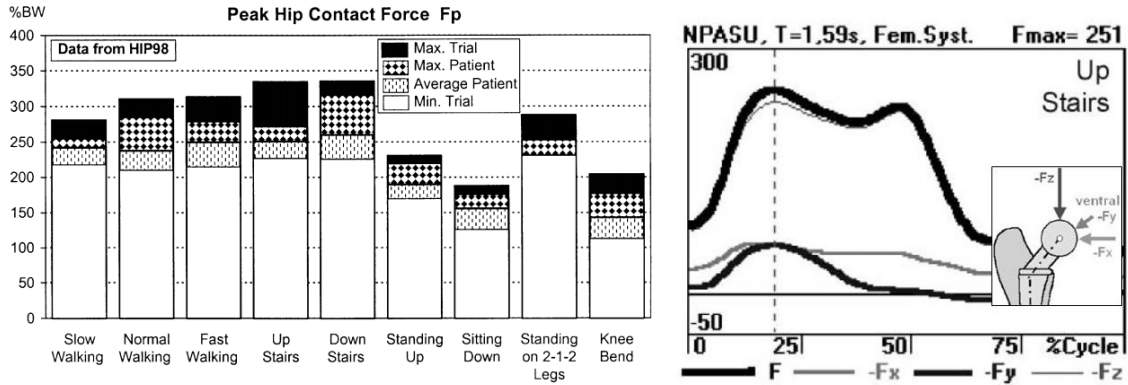


Figure 6 Peak hip contact forces (left) and normalized load profile (right) from Bergman et al. [29] Max Trial = Highest value from all trials. Max. Patient = Highest average from all patients. Average patient = value from one patient whose gait was identified as ‘typical’. Min. Trial=Lowest value from all trials. The highest forces occurred while climbing up or down stairs.

These studies also measured another important loading case. During a few trials, patients lost their balance and began to stumble. In response, they took several rapid steps to regain balance and prevent a fall. During this sequence of events, the telemetric hip implants recorded extremely high forces, up to 870%BW, as shown in Figure 7 [30].

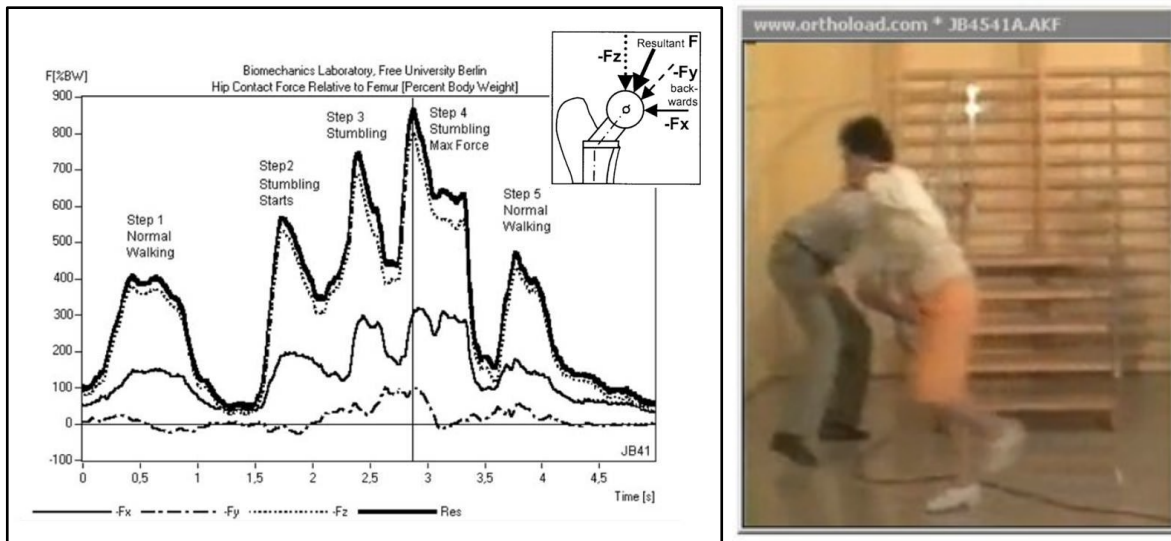


Figure 7 Hip contact forces from stumbling. At 1.5 s, the subject begins to stumble, and takes three rapid steps in order to maintain balance. These steps cause resultant hip contact forces up to 850%BW, which is significantly higher than those encountered during routine activity (Figure 6). Image adopted with modifications from [30].

In order for the data to be used meaningfully, it was important to report forces using a coordinate system that was well defined and easily reproducible. For their study, Bergman et al. [29] developed a ‘femur coordinate system’, defined using landmarks on the femoral condyles and implant center, shown in in Figure 8. As the name implies, this coordinate system rotates with the femur during motion. However, when the subject stands in the neutral position, the axes of the femoral coordinate system approximate the directions of the anatomical coordinate system, i.e., identifying the axes of the femur coordinate system is roughly equivalent to identifying the femur’s neutral position.

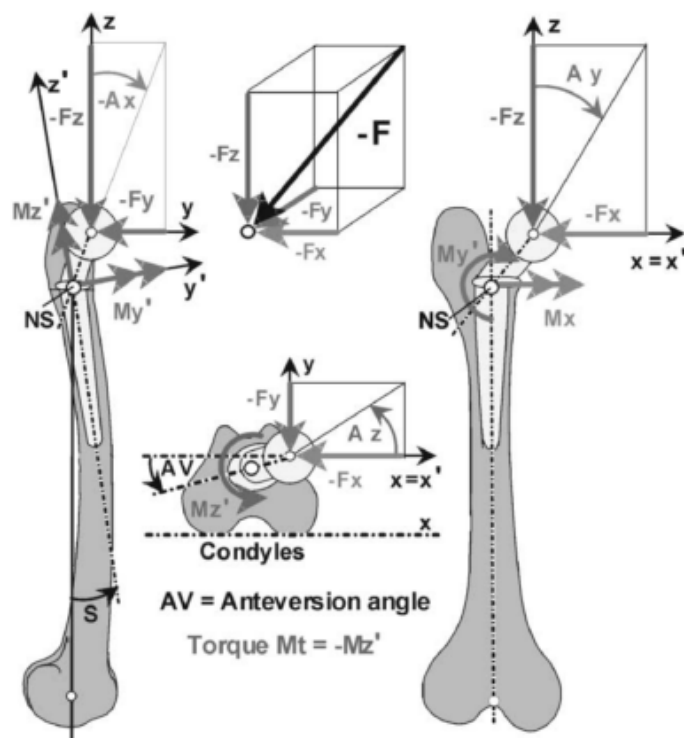


Figure 8 Femur coordinate system used for *in-vivo* measurement of hip contact forces. Axes directions were defined based on the position of the condyles as well as the center of the telemetric hip implant. Image adopted from [29].

Unfortunately, it is difficult to accurately recreate this coordinate system in an *in-vitro* study. Condyles are often unavailable, and the center of the implant (point NS in Figure 8) must be approximated, as the exact dimensions of the implant are unpublished. Noting these challenges, Bergman et al. published supplemental material describing the orientation of the proximal femur relative to the axes of their coordinate system [50]. The position of the femur was described in terms of three angles shown in Figure 9. Anteversion (AV) was reported as the angle between the medial-lateral axis and femoral neck axis, when viewed in the transverse plane. The caput-collum-diaphyseal angle (CCD) was measured between the femoral neck and the vertical axis, when viewed in the frontal plane. Finally, the shaft angle (S) was the angle between the local axis of the proximal shaft, and the vertical axes of the coordinate system.

Average angles approximating the neutral position, measured from nine patients, are reported in Table 1 [22]. Using geometry of the proximal femur alone, these angles may be measured and reproduced in order to ensure that the load direction applied during future *in vitro* studies closely match the load directions measured *in vivo* by Bergman et al. [16].

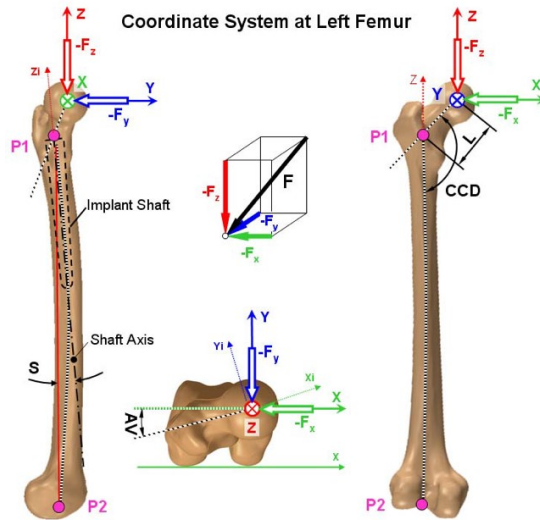


Figure 9 Coordinate system of the left femur as defined by Bergmann et al. [16]. The x-axis is the line joining the dorsal contour of the femoral condyles and the z-axis is the line joining the center of the condyles to the mid-point of the implant shaft. Image adopted from [50]

Table 1 Mean and standard deviation (SD) of neutral femoral alignment angles measured from 9 implanted patients [22].

Angle	Mean Angle [°]	Standard Deviation [°]
S	9	1.5
CCD	135	0
AV	12	11.1

#### 2.1.4. Estimation of Muscle Forces

The proximal femur is commonly modelled by applying hip contact forces, described above, to the femoral head while fully fixing the femoral shaft [48]. However, this results in large, physiologically unrealistic reaction forces at the femoral shaft. *In-vivo*, the contact forces are partially reacted by muscle forces which are distributed throughout the femur. Including these muscle forces in the model may result in a more realistic stress/strain distribution pattern. Because it is difficult to measure individual muscle forces *in-vivo*, these forces are instead calculated using biomechanical modelling.

First, a link-segment model (Figure 10) is used to determine joint reaction forces  $\{\overline{JRF}\}$  and joint reaction moments  $\{\overline{JRM}\}$ . As described in equations 1 and 2 below, these represent the combined effects of bone-on-bone contact and muscles that cross the joint.

$$\{\overline{JRF}\} = \{\overline{CF}\} + \sum_{i=1}^N \{\overline{FM}_i\} \quad (1)$$

$$\{\overline{JRM}\} = \sum_{i=1}^N \{\overline{R}_i\} \times \{\overline{FM}_i\} \quad (2)$$

Where  $\{\overline{CF}\}$  is the bone-on-bone contact force at a joint,  $\{\overline{FM}_i\}$  is the force of the  $i^{th}$  muscle which crosses the joint,  $\{\overline{R}_i\}$  is the moment arm of the  $i^{th}$  muscle about the joint center of rotation, and  $N$  is the total number of muscles crossing the joint. In the general case, these are all three dimensional vectors.  $\{\overline{JRF}\}$  and  $\{\overline{JRM}\}$  are calculated using the equations of motion below:

$$\Sigma\{\overline{\mathbf{F}}_k\} = m_k\{\overline{\mathbf{a}}_k\} \quad (3)$$

$$\Sigma\{\overline{\mathbf{M}}_k\} = [I_k]\{\overline{\boldsymbol{\alpha}}_k\} \quad (4)$$

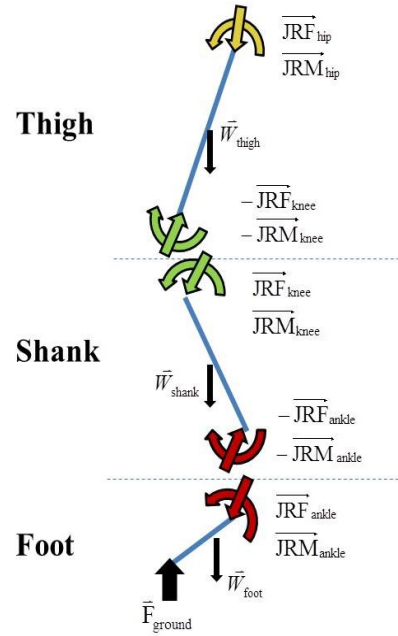


Figure 10 A typical link-segment model for the lower extremity. In the most general case, all force and moment vectors are three dimensional.

Where  $\{\overline{\mathbf{F}}_k\}$  and  $\{\overline{\mathbf{M}}_k\}$  are the 3D vector forces and moments acting on the  $i^{th}$  body segment,  $m_k$  and  $[I_k]$  are the segment mass and second moments of inertia, and  $\{\overline{\mathbf{a}}_k\}$  and  $\{\overline{\boldsymbol{\alpha}}_k\}$  are the segment's linear and angular acceleration, respectively. In order to solve Equations 3 and 4 for each body segment, an inverse dynamics approach is typically used [47], [51], [52]. Segment accelerations are measured by placing optical trackers on a subject and recording their motion during the activity in question. Segment masses and moments of inertia can be estimated using the patient's body weight and standard anthropomorphic data [53]. Finally, a force plate is used to measure ground reaction force. Equations 3 and 4 are solved using a 'bottom-up' approach; the only unknowns for the foot segment are ankle reaction force and moment. A solution for ankle reaction force and moment then allows the shank segment to be considered, and used to solve for

knee reactions and moments. This procedure is followed 'up the chain' until all unknown joint reactions are solved.

Once joint reaction forces and moments are known, a more detailed musculoskeletal model is used to solve for individual muscle forces. Muscles are typically represented as straight lines passing from origin to insertion, though muscles with large attachment areas are often represented by multiple lines of action [47]. Individual muscle forces can be calculated by considering Equation 2. However, due to the large number of muscles crossing each joint, this equation is underdetermined. To obtain a unique solution, it is assumed that muscle activation occurs in some optimal pattern, and the values for muscle forces can be obtained by minimizing an objective function subject to Equation 2 as a constraint. For analysis of lower extremities, the objective function is most commonly taken to be the sum of muscle forces cubed:

$$O = \sum_{i=1}^N \left( \frac{\{FM_i\}}{PCSA_i} \right)^3 \quad (5)$$

Where  $O$  denotes the objective function, to be minimized, and  $PCSA_i$  is the physiological cross sectional area of the  $k^{\text{th}}$  muscle, which are usually estimated from cadaver measurements [54].

The technique described above has successfully been used to predict muscle forces during walking, with good agreement between predicted muscle forces and *in-vivo* EMG measurements [55]. Predicted hip contact forces also agree with contact forces measured *in-vivo* [47], [56].

While muscle forces can be computed using this technique, it remains unclear whether they are important for accurate predictions of bone fracture. Previous experimental [57]–[59] and simulation [60], [61] studies have reported that inclusion of muscle loads may affect strains in the shaft and intertrochanteric region of the femur. Cristofolini et al. [48] reported small

differences in the strains in the head-neck region, but used walking as their only load case. To the best of the author's knowledge, no studies have attempted to estimate muscle forces during stumbling.

## **2.2. Behaviour and Material properties of Bone**

The previous sections described the femur and its mechanical environment, at the organ level. In order to perform realistic engineering analysis, however, it is also necessary to understand the behaviour of bone at the material level.

### **2.2.1. Structure and Composition of Bone**

Bone is a composite material. It consists of a mineral matrix, providing bone with its rigidity and compressive strength, reinforced by collagen fibrils, which enhance toughness and tensile strength. Bone tissues are classified into two types: cortical and trabecular. Cortical bone is a dense, solid mass with little porosity. It is found on the outer wall of all bones, and makes up most of the diaphysis of long bones. Trabecular bone, in contrast, is a porous 'spongy' tissue which makes of the majority of the volume of the epiphysis [12,13].

At the microstructural level, cortical bone is built up in layers called lamellae, as shown in Figure 11 below. Each lamella is approximately 5 microns thick with the exact arrangement differing based on location. The main structural unit of cortical bone is the osteon, which are approximately 200  $\mu\text{m}$  wide cylindrical structures made from concentric lamellae. The region between osteons is occupied by interstitial bone, which are remnants of osteons partially absorbed during bone remodelling. Finally, the inner and outer surface of cortical bone is composed of several layers of circumferential lamellae, wrapping around the bone uninterrupted. Blood is

supplied through a series of canals, with Haversian canals, running parallel through the center of each osteon, and Volkmann canals, running transverse [12,13].

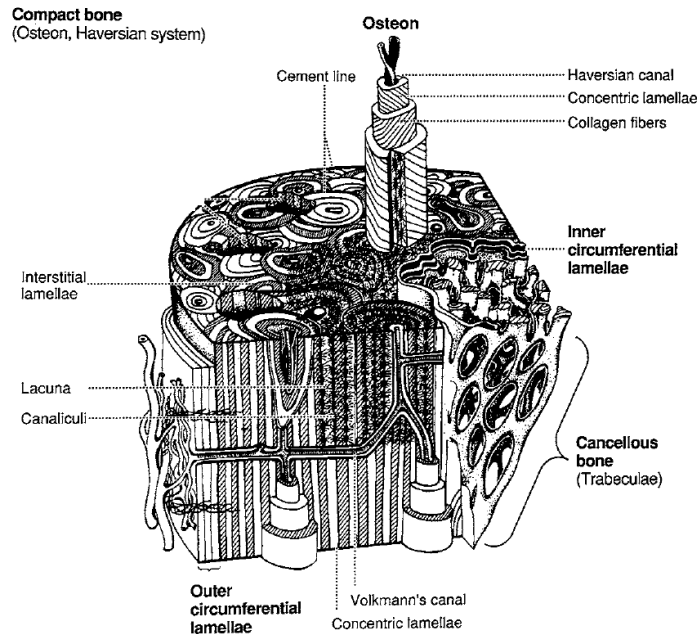


Figure 11 The microstructure of cortical bone. Image modified from [62].

The microstructure of trabecular bone is very different to that of cortical bone. This highly porous tissue is made up of a network of rod and plate-like structures, roughly 200  $\mu\text{m}$  thick, known as trabeculae (Figure 12). In contrast to cortical bone, these trabeculae are made of up shallow crescent structures, called hemiosteons, separated by interstitial bone, also shown in Figure 12 below. The pores of trabecular bone are occupied by bone marrow, the properties of which vary with location. In long bones, the epiphyseal ends are filled primarily with red marrow which is a viscous ( $\sim 400$  cP) non-Newtonian fluid. In contrast, the diaphysis is filled with fatty yellow marrow, a Newtonian fluid with much lower ( $\sim 40$  cP) viscosity [63].

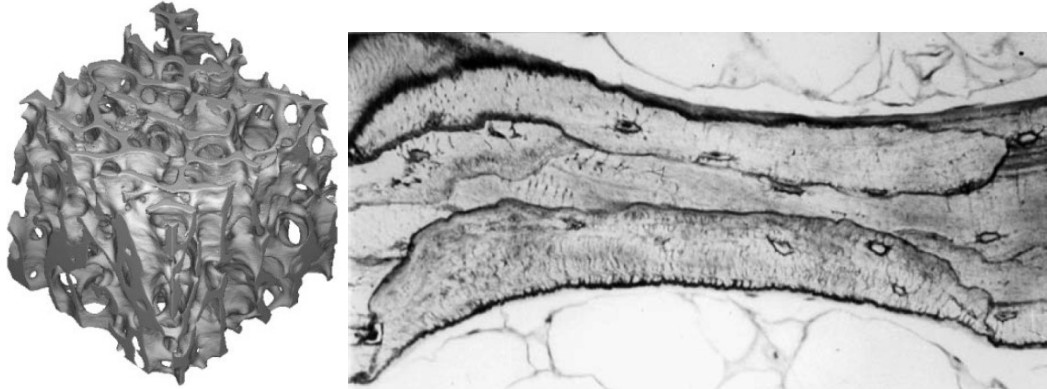


Figure 12 Microstructure of trabecular bone. Rod and plate-like trabeculae form a porous network (left)[64]. Each trabeculae is made up of crescent-like hemiosteons separated by interstitial bone (right) [62].

### 2.2.2. Mechanical Properties of Bone

Like many composites, the mechanical properties of bone can be very complex. At the continuum level, bone is an anisotropic, viscoelastic solid, whose material properties can vary significantly from patient-to-patient and site-to-site. The following sections discuss the current literature on predicting the stiffness and strength of bone.

The apparent-level stiffness of bone material shows a strong dependence on density. The relationship between density ( $\rho$ ) and elastic modulus ( $E$ ) is usually described using an exponential relationship, as per Equation 6:

$$E = A \rho^B \quad (6)$$

Where  $A$  and  $B$  are experimentally determined parameters. It is difficult to select appropriate values for these parameter as there are large inter-study differences in the reported values, even among studies which share the same experimental technique [65]. The reasons for these differences are not fully understood, though the anatomic location of the sample appears to play

a role [66]. For this research, the relationship determined by Morgan et al. [66], based on samples taken at the femoral neck, are used (Equation 7).

$$E = 6.950 \rho^{1.49} \quad (7)$$

Where  $E$  is the elastic modulus in GPa and  $\rho$  is the apparent density of bone in  $\text{g/cm}^3$ , i.e., the ratio of specimen mass to the volume enclosed by the external surfaces, including voids. This relationship has been used in previous FE studies to obtain good agreement between FE predicted and experimentally measured strains at the proximal femur [67].

Bone is also a viscoelastic material, and has been show to exhibit time-dependent material properties even at loads below the yield strain [33], [68]. Iyo et al. [68] found that the experimentally observed relaxation of cortical bone could be well explained with a linear combination of two Kohlraush-Williams-Watts functions (Equation 8).

$$E(t) = E_0 \left\{ A_1 \exp \left[ - \left( \frac{t}{\tau_1} \right)^\beta \right] + (1 - A_1) \exp \left[ - \left( \frac{t}{\tau_2} \right)^\gamma \right] \right\} \quad (8)$$

Where the elastic modulus  $E(t)$  at time  $t$ , is a function of a fast relaxation modulus ( $\tau_1$ ) a slow relation modulus ( $\tau_2$ ) and three experimental constants ( $A_1, \beta, \gamma$ ). As shown in Table 2, the fast relaxation process is relatively isotropic, but the slow process was found to vary depending on whether the bone sample was taken parallel (P) or normal (N) to the long axis of the bone (Figure 13).

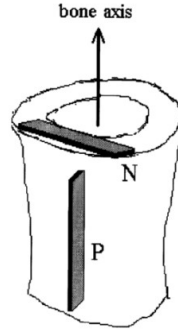


Figure 13 Experimental investigation of viscoelasticity. Viscoelastic parameters were measured for samples taken parallel (P) and normal (N) to the long axis of bone [68].

Table 2 Anisotropic Viscoelastic Properties of Bone

	$A_I$	$\tau_1$	$\tau_2$	$\beta$	$\gamma$
P	0.08	49	$9.3 \times 10^{-6}$	0.28	0.35
N	0.11	50	$6.4 \times 10^{-6}$	0.26	0.37

Similarly, Guedes et al. (2006) found that the stress relaxation behaviour of trabecular bone was well described using the power law relationship given by Equation 9, with viscoelastic parameters  $\lambda=0.25$ ,  $n=0.12$ , and  $\tau_0=1$  s.

$$E(t) = E_0 \left[ 1 - \lambda \left( \frac{t}{\tau_0} \right)^n \right] \quad (9)$$

Strength of bone is another important property which must be characterized. In this regard, there is a growing consensus on the use of strain based failure criterion for both cortical and trabecular bone [70], [71]. In contrast to stiffness or yield stress, yield strain criterion for bone is isotropic and relatively homogeneous [72] and a finite element study by Schileo et al. [73] demonstrated that strain-based failure criterion are a more specific predictor of failure than stress-based criterion. The relationship between stiffness and bone density (Equation 7), implies that low density bone reaches yield and fracture strains at much lower stress values than higher density bone. In modern clinical practice, this relationship between bone density and bone fragility is used to screen high-risk patients based measurements of bone density.

### 2.2.3. Damage accumulation in bone

The properties of bone tissue, discussed in the previous section, do not remain constant throughout the loading history. As the tissue is loaded, small micro-fractures develop in the bone; these cracks have been shown to develop at loads well below the fracture load of bone [32], [33], [74], [75].

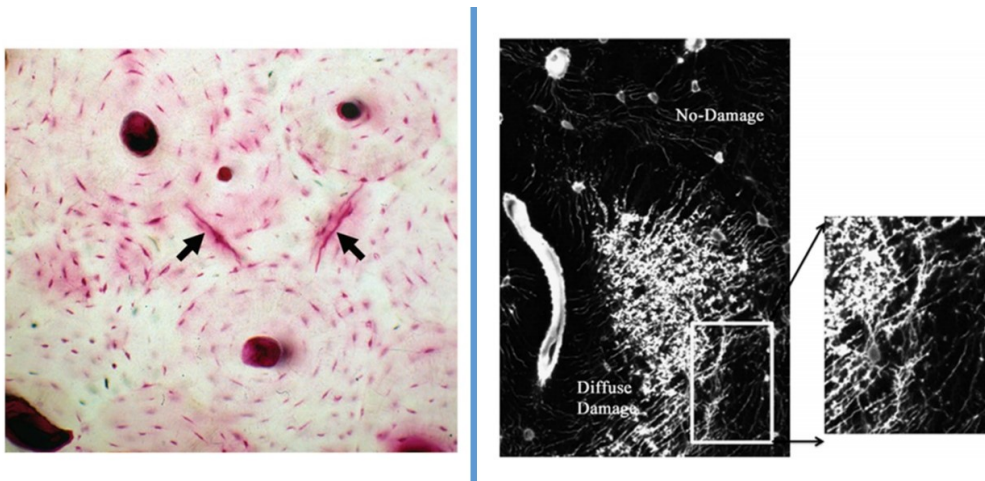


Figure 14 Images of micro damage in cortical bone. Damage can occur in the form of distinct linear cracks (left) or as a network of cracks known as 'diffuse damage'. Image adopted from [75]

The formation of microcracks reduces the effective cross sectional area of bone tissue that is available to resist a load, reducing the apparent stiffness of the material. As applied load increases, microcracks eventually coalesce into large macro cracks, and these cracks grow until failure occurs.

The mechanical effects of damage have been observed by repeatedly loading the same specimen; previous studies have shown that each successive loading results in a reduced tangent modulus [33]. Simple tensile tests (Figure 15) can also demonstrate the effects of microdamage.

As bone is loaded, the apparent stiffness gradually degrades. This behavior is particularly apparent at 70-85% of the peak load, where stiffness degradation proceeds rapidly until complete failure.

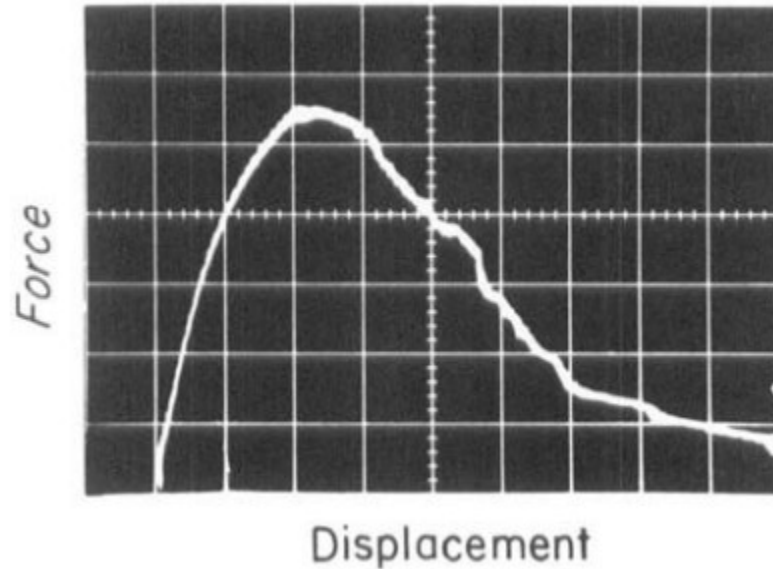


Figure 15 Results of a tensile test of trabecular bone. After 70% of peak load, stiffness degrades rapidly until complete failure. Image adopted from [76].

The constitutive relationship for this material can be well described using an isotropic damage model (Equation 10) [77]–[79]:

$$\boldsymbol{\sigma} = (1 - D)\mathbf{C}\boldsymbol{\varepsilon} \quad (10)$$

Where  $\boldsymbol{\sigma}$  and  $\boldsymbol{\varepsilon}$  are the stress and strain tensors, respectively, and  $\mathbf{C}$  is the fourth order Hookean stiffness tensor, derived from undamaged young's modulus (discussed in section 2.3) and poisson's ratio of bone. Exploiting symmetry of the stress and strain tensors, Equation 10 can be rewritten for an isotropic material as:

$$\begin{Bmatrix} \varepsilon_{xx} \\ \varepsilon_{yy} \\ \varepsilon_{zz} \\ 2\varepsilon_{yz} \\ 2\varepsilon_{xz} \\ 2\varepsilon_{xy} \end{Bmatrix} = \frac{(1-D)}{E} \begin{bmatrix} 1 & -\nu & -\nu & 0 & 0 & 0 \\ -\nu & 1 & -\nu & 0 & 0 & 0 \\ -\nu & -\nu & 1 & 0 & 0 & 0 \\ 0 & 0 & 0 & 2(1+\nu) & 0 & 0 \\ 0 & 0 & 0 & 0 & 2(1+\nu) & 0 \\ 0 & 0 & 0 & 0 & 0 & 2(1+\nu) \end{bmatrix} \begin{Bmatrix} \sigma_{xx} \\ \sigma_{yy} \\ \sigma_{zz} \\ \sigma_{yz} \\ \sigma_{xz} \\ \sigma_{xy} \end{Bmatrix} \quad (11)$$

Where  $E$  is the undamaged young's modulus (obtained from element density and Equation 7) and  $\nu$  is the poisson's ratio of bone (0.3). The damage parameter,  $D$ , is a function of the loading history. Recent studies use a quasi-brittle model [19], [80]–[82], where damage increases with increasing elastic strain:

$$D = A \cdot \varepsilon_{eq}^n \quad (12)$$

Where  $A$ , and  $n$  are experimentally determined coefficients [32], [81].  $\varepsilon_{eq}$  is a damage equivalent strain computed from components of the strain tensor.

#### 2.2.4. Osteoporosis and its Diagnosis

The previous sections have described how bone strength and damage evolution are both governed by strain. Noting the relationship between density and stiffness (Equation 7), this implies that low density bone will experience damage evolution and eventual material failure at lower stress levels than high density bone. This well accepted relationship between bone density and fragility is the basis for fracture risk screening in modern clinical practice.

Today, bone density is most commonly measured using dual x-ray absorptiometry (DEXA), a form of projection radiography which uses x-ray beams at two different energy

levels. This allows the scan to accurately correct for the effects of overlaying soft tissue and bone marrow, and is considered the ‘gold standard’ for diagnosis of osteoporosis [83]. DEXA scans measure areal bone mineral density (aBMD), i.e., bone mineral content per image area. To assess fracture risk, the measurement is compared to that of a healthy young female adult at the same anatomical location. According to World Health Organization (WHO) and International Osteoporosis Foundation guidelines, patients with BMD within 1 standard deviation of the norm are considered to have normal density, those between 2.5 and 1 standard deviation below the norm are considered to have low density (osteopenia). Finally, patients with a T-score below 2.5 are considered to have dangerously low bone density –a disease known as osteoporosis [84].

Despite its prevalence in modern clinical practice, there is evidence that aBMD alone is not an accurate tool for identifying hip fracture risk. Previous studies have found that approximately 44% of hip fractures occur in patients who would not be classified as osteoporotic [12]. Many other factors influence strength, such as the shape of the bone, distribution of bone tissue, and properties of bone tissue, and loading magnitude. These factors could be better accounted for using engineering techniques, such as patient-specific finite element modelling, which is discussed in the following section.

### **2.3. Computer Modelling of the Proximal Femur**

The previous subsections described the mechanical environment of the proximal femur (Section 2.1), and how bone behaves as a structural material (Section 2.2). This information can be used to produce physically realistic computer models, using the finite element method. The following section provides an overview of how patient specific FE models are constructed, as

well as a review of the current state-of-the-art. This thesis also investigates the use of model techniques not commonly used for bone, such as the modelling structural dynamics effects and biphasic effects; a brief overview of these techniques are provided in this section as well.

### **2.3.1. An overview of patient-specific FE modelling**

Numerous studies over the past three decades have developed and used FE models of bone [13], [14], [17], [18], [31], [45], [48], [67], [82], [85]–[94]. In this method, a discretized mesh of the patient femora is developed from 3D quantitative computed tomography (qCT) scans (Figure 16). Scans typically include a calibration phantom, a device with several regions of known mineral density. This allows the operator to develop a regression curve relating CT intensity to equivalent bone density. Using known relationships between bone material properties and density (Equation 7), each element of the model can be assigned an effective isotropic stiffness. The resulting model is then subject to boundary conditions and applied loads, and the finite element method [95] is used to calculate the stress and strain field in the bone, an example of which is shown in Figure 16.

A multitude of different models are proposed in the literature, with the primary distinguishing factor being the specific choice of failure criterion. Linear FE models are computationally inexpensive, and commonly used [15], [92]–[94], [96]. These models treat bone as a linear elastic solid, and failure is assumed to occur after a certain number of elements exceed the selected failure criterion. These models are able to accurately predict strains at low loads [67], and achieve strong correlations between FE predicted and experimentally determined failure load. Despite the strength of correlation, however, error magnitudes can remain quite large; some studies show that individual specimens have differences of up to 45% between predicted and experimentally measured fracture loads [15], [96]. To achieve better results, some

FE studies incorporate nonlinear material properties. In these studies, bone elements behave linear-elastically until a failure condition is met, at which point the element's properties are degraded, i.e., the stiffness and/or stress in the element is adjusted to account for localized failure of the bone material [17], [18], [91], [97]. However, there is currently little consensus regarding the best material model and failure criterion to use for modelling failure of the proximal femur.

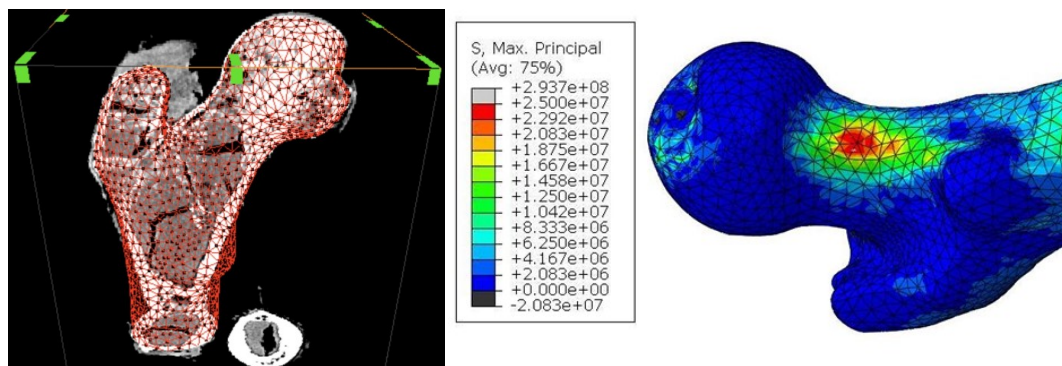


Figure 16 Finite element model of a femur. The discretized mesh is aligned with a CT scan, and assigned material properties based on element average density (left). The resulting model can be used to predict the stress and strain variations of bone when subject to loads and boundary conditions (right)

An important component of this thesis work was to investigate the influence of physics effects that are commonly neglected, or presumed negligible, in the models described above. These effects, as well as their FE implementation, are discussed in the following sections.

### 2.3.2. A Biphasic Model of Bone

The FE models discussed in the previous section treat bone as a monophasic (solid) continuum. However, bone also consists of a fluid phase. Trabecular bone, in particular, is a highly porous material filled with viscous bone marrow. High volumetric strains may cause increases in pore pressure, which may support part of the applied load causing an increase in

apparent stiffness [98]–[100]. While there is reasonable evidence demonstrating this effect at the material level [99], [101], it remains unclear whether its effects are important for whole bones under realistic loading conditions. Experimental studies have reported contradictory results [98], [102]. However, the influence of marrow on the structural response of bone can be investigated in further detail using biphasic theory, which was originally developed by Mow et al. [103], [104] for the study of articular fluid flows through cartilage. This method is described in the following paragraphs.

As a biphasic material is loaded locally, a pressure differential forms, potentially causing flow to unloaded regions with lower pressure, according to Darcy's Law:

$$\{\vec{q}\} = \frac{k [I]}{\mu} \nabla P \quad (13)$$

Where  $\{\vec{q}\}$  is the fluid flux (m/s),  $P$  is the fluid pressure (Pa),  $[I]$  is the identity matrix,  $\mu$  is the fluid viscosity (Pa s) and  $k$  is the permeability of the solid ( $m^2$ ). Equation 13 can be rewritten in terms of the velocity of the fluid and solid phases as:

$$\Phi_f \left( \{\vec{v}^f\} - \{\vec{v}^s\} \right) = \frac{k [I]}{\mu} \nabla P \quad (14)$$

Where  $\Phi_f$  is the volume fraction of fluid, and  $\{\vec{v}^f\}$  and  $\{\vec{v}^s\}$  are velocities of the fluid and solid, respectively (m/s). Assuming incompressibility, continuity implies:

$$\nabla \cdot \left( \Phi_f \{\vec{v}^f\} + \Phi_s \{\vec{v}^s\} \right) = 0 \quad (15)$$

Where  $\Phi_s$  is the volume fraction of the solid phase, and all other terms were previously defined. In addition to continuity, conservation of momentum must also be considered. Momentum in the solid and liquid phase may be considered separately, as per Equations 16 and 17, respectively:

$$\frac{\partial \sigma_{ij}^f}{\partial x_j} + \frac{\Phi_f^2}{k} (v_i^s - v_i^f) = 0 \quad (16)$$

$$\frac{\partial \sigma_{ij}^s}{\partial x_j} + \frac{\Phi_f^2}{k} (v_i^f - v_i^s) = 0 \quad (17)$$

Where  $\sigma_{ij}^f$  and  $\sigma_{ij}^s$  are the tensor of stresses in the fluid and solid phases, respectively. Finally, the constitutive equations used for the two phases are:

$$\sigma_{ij}^f = -\Phi_f p \delta_{ij} \quad (18)$$

$$\sigma_{ij}^s = -\Phi_s p \delta_{ij} + \lambda \varepsilon_{kk} \delta_{ij} + 2\mu \varepsilon_{ij} \quad (19)$$

Where  $p$  is fluid pressure,  $\delta_{ij}$  is the Kronecker delta function,  $\varepsilon_{kk}$  is the strain tensor, and  $\lambda$  and  $\mu$  are the first and second Lamé parameters for an isotropic, linear elastic solid. As is commonly done, the viscous term has been neglected from the fluid constitutive equation (18) [104].

The numerical solution to the system of equations defining a linear biphasic material (Equations 13-19), has been implemented in commercial finite element software ABAQUS. Previous studies have shown good agreement between the solutions obtained numerically through ABAQUS, compared to analytical results [105].

### 2.3.3. Modelling Dynamic Effects

Another limitation of traditional modelling techniques, described in section 2.3.1, is that only quasi-static loading is considered and inertial effects are ignored. However, realistic loads are dynamic in nature (Sections 2.1.2 and 2.1.3). Fall loads, for example, are highly impulsive with a large magnitude and a short duration. For these types of loads, inertial effects may become significant, and strains due to the dynamic loading may be greater than the static case, a process known as dynamic amplification [106]. However, few studies in the literature have modelled

inertial effects [42], [43], and to the best of the author's knowledge, none have compared dynamic loading to the static case.

The finite element software ABAQUS can be used to model dynamic loading. One method for doing so is by direct integration of the equations of motion. In this method, the equation of equilibrium is expressed as:

$$[M]_{global}\{\ddot{\mathbf{u}}\}^{t+\Delta t} + (1 + \alpha)(\{\mathbf{I}\}_{global}^{t+\Delta t} - \{\mathbf{F}\}^{t+\Delta t}) - \alpha(\{\mathbf{I}\}_{global}^t - \{\mathbf{F}\}^t) = 0 \quad (20)$$

Equation 20 is solved using the time integration scheme described by Hilber et al. [107]:

$$\{\mathbf{u}\}^{t+\Delta t} = \{\mathbf{u}\}^t + \Delta t\{\dot{\mathbf{u}}\}^t + \Delta t^2\left(\left(\frac{1}{2} - \beta\right)\{\ddot{\mathbf{u}}\}^t + \beta\{\ddot{\mathbf{u}}\}^{t+\Delta t}\right) \quad (21)$$

$$\{\dot{\mathbf{u}}\}^{t+\Delta t} = \{\dot{\mathbf{u}}\}^t + \Delta t\left(\left(\frac{1}{2} - \gamma\right)\{\ddot{\mathbf{u}}\}^t + \gamma\{\ddot{\mathbf{u}}\}^{t+\Delta t}\right) \quad (22)$$

Where  $\{\mathbf{u}\}$  is the vector of nodal displacements, and  $\{\dot{\mathbf{u}}\}$  and  $\{\ddot{\mathbf{u}}\}$  are its first and second time derivatives, respectively.  $t$  is the current time,  $\Delta t$  is the time increment and  $\{\mathbf{F}\}$  is the vector of applied loads.  $\alpha$  is a term which introduces numerical damping into the solution; this is intended to reduce high-frequency noise which is an artifact of the solution procedure, without having a significant impact on the more meaningful, low frequency response [108].  $[M]_{global}$  is the system mass matrix and  $\{\mathbf{I}\}_{global}^{t+\Delta t}$  is the vector of internal forces. In the finite element method, these are assembled from their individual element contributions which are calculated using Equations 23 and 24 below:

$$[\mathbf{m}^{(e)}] = \iiint_{V^{(e)}} \rho [\mathbf{N}]^T [\mathbf{N}] dV \quad (23)$$

$$\{\mathbf{i}^{(e)}\} = \iiint_{V^{(e)}} [\mathbf{B}]^T \{\boldsymbol{\sigma}\} dV \quad (24)$$

Where  $[\mathbf{m}^{(e)}]$  and  $\{\mathbf{i}^{(e)}\}$  are the mass matrix and internal force contributions from the  $e^{\text{th}}$  element in the model,  $\rho$  is the density,  $[\mathbf{N}]$  is the matrix of finite element shape functions,  $[\mathbf{B}]$  is the

strain-displacement relationship, and  $\{\sigma\}$  is the vector of element stresses. In this study,  $\{\sigma\}$  is computed for a viscoelastic solid, and is a function of time.

$$\{\sigma\}^t = \int_0^t 2 G(t - t') \{\dot{\epsilon}\} dt' + [I] K \phi \quad (25)$$

Where  $G$  is the shear modulus, as a function of time  $t$ ,  $\{\dot{\epsilon}\}$  is the deviatoric strain rate,  $K$  is the bulk modulus and  $\phi$  is the volumetric strain. The numerical solution to Equations 20-25 have been implemented in the finite element software, ABAQUS, which was used for this phase of the study.

#### **2.3.4. A Gradient-Enhanced Damage Model for Bone**

Accuracy of FE predictions for femoral failure are likely to improve with more accurate models of nonlinear bone behaviour. As mentioned previously, there is currently no consensus on the best material model to use. However, recent studies by Hambli et al. [80]–[82] have used continuum damage mechanics (CDM) to incorporate the effects of bone damage (described in Section 2.2.3) into finite element modelling with very good results. Compared to experimental evidence, their simulations have been able to accurately predict the force-displacement curves and fracture pattern.

While the technique is powerful, there are important challenges that need to be addressed. FE models that include strain softening behaviour have well documented issues with spurious mesh sensitivity. The size of the damaged region corresponds to the size of the mesh used to solve the problem. As the mesh is refined, the size of the damaged region, and thus the energy dissipated, shrinks. This is a physically inadmissible result; the energy dissipated by crack formation is a property of the material and should not be dependent on mesh size [109], [110].

To remedy this issue, some authors have proposed using a non-local constitutive model. For example, damage evolution can be driven by a weighted spatial averaging of strains near a point, rather than the local strain at the point itself. This technique has been used successfully for simulations of vertebral bone [111], but is difficult to implement within a conventional finite element solver. As an alternative, gradient-dependent descriptions have recently gained interest. Based on Taylor series expansions, these models approximate the nonlocal parameter as the solution to a differential equation which can be evaluated locally [112]. This equation can be easily coupled to the equation of equilibrium and solved using the finite element method.

Formulation of the nonlocal model, and its implementation using finite elements, was derived in detail by Peerlings et al [79], [113], but is summarized here for the reader's convenience. In a quasi-brittle material, stress at a point is a function of both strain and the state of damage. This behaviour was described in Equation 10, but is reproduced here for the readers' convenience:

$$\boldsymbol{\sigma} = (1 - D)\mathbf{C} \boldsymbol{\varepsilon} \quad (10)$$

The state of damage is related to the loading history; most typically, damage is related to a scalar measure of deformation, known as equivalent strain  $\varepsilon_{eq}$ , computed from components of the strain tensor. In a nonlocal model, damage is related to a weighted volume average of equivalent strains, computed from Equation 26:

$$\overline{\varepsilon_{eq}}(\vec{x}) = \int_V g(\vec{\varepsilon}) \varepsilon_{eq}(\vec{x} + \vec{\varepsilon}) dV \quad (26)$$

Where  $\overline{\varepsilon_{eq}}(\vec{x})$  is the nonlocal equivalent strain at point  $\vec{x}$ ,  $\vec{\varepsilon}$  is an integration variable, and  $g(\vec{\varepsilon})$  is the weighting function. Unfortunately, Equation 26 is difficult to implement in a traditional finite

element solver. However, by manipulating the Taylor series expansion of Equation 26, Peerlings [112] showed that the nonlocal strain can be approximated using a differential equation:

$$\overline{\varepsilon_{eq}} - c\nabla^2\overline{\varepsilon_{eq}} = \varepsilon_{eq} \quad (27)$$

Where  $c$  is a nonlocal interaction radius with units of length squared. Equation 28 is significantly easier to implement and solve using the finite element method.

The custom finite element finite element used in this study simultaneously solves the equation for nonlocal strain (Equation 28) alongside the familiar equation of static equilibrium with body forces neglected:

$$\nabla \cdot \boldsymbol{\sigma} = 0 \quad (28)$$

Coupling between Equation 27 and 28 occurs because stress  $\boldsymbol{\sigma}$  is related to damage, from the constitutive law (Equation 10), and damage evolution is computed from nonlocal strains (Equation 12). To solve this system equations, the unknown fields of displacement ( $\mathbf{u}$ ) and nonlocal strain ( $\overline{\varepsilon_{eq}}$ ) are discretized using two sets of standard finite element shape functions  $\mathbf{N}_u$  and  $\mathbf{N}_\varepsilon$ :

$$\mathbf{u} = \mathbf{N}_u \bar{\mathbf{U}} \quad (29)$$

$$\varepsilon_{eq} = \mathbf{N}_\varepsilon \bar{\mathbf{E}} \quad (30)$$

Where  $\bar{\mathbf{U}}$  and  $\bar{\mathbf{E}}$  are vectors containing the nodal values of displacement and nonlocal equivalent strain, respectively. Analogous to the derivation of a more standard continuum finite element, divergence theorem is used to manipulate Equation 28 into the weak form. Substitution of Equation 29 then results in the familiar finite element equations:

$$\mathbf{f}_u^{int} = \mathbf{f}_u^{ext} \quad (31)$$

$$\mathbf{f}_u^{int} = \int (\mathbf{B}_u)^T \boldsymbol{\sigma} d\Omega \quad (32)$$

$$\mathbf{f}_u^{ext} = \int (\mathbf{N}_u)^T \mathbf{p} d\Omega \quad (33)$$

Where  $\mathbf{p}$  is the vector of external nodal forces acting on the body. The matrix  $\mathbf{B}_u$  is assembled from derivatives of the shape functions  $\mathbf{N}_u$ , and describes the strain-displacement relationship. Similarly, casting the differential equation for nonlocal strain into the weak form, and substituting the discretization Equation 6, yields:

$$\mathbf{K}_{\varepsilon\varepsilon} \bar{\mathbf{E}} = \mathbf{f}_e \quad (34)$$

Where:

$$\mathbf{K}_{\varepsilon\varepsilon} = \int \mathbf{N}_\varepsilon^T \mathbf{N}_\varepsilon + \mathbf{B}_\varepsilon^T \mathbf{c} \mathbf{B}_\varepsilon d\Omega \quad (35)$$

$$\mathbf{f}_e = \int \mathbf{N}_\varepsilon^T \varepsilon_{eq} d\Omega \quad (36)$$

Similar to Equation 32, the matrix  $\mathbf{B}_\varepsilon$  is assembled from derivatives of the shape functions  $\mathbf{N}_\varepsilon$ . Damage evolution causes nonlinearity, and so Equations 31 and Equation 34 are linearized then solved by Newton-Raphson iterations. For a given set of estimated solution variables  $\bar{\mathbf{U}}_i$  and  $\bar{\mathbf{E}}_i$  estimated at iteration  $i$ , the updates  $\bar{\mathbf{U}}_{i+1} = \bar{\mathbf{U}}_i + \Delta \bar{\mathbf{U}}$  and  $\bar{\mathbf{E}}_{i+1} = \bar{\mathbf{E}}_i + \Delta \bar{\mathbf{E}}$  are computed from:

$$\begin{bmatrix} \mathbf{K}_{uu} & \mathbf{K}_{u\varepsilon} \\ \mathbf{K}_{\varepsilon u} & \mathbf{K}_{\varepsilon\varepsilon} \end{bmatrix} \begin{Bmatrix} \Delta \bar{\mathbf{U}}_i \\ \Delta \bar{\mathbf{E}}_i \end{Bmatrix} = \begin{Bmatrix} \mathbf{f}_u^{ext} - \mathbf{f}_u^{int} \\ \mathbf{K}_{\varepsilon\varepsilon} \bar{\mathbf{E}}_i \end{Bmatrix} \quad (37)$$

Where:

$$\mathbf{K}_{uu} = \int \mathbf{B}_u^T (1 - D) \mathbf{C} \mathbf{B}_u d\Omega \quad (38)$$

$$\mathbf{K}_{u\varepsilon} = - \int \mathbf{B}_u^T \mathbf{C} \boldsymbol{\varepsilon} \mathbf{q} \, d\Omega \quad (39)$$

$$\mathbf{K}_{\varepsilon u} = \int \mathbf{N}_\varepsilon^T \left( \frac{\partial \boldsymbol{\varepsilon}_{eq}}{\partial \boldsymbol{\varepsilon}} \right)^T \mathbf{B}_u \, d\Omega \quad (40)$$

$$\mathbf{K}_{\varepsilon\varepsilon} = \int \mathbf{N}_\varepsilon^T \mathbf{N}_\varepsilon + \mathbf{B}_\varepsilon^T c \mathbf{B}_\varepsilon \, d\Omega \quad (41)$$

The term  $\mathbf{q} = \frac{\partial D}{\partial \boldsymbol{\varepsilon}_{eq}}$  if equivalent strain is increasing, and zero otherwise; this prevents the model from reversing damage if strain decreases. Equation 37 can be solved with commercially available nonlinear finite element solvers, but custom coding was required.

## Chapter 3: Simulation of Fall Loading: Impact of BCs and Multiphysics Effects on In-Vitro Investigations of Femoral Fracture Strength

Significant portions of this chapter have been published in the Journal of Biomechanics:

**Haider, I. T.**, Speirs, A. D., & Frei, H. (2013). Effect of boundary conditions, impact loading and hydraulic stiffening on femoral fracture strength. *Journal of Biomechanics*, 46(13), 2115–21. doi:10.1016/j.jbiomech.2013.07.004

### 3.1. Introduction

In-vitro investigation through FE modelling is a powerful tool in the study of osteoporotic hip fractures. It allows the researcher to investigate phenomenon which would be impossible to study *in-vivo*, because of practical or ethical concerns. However, in order to obtain meaningful results, care must be taken to ensure that the *in-vitro* studies accurately reflect the *in-vivo* condition. All relevant physics needs to be included in the simulation, and boundary conditions must be selected carefully in order to obtain meaningful results.

The accuracy of the FEM predictions may be enhanced by including physical phenomena in the simulation, which are not yet common practice. As mentioned in section 2.1.2, sideways falling is a highly dynamic event. Although numerous authors have used finite element simulation [13], [17], [18], [45], [67], [82], [85]–[88] to predict hip fracture, few authors included dynamic effects in their FE simulation. Experimental evidence shows that bone is viscoelastic [68], [69], [114] resulting in a deformation response which is dependent on the rate of load application [40]. While time dependent material properties can be incorporated into a quasi-static FE solver, rapid loading may cause inertial effects such as shock wave propagation

[115] or vibration [116], [117]. These effects can be resolved in the FE simulation through direct integration of the equations of motion.

Another rate dependent effect which may be important is hydraulic strengthening of bone which can be caused by the bone marrow, a viscous fluid in the intramedullary cavity. High volumetric strains may cause increases in pore pressure, which may support part of the applied load causing an increase in apparent stiffness [98]–[100]. While there is reasonable evidence demonstrating this effect at the material level [99], [101], at the time of this investigation no study had shown whether hydraulic strengthening effects significantly affect the fracture strength of a femur during fall impact.

Another major challenge in developing a finite element model of the femur during a fall is the simulation of BC's that represent the femur in vivo. Discussed in Section 2.1.2, the orientation of the femur during a fall is well understood [40] but there are many differing examples in the literature on how the femur should be constrained [21], [40], [45], [46], [118]. While it is difficult to prove with certainty which set of BCs is most accurate, these differing studies are often well referenced and considered important to the field. Thus it, remains important to understand how these differences in BC selection can influence results.

The purpose of this chapter is to better quantify all of the effects discussed above, and how they influence prediction of femoral fracture load. Using a patient specific finite element model of the proximal femur, four different effects were investigated: (I) the effect of different BCs to simulate fall, (II) the effect of viscoelasticity and poroelasticity during fall, (III) the effect of muscle forces during simulation of physiological loads, and (IV) the effect of model orientation/alignment errors during physiological loading.

## 3.2. Methods

### 3.2.1. Developing a Specimen-Specific FE model

A three-dimensional finite element model of a proximal human femur was generated from quantitative computed tomography (qCT) scans of a fresh frozen cadaveric femur. Inclusion of a CT calibration phantom (Model 3, Mindways Software, TX, USA) with the specimen allowed estimation of bone density from the image intensity values. Scans were performed with a 0.5mm slice thickness and 0.49 x 0.49 in-plane resolution. The femur was segmented from the CT scan (OsiriX Imaging Software, osirix-viewer.com) and converted to a parametric solid model (Pro/ENGINEER v5.0, Parametric Technology Corporation, MA, USA).

The solid model was meshed using PATRAN (v2008r2, MSC Software, CA, USA) and later refined using AMIRA (v5.2, Visage Imaging, CA, USA), resulting in a mesh with 164000 quadratic tetrahedral elements. Elements on the proximal surface, above the lesser trochanter, had an average edge length of 2 mm, a mesh density which was found to yield good results for a femur in fall configuration [88]. On the femoral shaft, where stress gradients were much lower, the mesh was coarsened to an average edge length of 4.75 mm. Subsequent finite element analyses were performed using ABAQUS (v6.10, Dassault Systèmes, RI, USA). While the density of the mesh was selected based on previous investigations, a brief convergence study was also performed in order to verify accuracy of the mesh. A coarsened mesh of 28000 elements yielded strains which were nearly identical (less than 1% difference) to the 164000 element model described above. All subsequent models were solved using the 164000 element mesh, with different simulation parameters which are summarized in Table 3. It should be noted that the original segmentation and mesh generation tasks were performed by Timothy Elgin as part of a previous research project [119]. However, mesh refinement and all future modelling tasks were performed by the author.

Bone tissue was initially modeled as an isotropic, linearly elastic material and properties were assigned individually to each node. The ABAQUS solver interpolates nodal material property values at each integration point based on element shape functions. A custom Matlab (r.2010b, MathWorks Inc, MA, USA) script, written by the author, was used to sample CT intensity at each nodal location. This value was then related to an equivalent  $K_2HPO_4$  mineral density by linear regression using the measured CT intensities in the phantom compared to known density values provided by the manufacturer's certificate. As discussed in section 2.3.4, elastic modulus  $E$  of each element could be determined based on the density using Equation 7. To apply this equation,  $K_2HPO_4$  mineral densities, obtained from the qCT scans, were related to bone ash densities using previously reported correlations [120]. Ash densities were then normalized to apparent density using the ratio  $\rho_{ash}/\rho_{app}=0.6$  [67].

Failure load was estimated based on the work of Schileo et al. [73] who found that a maximum principal strain criterion was a specific predictor of fracture load. An element was considered to have failed if the principal strain exceeded the yield strains for bone, which were selected to be 1.04% in compression and 0.73% in tension [72]. The fracture load of the femur was defined when the total exposed area of the failed surface elements reached  $160\text{ mm}^2$  [73]. Due to linearity of the model, 100 N of load was applied and the results were scaled until a fracture surface of  $160\text{ mm}^2$  was reached.

### **3.2.2. Effects of Different Fall Boundary Conditions**

Three different BCs were selected, based on examples in the literature discussed in Section 2.1.2 [40], [45], [46]. They are repeated here for the reader's convenience. Boundary conditions were applied to the femoral head (FH), greater trochanter (GT) and femoral shaft (FS) as follows: (Case I) the FS and GT were fully constrained to rotation and translation, while the

FH was loaded; (Case II) the FS was only free to rotate in the coronal plane and translate along the shaft axis in the coronal plane. The GT was constrained in translation but free to rotate in all directions; (Case III) the FS was only free to rotate and translate in a cranio-caudal direction in the coronal plane. The FH was only free to rotate in the coronal plane. Load was applied to the GT. Visualizations of these three cases were shown in Figure 5, section 2.1.2.

For all three BC's, the femur was oriented in a fall configuration, with the shaft at  $10^\circ$  to the ground and femoral neck at rotated  $15^\circ$  internally [21], [40]. Each of the BC's above were applied by either restricting all nodes along the axis of rotation (pinned BC) or 3 or more non-collinear nodes (fully constrained BC). The different BCs were compared at an arbitrary load of 100 N. Three simulations were run for this phase of the study, as described in Table 3.

### **3.2.3. Multiphysics Effects**

The static model was modified in order to investigate the influence of dynamic effects on femoral fracture. Based on previous simulations [42], the load was approximated as a sinusoidal pulse, with a 8.3 kN peak at 21 ms applied to the GT. Since dynamic load profiles were only available for BC III, where the load is applied to the GT only this case was used for dynamic simulations.

The material property assignment, discussed above, was augmented to include the effects of bone viscoelasticity, using Equations 8 and 9, which describe the viscoelastic behaviour of cortical and trabecular bone, respectively. While the femur consists of both cortical and trabecular bone, it is difficult to incorporate spatially varying viscoelastic properties into an ABAQUS model. Instead, separate simulations were performed using the stress relaxation relationship for cortical bone (Equation 8) and cancellous bone (Equation 9), throughout the

model. Two different solvers were used: a quasi-static solver, which only resolves the effects of bone viscoelasticity and a dynamic solver which also simulates inertial effects (vibration and impact) by integrating the equations of motion using an implicit scheme [108], detailed in section 2.3.3. The failure criterion described above was also used for these models. Fracture load was estimated by identifying the first time instant where the exposed fracture surface reached 160 mm<sup>2</sup>. In total, four dynamic models were created, with simulation parameters summarized in Table 1.

Carter and Hayes (1977) observed that samples with bone marrow show effects of hydraulic strengthening, but only at high strain rates. In an attempt to observe this effect, the dynamic model, discussed above, was modified to account for bone marrow. This was performed with a coupled pore fluid diffusion and stress analysis in ABAQUS, which was described in greater detail in section 2.3.2. The solid matrix was simulated as viscoelastic cortical bone (Equations 7 and 8), with the addition of a nodally assigned permeability. Cortical bone has an average permeability of  $4.68 \times 10^{-13} \text{ m}^2$  [121], while permeability of trabecular bone varies logarithmically with porosity [122]. Data from these two studies were combined to give a porosity-density relationship of:

$$\log_{10} k = -4.1 - 22(1 - P) \quad (P > 0.6) \quad (42.a)$$

$$k = 4.68 \cdot 10^{-13} \quad (P \leq 0.6) \quad (42.b)$$

Where  $k$  is the permeability (m<sup>2</sup>), and  $P$  is the porosity (bone volume/total sample volume). At a porosity of 0.6, the logarithmic expression (Equation 42.a) calculates a permeability for trabecular bone equal that of cortical bone; as permeability of trabecular bone is unlikely to drop to less than that of cortical bone, this expression was only used for samples with porosity greater

than 0.6. Equation 42.a and 42.b were used to calculate permeability at each nodal location. The highest nodal density was assumed to be dense cortical bone, with a porosity of 0.04 [121], and the porosity at the other nodes was calculated based on their density through the rule of mixtures. Bone marrow, which behaves like a Newtonian fluid near body temperature, was assigned a density of 1.06 g/cm<sup>3</sup> and a viscosity of 400 cP [63]. One pore fluid diffusion and stress analysis was performed, with parameters summarized in Table 3.

Table 3 Summary of simulations performed their objectives, and model parameters.

Evaluating effects of:	BC Case <sup>a</sup>	Peak Load (N)	Material Model	Analysis
Boundary Conditions	I	100	Linear elastic <sup>b</sup>	Linear Static
	II	100	Linear elastic <sup>b</sup>	Linear Static
	III	100	Linear elastic <sup>b</sup>	Linear Static
Dynamic Effects	III	8300 <sup>b</sup>	Cortical viscoelasticity <sup>c</sup>	Quasi-static
	III	8300 <sup>b</sup>	Cortical viscoelasticity <sup>c</sup>	Implicit dynamic
	III	8300 <sup>b</sup>	Trabecular viscoelasticity <sup>d</sup>	Quasi-static
	III	8300 <sup>b</sup>	Trabecular viscoelasticity <sup>d</sup>	Implicit dynamic
Hydraulic Strengthening	III	8300 <sup>b</sup>	Solid: Cortical viscoelasticity <sup>c</sup> Fluid: Newtonian bone marrow	Coupled pore fluid diffusion and stress

<sup>a</sup> Boundary conditions were detailed in Figure 5.

<sup>b</sup> The linear elastic model used a density based, spatially varying Young's modulus (Equation 7)

<sup>c</sup> The cortical viscoelasticity model augmented the linear elastic model (Equation 7) with time dependent properties of cortical bone (Equation 8)

<sup>d</sup> The trabecular viscoelasticity model augmented the linear elastic model (Equation 7) with time dependent properties of trabecular bone (Equation 9)

<sup>e</sup> The fluid phase was assigned properties of bone marrow, with a viscosity of 400 cP and density of 1.06 g/cm<sup>3</sup> [63].

### 3.3.Results

#### 3.3.1. Effects of Different Fall Boundary Conditions

Strain patterns were nearly identical for all BC cases (Figure 17), with large strains in the subcapital region. Peak minimum and maximum strains occurred in a localized region on the superior subcapital aspect, with a second region of high maximum strain on the inferior subcapital aspect (Figure 18 and Figure 19). As shown in Figure 20 , Case III, with the load applied to the greater trochanter, showed slightly lower (<22% difference) peak strains, and thus slightly higher fracture load, than Cases I and II, which were loaded on the femoral head.

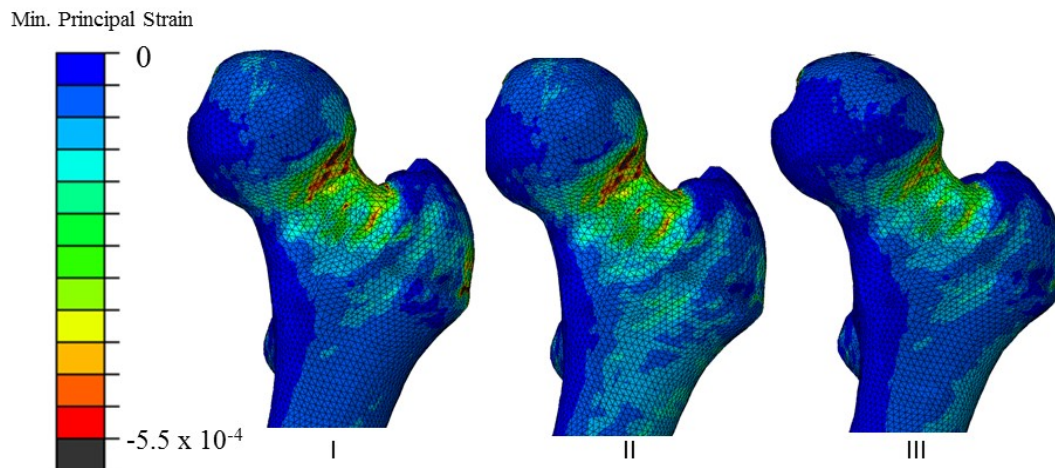


Figure 17 Minimum principal strain for three boundary conditions. The overall pattern and location of peak strain was identical for three cases, however, strain magnitudes were up to 20% lower for case III, with the load applied to the GT instead of the FH. Strains were predicted for an applied load of 100 N (Table 3). The scale was limited to a strain value of  $-5.5 \times 10^{-4}$ ; this value was selected to clearly show the pattern of strains, but has no other physical significance.

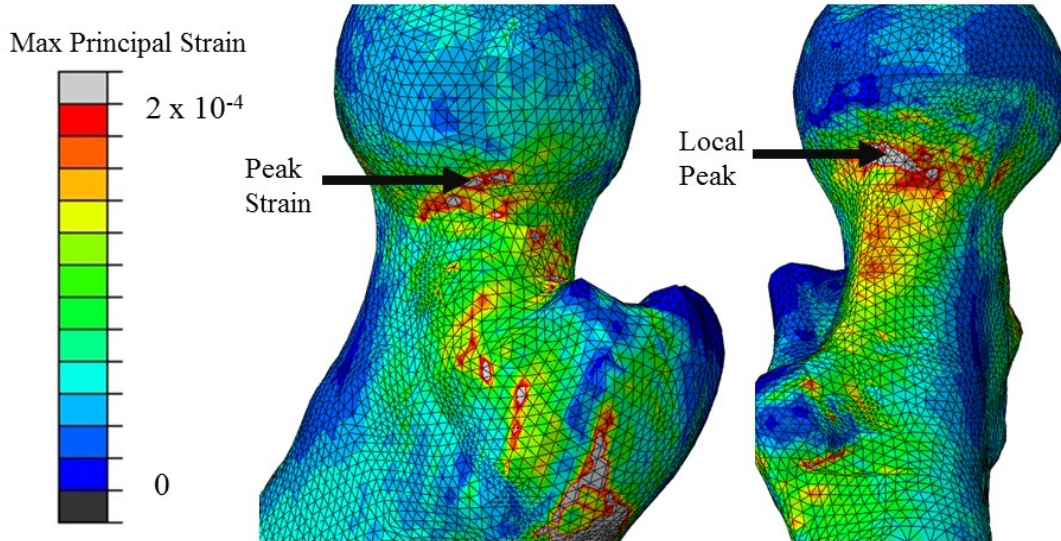


Figure 18 Maximum principal strains for Case I. All other cases showed identical strain patterns. Peak strain occurred in the superior aspect of the subcapital region, with a second region of locally high strain on the inferior aspect of the subcapital region. Strains were predicted for an applied load of 100 N (Table 3). The scale was limited to a strain value of  $2 \times 10^{-4}$ ; this value was selected to clearly show the pattern of strains, but has no other physical significance.

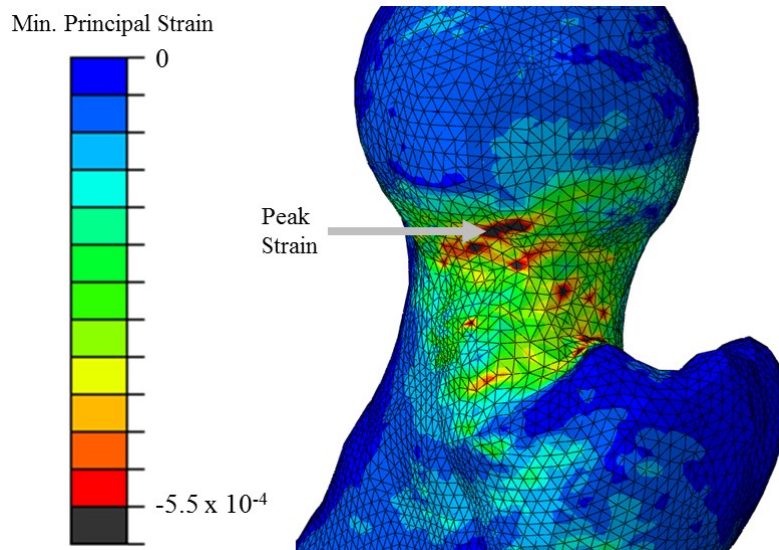


Figure 19 Minimum principal strains for Case I. All other cases showed identical strain patterns. As with maximum principal strain, peak minimum principal strain occurred in the superior aspect of the subcapital region. Strains were predicted for an applied load of 100 N (Table 3).

The scale was limited to a strain value of  $-5.5 \times 10^4$ ; this value was selected to clearly show the pattern of strains, but has no other physical significance.

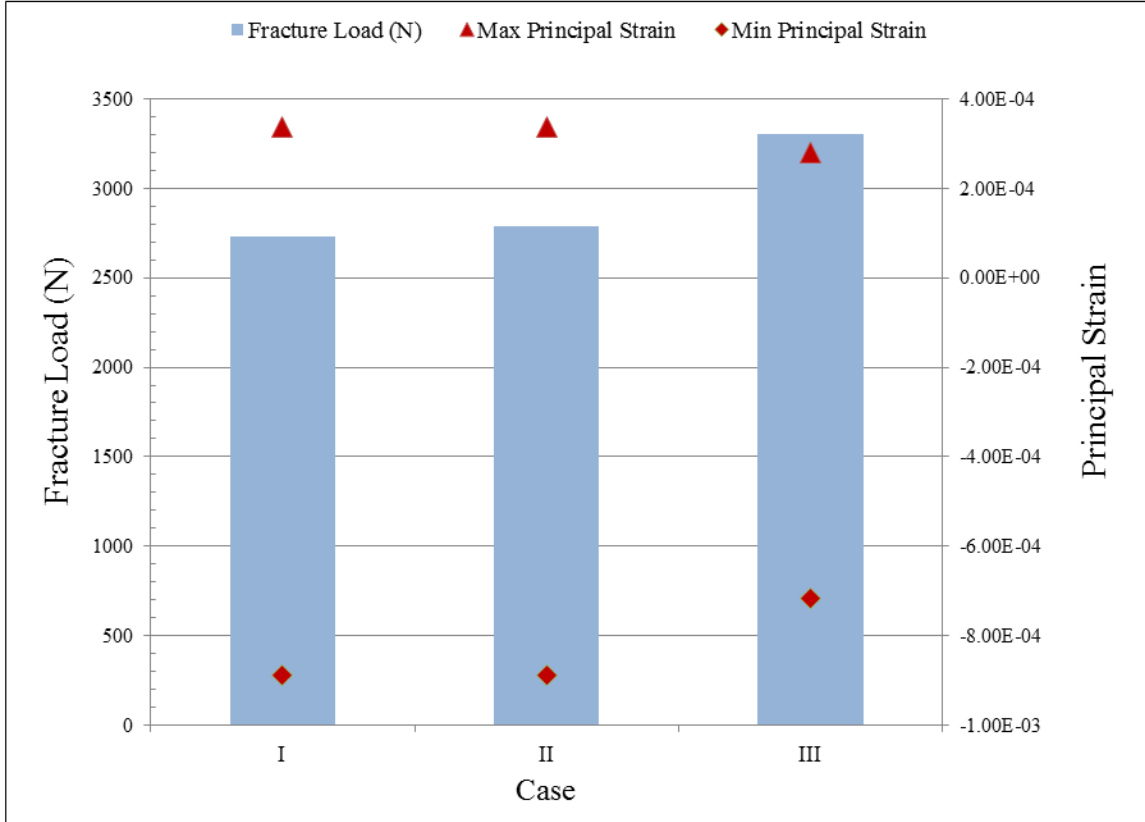


Figure 20 Failure loads (blue bar) and peak maximum (red triangle) and minimum (red diamond) principal strains for three BC cases investigated. As shown in Figs. 3 and 4, peak strains occurred in the superior subcapital region for all BC cases investigated. However, the magnitude of peak strain was approximately 22% lower when load was applied to the GT (Case III) compared to cases loaded at the FH (Case I and II). As a result, fracture strength in Case III was 18% higher compared to the other cases.

### 3.3.2. Multiphysics Effects

Results of the dynamic models showed that inertial effects were negligible, with very little difference between the dynamic and quasi-static solutions (<3% peak strain). Vibration effects were only significant for unrealistically short duration impacts (Figure 21).

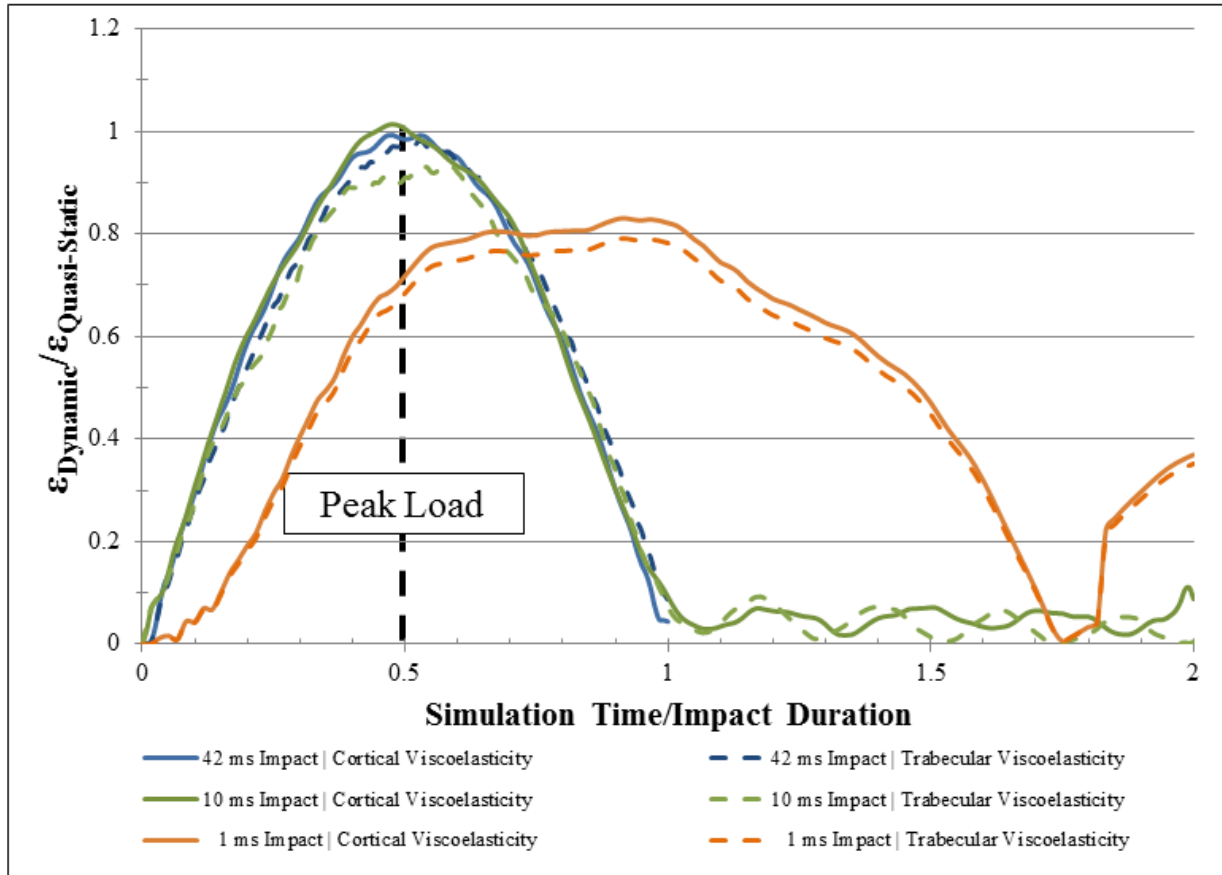


Figure 21 Normalized time history of peak maximum principal strain, located at the inferior aspect of the femoral head (Figure 18). Minimum principal strains of the dynamic solution ( $\epsilon_{\text{Dynamic}}$ ) were normalized with respect to the quasi-static solution for minimum principal ( $\epsilon_{\text{Static}}$ ) and time was normalized with respect to impact duration. Impact durations of 42 ms (blue), 10 ms (green) and 1 ms (orange) were applied to models using the viscoelastic properties of cortical (solid line) and cancellous bone (dashed line). Vibration effects were only significant for the 1 ms impact duration, but the magnitude of the response was attenuated in the more dissipative cancellous bone viscoelasticity model.

Effects of viscoelasticity, however, were significant. The viscoelastic models had fracture loads of 3400 and 3800 kN, using viscoelastic properties of cortical and trabecular bone, respectively. This was 3% and 15% higher than the fracture load of the equivalent linear elastic model (BC III). However, little difference in strain distribution, and thus predicted fracture pattern, was seen compared to the linear elastic, static model (Figure 22).

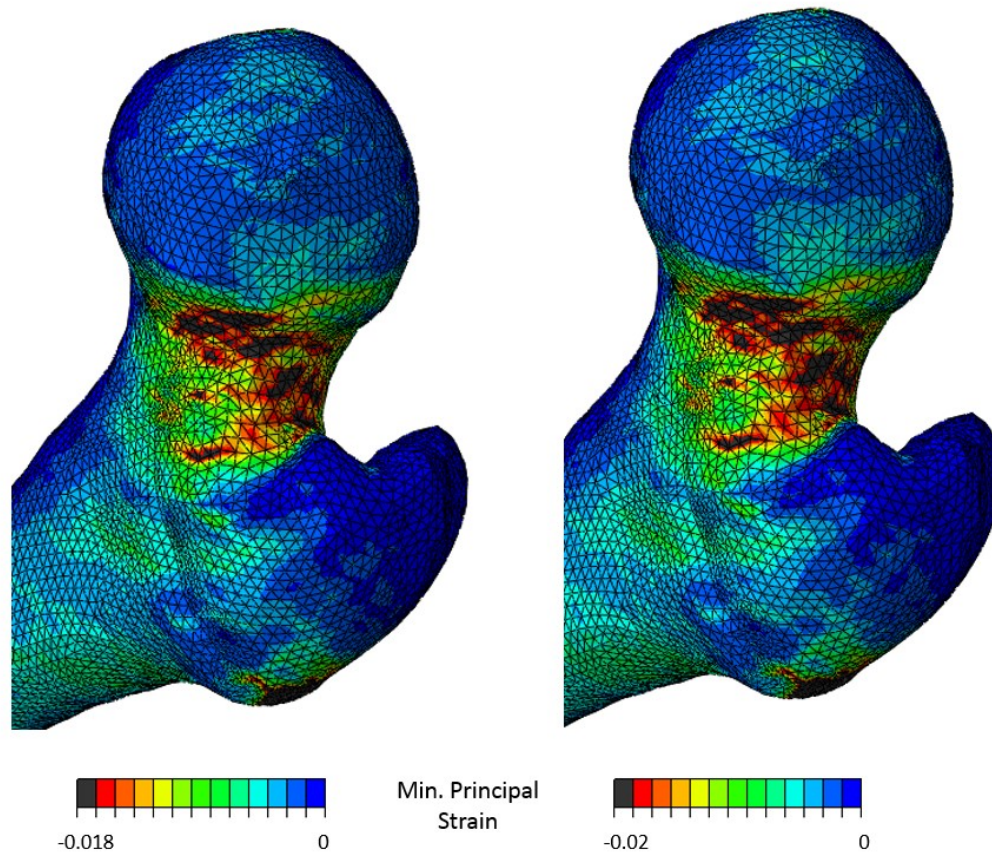


Figure 22 Minimum principal strains from trabecular viscoelasticity model (LEFT) compared to linear elastic model (RIGHT). Strain magnitudes were lower in the viscoelastic model, resulting in a 15% increase in strength compared to the linear elastic case. In this figure, the scale of the color plots were adjusted to reveal that strain distribution patterns remained consistent between the two models.

Finally, the effects from bone marrow were found to have little impact on simulation results. Rise in marrow pressure was low, at less than 2% of the maximum hydrostatic stress, resulting in little hydraulic strengthening effects. However, no volume change was measured at any time step suggesting that this trivial increase in pore pressure was due to the convergence criteria of the model, and is likely non-physiological. As a result, the pattern of strain in the biphasic model was also identical to that found in the equivalent quasi-static model with peak strains differing by only 4%.

### 3.4. Discussion

The goal of these simulations was to determine the suitability of different models in predicting femoral fracture. There is a growing consensus on the use of strain based failure criterion for bone [70], [71], [123]. In contrast to yield stress, yield strain for bone is isotropic and relatively homogeneous [72]. As a result, this study chose to examine minimum and maximum principal strains for all cases modelled, and fracture load was estimated using a strain based-criterion.

This study adopted a failure criterion using experimental data from a femur loaded in a quasi-axial configuration [73]. Fracture was predicted to occur when a failure surface of 160 mm<sup>2</sup> was reached. Although this study also investigated a sideways fall, both loading configurations predict a similar type of failure, i.e., a femoral neck fracture. The predicted fracture load was relatively insensitive to choice of failure surface, and changing the failure surface by  $\pm 10\%$  changed fracture load by less than 3%. In the past, linear models using similar failure criteria have achieved strong correlation between FE predicted and experimentally measured failure loads [96]. This choice of failure criterion was an effective, and computationally efficient, means of evaluating the relative structural response from the many different simulations performed in this study.

A more accurate estimation of fracture load could be achieved by incorporating nonlinear material properties, but there is little consensus in the literature on how to best model failure of bone material at the element level [17], [18], [82], [91]. Based on these preliminary investigations, such a model was developed and validated in future investigations (Chapter 5).

### 3.4.1. Effects of Different Fall Boundary Conditions

Strain patterns were identical for all BC cases (Figure 17). Thus, prediction of fracture location and pattern is not sensitive to the choice of BCs. However, if the femoral head (BCs I and II) was loaded instead of the GT (BC III), peak strain increased by 22% and fracture strength decreased by approximately the same amount (18%). However, it is difficult to determine which of the investigated loading conditions best represents a femur during a fall.

In this study, strains in the femoral head and greater trochanter region were disregarded due to their proximity to nodes where BC's and loads are applied. It is difficult to model the *in-vivo* conditions or the *in-vitro* biomechanical test conditions in these regions. For example, the pinned joint at the greater trochanter restricts only a single node resulting in a very large stress concentration. In the body, these forces would be spread out over a larger region by the subject's trochanteric soft tissue. In a mechanical test, the greater trochanter is typically potted in a hemispherical cup, which also distributes the reaction forces. However, these simulations still yield valuable results. High speed footage of femoral failure shows that fracture commonly initiates in the femoral neck and subcapital regions [21]. Thus, accurate determination of strain in this region is important for the prediction of femoral fracture.

The loading conditions examined in this investigation may still be an oversimplification of the femur's *in vivo* condition, as muscle loads were not investigated. Very recent studies suggest that muscle activation can reduce bending moments, and thus peak stress, acting at the femoral neck [124]. However, muscle activity may also increase fall impact force [25], [125], and characterizing the interaction between these effects is somewhat beyond the scope of this work. Realistic muscle activation patterns in elderly hip fracture patients also remain unknown, making it difficult to include these effects into the simulations.

This study predicted that failure will initiate on the superior subcapital aspect of the femoral head, likely followed by a second crack on the inferior subcapital aspect. This is consistent with the experimental findings [21]. Also, using realistic viscoelastic material properties, the failure load was estimated to be between 2800-3800 kN, which is similar to the failure loads predicted by other finite element studies [18], [42] and measured in-vitro [21], [40].

### **3.4.2. Multiphysics Effects**

Results of the dynamic simulation show that local inertial dynamic effects are not significant. For realistic impact durations, the simulated strains were identical to those of an equivalent quasi-static model. The selected parameters of the dynamic model represent a worst case scenario, with regard to propagation of stress waves and vibrational effects. For example, material plasticity was omitted, eliminating the possibility of energy loss due to plasticity. Despite this assumption, no stress wave propagation or significant vibration effects were observed. This is explained by the fact that stress wave effects are significant only if the impact duration is on the same order of magnitude as the time required for the waves to reach the boundaries and return to the impact location [126]. At a speed of approximately 3200 m/s [115], a stress wave could travel the 50 cm distance to and from the model's fixed end in 0.16 ms, which is significantly shorter than the impact durations investigated. Longer duration impacts may cause vibration effect. However, if the impact time is much longer than the fundamental vibrational period, the response is quasi-static [127]. Previous studies measured resonant frequencies of a femur with the head and shaft free to rotate in all directions (free-free condition) and estimated vibrational periods between 3.33 and 4 ms, respectively [128], [129]. While our study uses different boundary conditions, their experimental evidence supports the conclusion

that vibration effects are not significant during a realistic fall simulation. As discussed in section 3.3.2, inertial effects were seen only for extremely short impacts.

Viscoelastic effects were somewhat more significant. Viscoelasticity increases bone stiffness when loaded rapidly and therefore higher loads are required to reach failure strains, resulting in an increased fracture load. This study predicts the dynamically loaded femur to be between 3% (using cortical bone viscoelasticity) to 15% (using cancellous bone viscoelasticity) stronger than a statically loaded femur. Because the femoral neck is composed primarily of cancellous bone, the measured increase in fracture load is expected to be closer to 15%. This is in agreement with previous experimental data which found that realistic fall loading rates increased fracture strength by 12-20% [40]. Inclusion of viscoelastic effects did not, however, influence the distribution of strains (Figure 22).

Bone is also a quasi-brittle material with rate dependent failure properties. However, FE models that predict failure are typically based on bone yield strain [73], [82], [91] which does not vary significantly within the range of strain rates observed during falling [74], [130]. Therefore these effects were not considered in this phase of the study.

Finally, while there is compelling evidence showing the effects of hydraulic strengthening at the material level [99], [101], there is disagreement in the literature on whether the effect is significant under physiologically realistic loading of whole bones. Kafka and Jirova [131] presented a mathematical model for viscous behaviour in trabecular bone which concludes that up to 30% of an impact load is carried by the pore fluid. Their conclusion was supported by the findings of Ochea et al. [132] who found that the dynamic stiffness of intact femoral heads to be 33% higher than cored femoral heads. The significance of these results was questioned by Bryant [100], however, who stated that the loading conditions in Ochea's study do not occur in

nature and whose own experimental findings [98] showed only very small changes in pore pressure (<300 kPa) for a human radius subject to axial impact loads up to 2 kN. The simulations in this study showed that hydraulic strengthening has little effect on whole bones in realistic fall conditions, as this load condition causes no volumetric strain.

As with the previous dynamic FE model, this model was developed to provide a ‘worst case’ estimate of the effects of hydraulic strengthening. It was hypothesized that locally high pore pressures could develop around the greater trochanter, where load was applied rapidly. Material properties were assigned conservatively in order to prevent diffusion of these locally high pore pressures, should they develop, and possibly provide an upper limit for the influence of hydraulic strengthening. For example, permeability of bone is significantly greater in the longitudinal direction than in the transverse direction [122], however an isotropic value using the transverse permeability was assigned to the model. This would hinder local increases in pore pressure from diffusing due to fluid flow. Similarly, pore fluid viscosity was assigned the value measured from bovine red marrow, which represents an upper limit on the viscosity of human marrow in the proximal femur. Again, such a high viscosity would delay pore pressure diffusion due to fluid flow. Despite these highly conservative estimates, this simulation did not find any significant rises in pore fluid pressure, local or otherwise.

## Chapter 4: Simulation of Physiological Loading: Impact of Muscle Forces and Femoral Alignment on In-Vitro Investigations of Femoral Fracture Strength in Stumbling Configuration

### 4.1. Introduction

The previous chapter investigated effects pertaining to the accurate *in-vitro* testing of a femur in fall configuration. However, *in-vitro* investigations may also consider physiological loading conditions. In some respects, physiological loading is simpler than fall loading. For example, physiological loading rates are orders of magnitude lower than fall [29], [30], [42], which significantly reduces the potential influence of dynamic effects. The influence of different BCs at the proximal femur (where hip fractures occur) is also well explored; a recent study by Speirs et al. [61] found little difference in proximal femur strains between models fully constrained midshaft, compared to more realistic BCs applied at the condyles or knee center.

While the BCs themselves are well explored, it remains somewhat unclear how they can be accurately achieved in an *in-vitro* setting. Specimens are typically fixed at the distal end while load is applied to the head. However, care must be taken to ensure that specimen is accurately oriented, and the loads are applied in a physiologically realistic direction. This is particularly true for experimental studies, where landmarks may be difficult to identify and track as a specimen is oriented in 3D space.

The most commonly used physiological load is the stance-like configuration, where the femur is rotated into the neutral position then loaded in the vertical direction [15], [18], [48], [80]. A detailed procedure to approximate the neutral position was reported by Bergman et al. [29] in their study of *in-vivo* hip contact forces (Section 2.1.3). The authors used landmarks on subjects' telemetric implant and femoral condyles to approximate the orientation of the femur

when the subject stood in the neutral position. Other authors have reported similar techniques, using the femoral condyles to orient the femur [48], [133]. However, it is impractical to test a whole femur with condyles intact, and it remains common practice to cut the specimen midshaft or just below the lesser trochanter [15], [18], [48], [80], [80]. In these cases, it remains unclear how the neutral position was identified, or how the cadaveric specimen's orientation was verified before loading. In some cases a single angle is reported [15], [18], [19], [48], such as the angle between the shaft axis and vertical direction in the coronal plane, but no description is given as to how that angle is achieved, or how the coronal plane was identified. Achieving predefined target angles may be particularly challenging during the experimental testing of cadaveric specimens; likely landmarks, such as the neck axis and center of the femoral head, are difficult to measure and track on a physical specimen as it is being rotated in 3D space.

Given the lack of reported details, it is assumed by the author that experience and visual approximation may play some role in the alignment process, with the specimen rotated until it appears correct to the investigator. This lack of detail given to the alignment procedures suggests the assumption that small errors in loading direction do not significantly impact results, but this assumption has not been investigated. In this study, it is hypothesized that errors in femoral alignment may result in measurable differences in predicted fracture load.

As mentioned previously, the oriented specimen is commonly tested by fixing the distal end and applying a load to the proximal end. However, this has been shown to result in large, physiologically unrealistic reaction forces at the femoral shaft [57]–[61]. *In-vivo*, the contact forces are partially reacted by muscle forces which are distributed throughout the femur. It remains unclear whether neglecting these forces has a significant impact on strain distributions in the head-neck region, where fractures typically occur. To the best of the author's knowledge,

only one study has looked closely at the effect of muscle forces on strain distributions in this region [48]. The authors reported that reductions in head-neck strain were quite moderate, but the change was not reported quantitatively. Moreover, the study used a limited set of muscles under walking loads only. It is hypothesized that muscle forces may have a larger, non-negligible, effect during an activity such as stumbling, where forces are expected to be much greater in magnitude.

The purpose of this chapter was to investigate two different phenomenon which may influence accuracy of *in-vitro* testing and modelling of a femur under physiological load configurations: (I) the influence of muscle forces and (II) the impact of femoral alignment errors.

## 4.2. Methods

### 4.2.1. Influence of Muscle Forces

The model described in 3.2.1 was modified to study the effects of muscle forces on proximal femur fracture. In particular, this phase of the study investigated the effects of muscle forces during stumbling. This event resulted in the highest *in-vivo* measurement of hip contact force (Figure 7), making it likely to have the highest magnitude muscle forces as well.

Muscle insertion points and loading directions were adopted from a model developed by an expert anatomist [134], shown in Figure 23. The anatomic model described simplified bone geometry, along with muscle insertion points. For many muscles, force directions are determined by connecting the insertion points at either end of the muscle. Some muscles, however, wrap around bone and other tissues; for these muscles addition ‘wrapping’ points are specified in order to identify load direction.

From the muscle insertion points located on this simplified bone geometry, corresponding points were identified on the more detailed patient specific model developed in section 3.2.1. This was done by aligning the two models using locations of the femoral head center, greater trochanter, and lesser trochanter as landmarks. MeshLab (v. 1.3.3) was used to determine the set of rotations and translations that overlaid the patient-specific model as closely as possible to the anatomic muscle model, i.e., the sum of square difference between landmark positions was minimized. For each muscle insertion point on the simplified anatomical model, the nearest node of the surface of the patient specific model was identified, and used as the point of applied muscle force.

Muscle force magnitudes were estimated using the link segment model described in section 2.1.4. As mentioned previously (section 2.1.4), this model is typically solved with measurements of ground reaction force, segment accelerations, and segment orientation. None of these are available for realistic stumbling events. Instead, a set of reasonable assumptions were made after inspecting video footage of the event [30]. During stumbling, the patient takes several steps in order to regain balance, and each of these steps is associated with localized peak in hip contact force (Figure 7). The peak in force occurred after the foot had been planted firmly on the ground; this event lasted for approximately 0.5 s during which little to no motion could be observed in the leg. Based on these observations, the following assumptions were made: (I) segment accelerations were assumed to be zero, (II) a ground reaction force of 100%BW (736 N for a 75 kg person) was assumed, (III) bone-on-bone contact force  $\{\overline{CF}\}$  (Equation 1), at the hip **was** equal to the force measured *in-vivo*. With these assumptions, the constrained optimization problem described by Equations 1-9 were solved using the Matlab optimization toolkit.

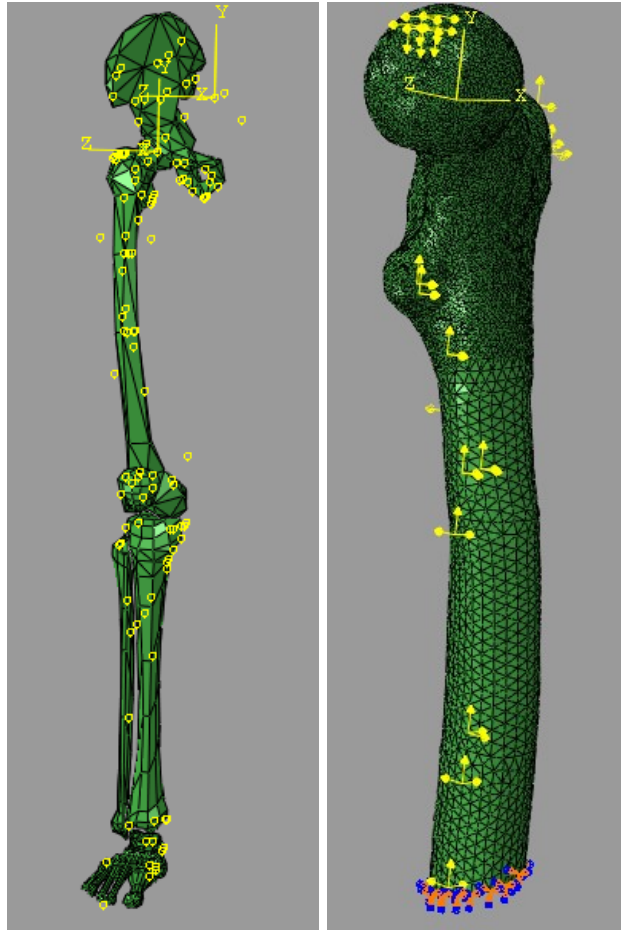


Figure 23 LEFT: Anatomical model with muscle insertion points and load directions [134]. Yellow dots represent either muscle insertion points or wrapping points. Together, these identify muscle force locations and load directions. RIGHT: Corresponding muscle loads applied to patient-specific model

The resulting model was fully constrained in the most distal location (Figure 23), and a hip contact force was applied to the femoral head with a load direction and magnitude simulating the *in-vivo* measurements of hip contact force during stumbling (Figure 7) [30]. Simulations were performed with and without muscle forces applied to the model, and the resulting patterns in femoral strain were compared.

#### 4.2.2. Influence of Femoral Alignment Errors

A new set of models were developed to assess the influence of femoral alignment errors on predicted fracture. This phase of the study compared FE results to orientations achieved during a physical, *in-vitro* experiment. As a result, the model used in the previous sections was not suitable; the cadaveric specimen had been used in a previous study [135] and since destroyed. Instead six new specimens were obtained from the University of Ottawa's division of clinical and functional anatomy, after approval from their research ethics board (Mean age 75, SD=13, weight unknown). However, at the time of this study, two of the six had been loaded to failure as part of the research detailed in Chapter 5, which was performed concurrently. This left four specimens for this phase of the study.

Patient specific models were generated from qCT scans, which were performed with a 0.4 mm slice thickness and 0.48 mm in-plane resolution. Bone voxels were identified using a fully automatic segmentation algorithm [136] and the segmented images were surface wrapped using an algorithm developed by Fang and Boas (2009), and meshed using Netgen [138]. The resulting tetrahedral meshes consisted of approximately 98000 elements, with an average edge length of 2.5 mm. Material property assignment and failure criterion remained identical to the method discussed in section 3.2.1.

Bone was modelled as an isotropic material with spatially varying properties. The software package AMIRA (5.4.3, FEI, OR, USA) was used to sample CT intensity at eight points within each element and report the average. The element averaged intensity was then related to an equivalent  $K_2HPO_4$  mineral density by linear regression using the measured CT intensities in the phantom compared to known density values provided by the manufacturer's certificate. The

young's modulus of each element was assigned using the same relationships described in section 3.2.1.

In order to apply physiologically realistic loads, models of the femur needed to be rotated into the neutral position. As the femoral condyles were unavailable, this was done using the average AV, S, and CCD angles described in section 2.1.3. For each specimen, the femoral neck axis was identified with a line connecting the center of the femoral head to the centroid of the thinnest cross section of the neck. Similarly, the proximal shaft axis was approximated as the line connecting the centroid of the shaft at two locations. A custom matlab script, written by the author, was used to rotate the models until S, CCD, and AV angles matched patient averaged targets of 9°, 135°, and 12° (Table 1, section 2.1.3).

Before any additional work was done, a preliminary FE analysis was performed to determine whether fracture load predictions were sensitive to loading direction. FE models were fixed at the shaft, just below the lesser trochanter, and load was applied to the femoral head corresponding to the direction of peak force during stumbling (Figure 7, section 2.1.3); fracture load was predicted using the failure criterion described in section 3.2.1. To assess the sensitivity, target S, CCD, and AV angles (9°, 135°, and 12°, respectively) were perturbed by one of three levels: -5°, 0°, and +5°. For each of the four femurs, twenty-seven new models were generated, corresponding to all possible permutations of these error levels across the three alignment angles (Table 4). FE predicted fracture load was computed at these twenty-seven load directions, and compared to FE prediction for the specimen when aligned without error.

Table 4. Twenty seven trials used to investigate the effect of small alignment errors on fracture load. Errors reported below were applied relative to the target values of 9°, 135°, and 12° for angles S, CDD, and AV, respectively.

Trial Number	S Error	CCD Error	AV Error
1	5°	5°	5°
2	5°	5°	0°
3	5°	5°	-5°
4	5°	0°	5°
5	5°	0°	0°
6	5°	0°	-5°
7	5°	-5°	5°
8	5°	-5°	0°
9	5°	-5°	-5°
10	0°	5°	5°
11	0°	5°	0°
12	0°	5°	-5°
13	0°	0°	5°
14	0°	0°	0°
15	0°	0°	-5°
16	0°	-5°	5°
17	0°	-5°	0°
18	0°	-5°	-5°
19	-5°	5°	5°
20	-5°	5°	0°
21	-5°	5°	-5°
22	-5°	0°	5°
23	-5°	0°	0°
24	-5°	0°	-5°
25	-5°	-5°	5°
26	-5°	-5°	0°
27	-5°	-5°	-5°

The second objective of this study was to investigate the repeatability and accuracy of positioning by visual approximation, which may be commonly used in experimental studies. The four available cadaveric proximal femurs were positioned by visual approximation, but an optical motion tracking system was used to record the achieved orientation and compare

to the target orientation. To do this, an infra-red rigid body marker was tied around the intertrochanteric region of the femur, and secured with cyanoacrylate. Points on the head, neck, and two planes at shaft (15, 8, 8, and 8 points respectively) were digitized and used to locate the neck and shaft axes. This method was analogous to the node point selections used to identify these features in the FE model, described above. The camera tracked the movement of the femur and the digitized landmarks, and measured the position of the neck and shaft axes as the femur was rotated. A custom Matlab script processed this data and reported S, CD, and AV angles in real time. A copy of the Matlab script is provided in Appendix E, along with additional discussion of the practical implementation of the motion tracking system. The author, a senior graduate student at the time, aligned each specimen by visual approximation and the achieved alignment angles were recorded. The specimen was then set down, and the process repeated a total of six times for each of the four specimens. After the experiment, the corresponding FE models were reoriented to match the S, CCD, and AV angles achieved during visual alignment; fracture load was computed for each case and compared to the FE model aligned without error.

Finally, it was hypothesized that the optical motion tracking system, combined with the method described above, could be used as a more accurate means for achieving alignment targets for *in-vitro* experimental tests. However, two important sources of repeatability errors needed to be quantified.

The first error is associated with the ability to physically rotate and hold the specimens in the desired orientation. This was assessed using the four available cadaveric specimens; each specimen was oriented by the operator, using the real-time feedback from the optical motion

tracking system. The specimen was held in position while a second operator recorded the achieved angles. This was repeated three times for each of the four specimens.

The second error is associated with repeatability of the method used to identify femoral neck and shaft axes. In this study, these axes were identified from a set of points on the head, neck, and two planes of the shaft (15, 8, 8, and 8 points respectively). Repeatability of this process was assessed using the 3D models. For each femur, the set of points needed to identify the axes were located three times. The resulting 3 sets of axes were compared, and any differences in axis orientation were compared.

## **4.3.Results**

### **4.3.1. Influence of Muscle Forces**

As expected the distribution of strains due to physiological loading differ significantly from the fall load case, with large compressive strains dominating both the inferior and superior aspect of the head-neck junction (Figure 24). However, the inclusion of muscle forces (Appendix D) had a measurable, but ultimately minor, influence on strain distribution and fracture load (<3% difference).

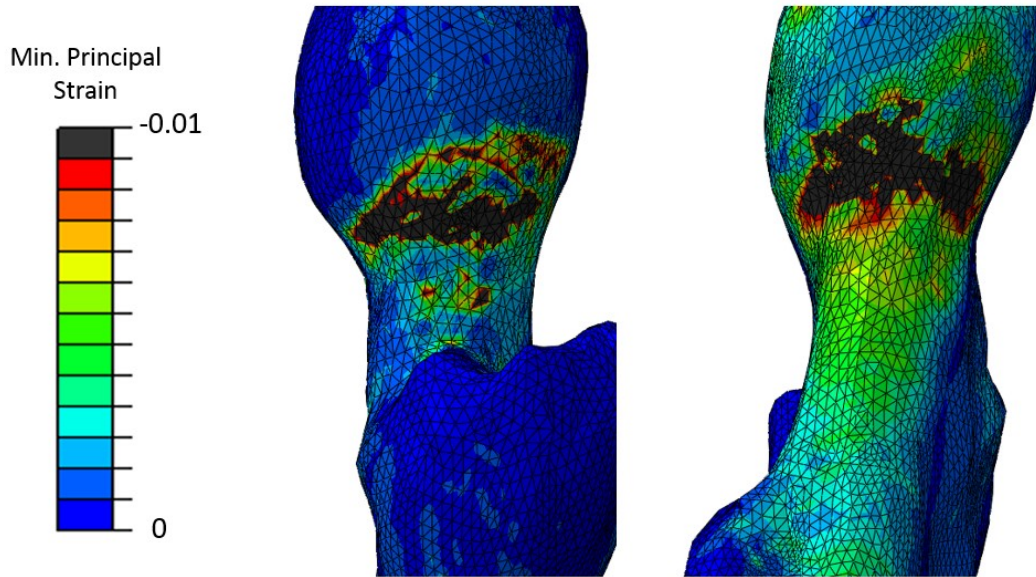


Figure 24 Distribution of minimum principal strain due to stumbling loads. Large compressive strains were predicted at both the superior and inferior aspects of the head-neck junction.

#### 4.3.2. Influence of Alignment Errors

It was found that relatively small errors in alignment can have very large effects on measured fracture load. Table 5 shows the results of twenty seven trials under perturbed alignment directions, for all four specimens. In some cases, these small perturbations in alignment angle ( $\pm 5^\circ$ ) resulted in very large differences in predicted fracture load, up to 47% relative to a model aligned without error. A total of 108 trials were performed, and 50% of these trials demonstrated significant ( $>20\%$ ) differences in fracture load compared to a model aligned without error.

Table 5 Effects of alignment error on FE computed fracture load for specimen 2 and 3, the strongest and weakest of the femurs, respectively. For all twenty seven cases, a percent error was computed relative to a model aligned with no error (case 14). Cases with error magnitudes greater than 20% are highlighted.

Trial Number	S Error	CCD Error	AV Error	%Error in Fracture Load			
				Specimen			
				1	2	3	4
1	5 °	5 °	5 °	30.9%	-11%	18%	-19%
2	5 °	5 °	0 °	36%	-16%	32%	-17%
3	5 °	5 °	-5 °	32%	-21%	47%	-20%
4	5 °	0 °	5 °	-1.4%	-3.5%	5.9%	-1%
5	5 °	0 °	0 °	-0.9%	-13%	15%	-1%
6	5 °	0 °	-5 °	0.5%	-20%	27%	-5%
7	5 °	-5 °	5 °	-23%	-5%	-5.9%	21%
8	5 °	-5 °	0 °	-23%	-18%	0.0%	12%
9	5 °	-5 °	-5 °	-22%	-27%	8.8%	-3.3%
10	0 °	5 °	5 °	40%	-3.5%	0.0%	-14%
11	0 °	5 °	0 °	32%	-2.4%	8.8%	-15%
12	0 °	5 °	-5 °	30%	-8.0%	23.5%	-17%
13	0 °	0 °	5 °	1.8%	7.7%	-5.9%	0.2%
14	0 °	0 °	0 °	0%	-0%	0%	0
15	0 °	0 °	-5 °	-1.4%	-8.0%	11.8%	0.2%
16	0 °	-5 °	5 °	-22%	5.5%	-14.7%	12%
17	0 °	-5 °	0 °	-22%	-2.4%	-8.8%	20%
18	0 °	-5 °	-5 °	-21%	-16%	0.0%	11%
19	-5 °	5 °	5 °	32%	-8.0%	-14.7%	-13%
20	-5 °	5 °	0 °	24%	-2.4%	-5.9%	-12%
21	-5 °	5 °	-5 °	17%	-0.1%	2.9%	-13%
22	-5 °	0 °	5 °	0.9%	4.4%	-18%	-4.9%
23	-5 °	0 °	0 °	-2.7%	10%	-8.8%	2.4%
24	-5 °	0 °	-5 °	-6.8%	4.4%	0.0%	0.8%
25	-5 °	-5 °	5 °	-21%	-0.1%	-21%	2.4%
26	-5 °	-5 °	0 °	-23%	2.1%	-15%	15.4%
27	-5 °	-5 °	-5 °	-25%	-2.4%	-5.9%	23.6%

As a result, this study also found that positioning by visual approximation was unreliable.

Positioning errors varied greatly between trials, with individual alignment angles up to 30° away

from alignment targets. Only one of 24 trials, across four different specimens, achieved all alignment angles to within 5° of the targets (Figure 25).

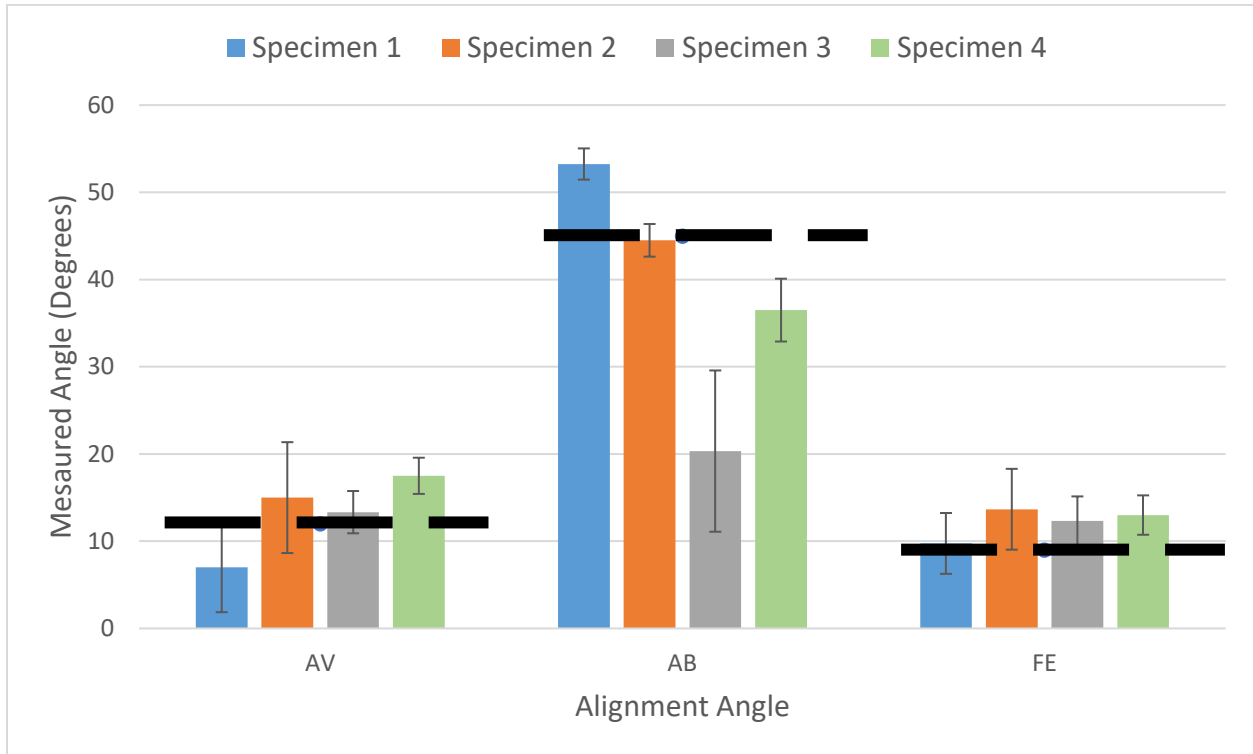


Figure 25 Average femoral AV, AD and FL angles achieved by visual orientation, compared to target angles (dashed lines). Error bars show SD between trial repetitions.

As expected, these alignment errors resulted in large differences in FE computed fracture load. Compared to a model aligned with no error, differences across all specimens and trials varied greatly (0%-50% difference compared to a model aligned without error). Average error across all six alignment repetitions was over 15% for three of the four specimens (Figure 26).

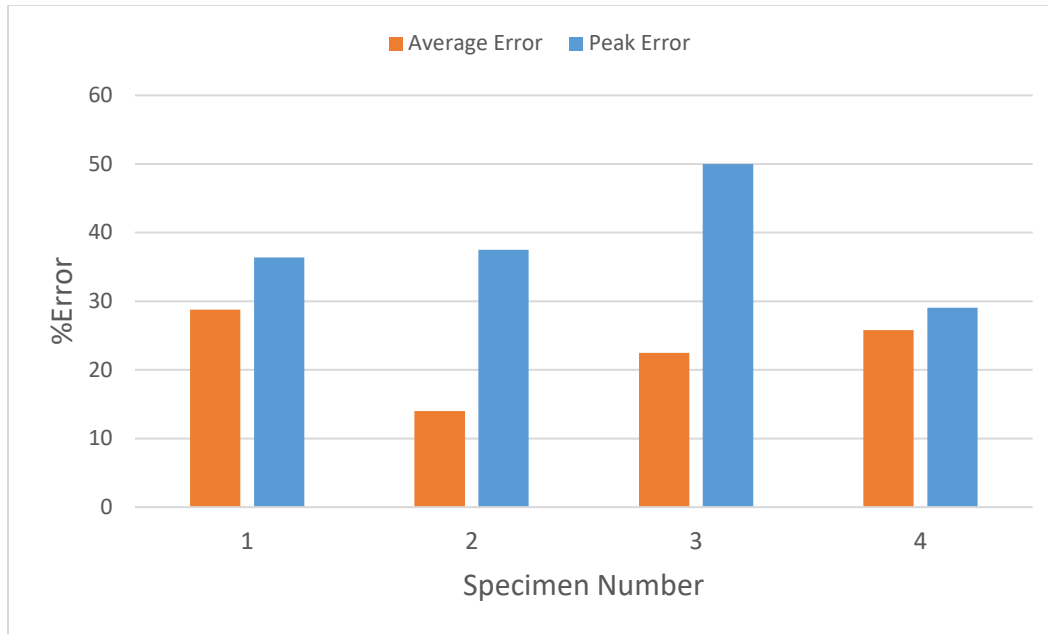


Figure 26 Average and peak errors due to visual alignments. For each of the four specimens, visual alignment was performed six times. FE computed fracture load from each alignment was compared to a model aligned with no error. Average error over all six trials (orange) and peak, or worst case, error (blue) are shown.

In response to these findings, a more accurate positioning method was developed, using an optical motion tracking system to display angles in real-time while the femur was placed into the neutral position (in section 4.2.2). With this method, physical positioning of the cadaveric specimens was very repeatable; each of the four specimens were physically oriented three times to within one degree of the target angle, with SD no greater than  $0.58^\circ$ . Identification of the neck and shaft axes, however, was a more dominant source of repeatability error. Axis identification was repeated three times for each of the four femurs, and these repetitions resulted in axes that were, on average,  $1.3^\circ$  apart, with a worst-case difference of  $3^\circ$ .

## 4.4. Discussion

### 4.4.1. Influence of Muscle Forces

This phase of the study attempted to estimate muscle forces from stumbling, and assess whether inclusion of muscle forces can affect FE predictions of proximal femur fracture. This particular loading scenario was chosen because it yielded the highest hip contact forces of any activity measured *in-vivo* [29], [30]. Noting the relationship between hip contact force and muscle force magnitudes (Equation 1, section 2.1.4), this loading scenario was likely to have higher magnitude muscle forces compared to more common activities, increasing the potential for effects on fracture load. Muscle forces were estimated using a physiological model developed by a trained anatomist [134], combined with *in-vivo* hip contact force measurements. However, this study found that inclusion of these forces into FE simulations had a measurable, but ultimately negligible, effect on proximal femoral strain and estimated fracture load (<3% difference).

This result is consistent with a previous FE study, which looked at the effect of muscle forces during walking [48] and found similar results. The study noted that inclusion of muscle forces had an effect on proximal femur strains but, in the authors' words, the effects were "quite moderate". However, a more quantitative comparison was not provided. To the best of the author's knowledge, no other studies have looked at the effect of muscle forces on proximal femur strain during physiological loading conditions. Other studies have investigated the influence of muscle forces on strains in the shaft [48]. These studies have found that simplified boundary conditions, with muscle forces excluded, results in an overestimation of femoral shaft strains [60], [61]. However, the shaft is typically the strongest part of the femur and failures here are considered to be atypical, in a clinical setting [10].

It remains challenging to precisely predict muscle forces during stumbling. While Equations 1-9 (Section 2.1.4) are well understood, and commonly used in the literature [47], [54], [56], [139], they require measurements of joint acceleration and ground reaction force, none of which were available for realistic stumbling events. Instead, a set of reasonable assumptions were made based on video footage from the worst of two observed stumbling events [30]. Muscle forces had a very minimal effect on FE prediction of peak strain and fracture load (<3%), compared to a model that included only the hip contact force. Thus, sensitivity to these assumptions were not investigated in greater detail.

#### **4.4.2. Influence of Alignment Errors**

The first objective of this phase was to determine whether it was possible for small alignment errors to have a non-negligible effect on fracture load. This was done by modeling a femur in the neutral position, then perturbing the alignment angles and comparing FE computed fracture load between models. It was found that even relatively small alignment errors can have non-negligible effects on fracture load. Over 50% of the 108 trials had moderate to large errors (20-47%), relative to a model aligned without error. While this investigation focused on the impact in measured fracture load, the conclusions drawn could translate to other common measurements such as stress or strain in the femur. These results demonstrate that there is a need to develop an accurate and repeatable method for femoral alignment, as even relatively small errors can cause non-negligible changes in experimental predictions.

Accurate alignment is particularly challenging when the study relies on mechanical testing of cadaveric specimens. This study noted that many recent investigations [15], [18], [19], [48] do not fully define how the femur is oriented, or how the orientations are achieved in an experimental test. Even if target alignment angles were well defined, it is challenging to achieve

those angles with accuracy and repeatability; given the lack of reported information, the author presumed that visual approximation played some role in these studies. Another objective of this study was to characterize alignment errors from visual approximation alone. This was done using an optical motion tracking system, which reported alignment angles of cadaveric specimens while they were manually positioned by visual approximation. It was found that visual approximation is extremely inaccurate, and individual trials had alignment errors up to 30°. As a result, the average error in FE computed fracture load was between 20-30% for three of the four specimens investigated.

Together, these findings demonstrated the need to develop a more accurate and repeatable method of positioning cadaveric specimens. This was done using optical motion tracking equipment, which was able to record the orientation of the specimens in real time, and allowed the operator to orient the specimen to within one degree of the target angles ( $SD < 0.58^\circ$ ). The reference axes could also be identified with great repeatability, with a less than 3° difference between trials (mean difference=1.3°). It should be noted, however, that such high repeatability was achieved when the repetitions were performed by a single investigator, i.e., the author. It is expected that repeatability may be somewhat worse when comparing different investigators, though additional unbiased investigators were not available to test this hypothesis.

While the positioning method presented in this paper is accurate, it comes with additional costs. It requires an optical motion tracking system which may not be easily available to many biomechanics labs. It also adds significantly to the time needed to test each specimen. In the following chapter, six specimens were tested to failure using this method for femoral alignment. It was estimated that the additional steps introduced in the alignment procedure accounted for approximately a third of the total experiment time, i.e., one hour was spent on alignment

procedure for a test that took, on average, three hours in total. Depending on the design and objectives of the study, these additional costs may not be necessary. Some studies use large sample sizes ( $n > 50$ ) in order to compare groups [140], or seek statistically significant correlation between variables [13]. Such studies often find statistically significant results despite large specimen-to-specimen variation, of which variation due to alignment error may be only a small factor. The author speculates that improved alignment techniques may not have a large impact on the results of these studies.

Other studies, however, rely on small sample sizes and seek more quantitative conclusions; these studies are more likely to benefit most from accurate alignment. Model validation studies, such as the one performed in Chapter 6, often fall into this category. These studies commonly use a small number of specimens ( $n$  of 1-20) [17], [18], [80], [81], [91] to quantify performance of a computational model. Accurate specimen alignment procedures may allow these studies to accurately quantify model performance when a large number of donors are not available.

Finally, some additional limitations of the specimen alignment procedure should be noted. Femoral positioning angle targets were averaged from measurements taken by Bergman et al [29]; this data was gathered from a relatively small ( $n=9$ ) group of participants and may not be representative of a population as a whole. Moreover, AV angle varied greatly from specimen-to-specimen and using the average value may not be accurate for all specimens. However, this data still represents a reasonable approximation of the neutral position, particularly when no other information is available. It is possible that future studies could be designed with these issues in mind. For example, if specimens are intentionally harvested with the knee condyles intact, these

could be used to determine the specific AV, FE, and AD alignment angles for the individual [48], [133], before being cut away to mount the specimen for testing.

## Chapter 5: Development and Validation of a FE model to predict bone fracture using a Quasi-brittle damage model

Significant portions of this chapter have been submitted for publication in the Journal of Biomechanics:

**Haider, I. T.**, Goldak, J., & Frei, H. (2016). Femoral Fracture Load and Fracture Pattern is Accurately Predicted using a Gradient-Enhanced Quasi-Brittle Finite Element Model. *Journal of Biomechanics*. **In peer review.**

### 5.1. Introduction

The previous chapters used FE modelling to investigate many effects that are commonly neglected from *in-vitro* studies of hip fracture. Fracture load was estimated using a criterion developed for use with linear elastic models, i.e., failure of bone material was not simulated. This technique is computationally inexpensive and commonly used in the literature [15], [92], [94], [96]. Linear models are able to accurately predict strains at low loads [67], and achieve strong correlations between FE predicted and experimentally determined failure load. As a result, these models are a powerful and effective tool for studying relative effects of different conditions, as was done in previous chapters. However, these models have some important limitations. Despite the strength of correlation, error magnitudes can remain quite large and some studies show that individual specimens have differences of up to 45% between predicted and experimentally measured fracture loads [15], [96]. These models are also poorly suited for studying the mechanisms behind bone fracture at the organ level, as they are not able to accurately model the behaviour of material as it nears failure.

These limitations could potentially be overcome using more advanced FE models, with nonlinear material properties. As mentioned in section 2.3.1, these models attempt to simulate

the failure by degrading element material properties as strains approach or exceed the failure criterion [17], [18], [91], [97]. However, there is currently little consensus regarding the best material model and failure criterion to use for modelling failure of the proximal femur.

Some very recent studies [80], [81] have had success using a quasi-brittle damage model, where stiffness of elements degrades gradually as strain increases, and the crack is modelled as the region of elements whose stiffness has been reduced to near zero. While the technique is powerful, there are important challenges that need to be addressed. FE models that include strain softening behaviour have well documented issues with spurious mesh sensitivity. The size of the damaged region corresponds to the size of the mesh used to solve the problem. As the mesh is refined, the size of the damaged region, and thus the energy dissipated, shrinks. This is a physically inadmissible result; the energy dissipated by crack formation is a property of the structure and should not be dependent on mesh size [109], [110].

As discussed in section 2.3.4, this issue can be remedied using a non-local constitutive model. For example, damage evolution can be driven by a weighted spatial averaging of strains near a point, rather than the local strain at the point itself. This technique has been used successfully for simulations of vertebral bone [111], but is difficult to implement within a conventional finite element solver. As an alternative, gradient-dependent descriptions have recently gained interest. Using Taylor series expansions, these models approximate the nonlocal parameter as the solution to a differential equation which can be evaluated locally [112]. This equation can be easily coupled to the equation of equilibrium and solved using the finite element method.

While this method has been used successfully in the past to model failures in quasi-brittle engineering materials [113], to the best of the author’s knowledge, it has not been used to study bone fracture at the organ level. Thus, the purpose of this study is to develop specimen-specific finite element models of the femur, simulate fracture using a gradient-enhanced quasi-brittle damage model, and validate the predicted fracture load and fracture pattern through experimental testing.

## 5.2. Methods

### 5.2.1. Developing a Specimen-Specific FE model

Six specimen-specific models were developed from cadaveric femurs obtained from the University of Ottawa’s division of clinical and functional anatomy, after approval from their research ethics board (Mean age 75, SD=13). Procedures for image segmentation, mesh generation, and assignment of undamaged material properties were discussed in the previous chapter (section 4.2.2). The resulting tetrahedral meshes consisted of approximately 98000 elements, with an average edge length of 2.5 mm. To verify convergence of the mesh, one specimen was also modelled with average element edge lengths of 3.5 mm and 1.5 mm (Appendix B).

Damage evolution was modelled as a function of nonlocal equivalent strain as:

$$D = 100 \cdot \varepsilon_{eq}^{1.25} \quad (43)$$

The form of the equation is similar to that used in previous quasi-brittle damage models of bone [80]. The damage exponent of 1.25 was adopted from a study of microdamage in trabecular bone [32], [81], and the damage coefficient of 100 was selected based on compression tests of trabecular

bone [141]. This combination of parameters causes ultimate stress predicted by the model to closely match average measured ultimate stress (<1% difference), and reasonably predicts the 0.5% offset yield stress and strain (<10% difference).

Finally, the model must be able to account for strength asymmetry of bone in tension vs compression. This was done through selection of the equivalent strain definition. This study used the modified von Mises strain, described by Vree et al. [142], which has been used successfully in the past to model concrete [113]:

$$\varepsilon_{eq} = \frac{k-1}{2k(1-2\nu)}J_1 + \frac{1}{2k}\sqrt{\left(\frac{k-1}{1-2\nu}J_1\right)^2 + \frac{12k}{(1+\nu)^2}J'_2} \quad (44)$$

Where k is the ratio of compressive vs. tensile stress, taken to be 1.2 for bone [141], and  $J_1$  and  $J'_2$  are strain invariants defined as:

$$J_1 = \varepsilon_{xx} + \varepsilon_{yy} + \varepsilon_{zz} \quad (45)$$

$$J'_2 = \frac{1}{3}\left(\varepsilon_{xx}^2 + \varepsilon_{yy}^2 + \varepsilon_{zz}^2 - \varepsilon_{xx}\varepsilon_{yy} - \varepsilon_{yy}\varepsilon_{zz} - \varepsilon_{zz}\varepsilon_{xx} + 3(\varepsilon_{xy}^2 + \varepsilon_{yz}^2 + \varepsilon_{zx}^2)\right) \quad (46)$$

An ABAQUS custom element subroutine (UEL) was written to incorporate the material properties above into the gradient enhanced custom finite element described in section 2.3.4.

The FE model of the femur was rotated into the neutral position using the technique described in section 3.2.5, and boundary conditions were assigned in order to simulate the effect of stumbling loads [29], [30]. In the FE model, a small number of elements on the proximal head were subject to displacement boundary conditions in the direction of this applied load, while the distal end of the shaft was fully fixed below the lesser trochanter. To limit unrealistic collapse of the femoral head at the loaded nodes, which may also result in convergence issues, damage was

disabled over a small region surrounding the loaded nodes (diameter = 1 cm). Simulation was allowed to continue until the model failed to converge. Previous studies have noted that damage progression and fracture is often associated with a sudden loss of structural stiffness [113], which causes convergence difficulties when using a Newton Raphson iteration scheme. This behaviour, however, signifies the onset of a sudden drop in applied load, which occurs after peak load has been achieved (Figure 29). Thus, fracture load was identified as the highest net reaction force achieved during the simulation history.

### **5.2.2. Experimental Validation**

The accuracy of the FE model was assessed by comparing the simulation results to that of an in-vitro test done using the same specimens. The goal of the experiment was to replicate the boundary conditions of the FE model as accurately as possible. Thus the optical motion tracking and position system, described in detail in section 4.2.2, was used to orient the femur and ensure that loading direction in the tests matched the FE model load directions as closely as possible.

A servo-hydraulic test frame was used to load the oriented specimens. The base of each specimen was potted in approximately 50 mm [2 in] of dental stone, and a displacement controlled load (1 mm/s) was applied to the femoral head. Preliminary testing showed that load applied directly to the femoral head would often cause it to collapse in a manner that is not commonly seen in vivo. To mitigate this effect, loads were distributed using a tennis ball cut into halves. Both halves were placed on the femoral head, after the top half was coated in dental stone in order to resist highly localized deformation (Figure 27). Examples of typical load-displacement curves are shown in Figure 29.

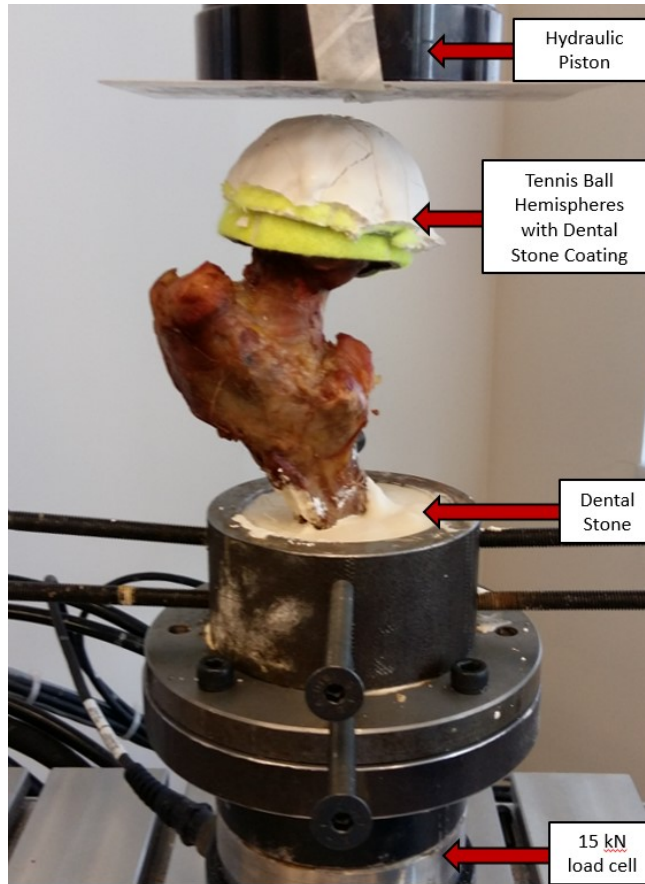


Figure 27 Experimental Setup. The base of the specimen was potted in approximately 50 mm of dental stone. Two tennis ball halves were placed on the femoral head, and the top was coated with dental stone in order to more evenly distribute loads from the hydraulic piston head. Reaction force was measured using a 15 kN load cell.

After testing, the average absolute error between the experimental test and FE prediction was computed, the definition for which was adopted from a recent review of accuracy in FE modelling [143]:

$$E_{avg} = \frac{|F_i - F_0|_1}{F_0} \times 100 \quad (47)$$

Where  $E_{avg}$  is the averaged error across all specimens,  $F_i$  is the FE computed fracture load for the  $i^{th}$  specimen, and  $F_0$  is the experimentally measured fracture load of the specimen.  $|F_i - F_0|_1$  is the L-1 norm of the set  $F_i - F_0$ . Similarly, a worst case or peak error was computed as:

$$E_{max} = \frac{|F_i - F_0|_{\infty}}{F_0} \times 100 \quad (48)$$

Where  $|F_i - F_0|_{\infty}$  the L-infinity norm of the set  $F_i - F_0$ . After testing, it was found that peak force occurred with relatively little surface damage, which is discussed in greater detail in the following section. However, it was hypothesized that structurally significant damage was occurring in the trabecular bone under the surface. Available femurs were qCT scanned again (0.6 mm slice thickness and 0.55 mm in-plane resolution) and scans taken before and after failure were compared to the FE predictions. Unfortunately, two of the tested femurs had suffered severe compaction of the femoral head, making it difficult to identify trabecular structures after failure, while a third specimen was not included in this study until after these scans.

### 5.2.3. Comparison to Linear Elastic FE Model

As expected, preliminary simulations revealed that the quasi-brittle model developed in this study was significantly more computationally intensive than the linear elastic (LE) models used in Chapters 3 and 4. A set of models were developed to compare the two techniques, and determine whether the additional costs of the quasi-brittle model are justified. The six specimens specific models developed for this study were modified to disable damage progression, and failure was determined using the linear elastic criterion described in Section 3.2. Average and peak errors (equations 47 and 48) were recalculated with fracture load predictions made by the LE models, and compared to results from the quasi-brittle model.

### 5.3. Results

Table 6 summarizes the experimental and FE computed fracture loads. The FE model had excellent agreement with the experimental results, with a very strong correlation coefficient ( $R^2=0.79$ , Figure 28), and errors less than 14% over all specimens. The average percentage error for this study was found to be only 9.6%. Unfortunately, comparisons between experimental and FE predicted stiffness were not possible. In the experiment, very compliant materials (tennis balls) were used to distribute the applied load; deformation of this material confounded the measurement of femoral head displacement, resulting in an underprediction of femoral stiffness. However, the FE computed stiffness (mean=7.0 kN/mm, min=4.0 kN/mm, max=10.5 kN/mm) was consistent with values previously reported in the literature [17].

Table 6 Comparison between experimentally measured and FE predicted fracture load. The model performed well overall, with an average error of 9.6% and peak error of only 14%.

Specimen Number	Measured Fracture Load [kN]	FE predicted fracture load [kN]	% Error
1	7.3	7.8	6.8%
2	11	12.5	<b>14%</b>
3	6.0	5.3	12%
4	9.5	8.3	13%
5	5.5	5.5	0%
6	6.2	5.4	13%

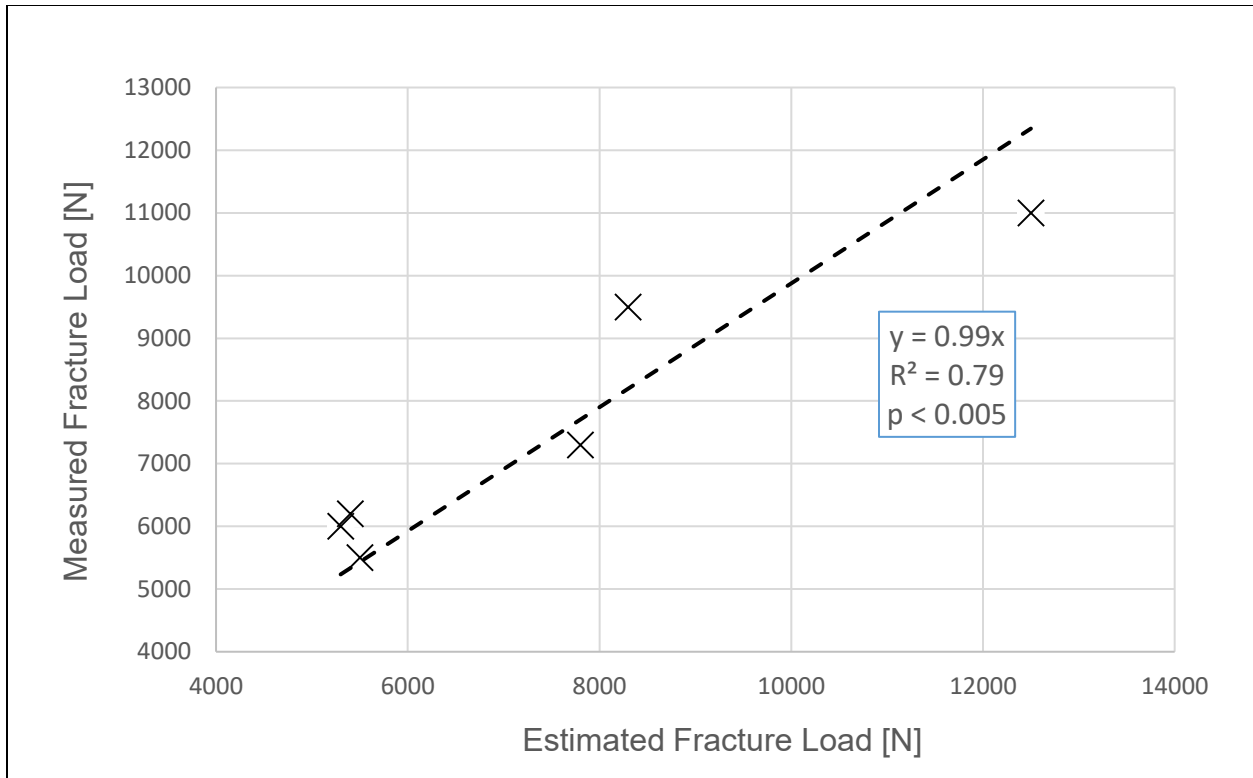


Figure 28 Correlation between measured and predicted fracture loads. As expected, the slope of the best-fit line was very close to 1 ( $m=0.99$ ), and the correlation was very strong ( $R^2=0.79$ ).

Overall fracture pattern was also well predicted. Simulating crack propagation and growth was difficult, as the initiation of fracture causes a very sharp decline in stiffness and structural integrity of the bone (Figure 29). It is very difficult to simulate past this failure point using Newton Raphson iterations, and some simulations did not reach 40% (peak stress) or 99% (complete failure) in more than a few surface elements. However, in all cases the region of greatest surface damage corresponded to the location of surface fracture seen in the experiment.

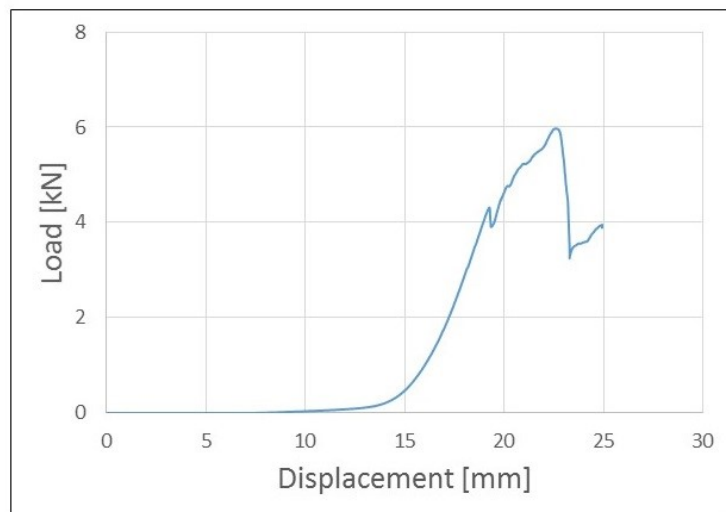
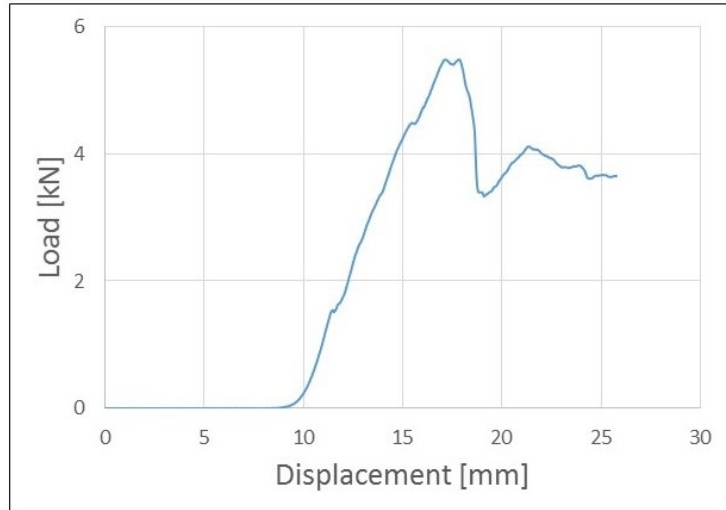


Figure 29 Experimentally determined fracture pattern (LEFT) and corresponding load-displacement measurement (RIGHT). Specimen 5 (TOP), randomly selected to be the first tested, was loaded long after peak force was achieved, resulting in compaction of the subcapital bone. Subsequent tests, such as specimen 3 (BOTTOM) were stopped soon after peak force was achieved.

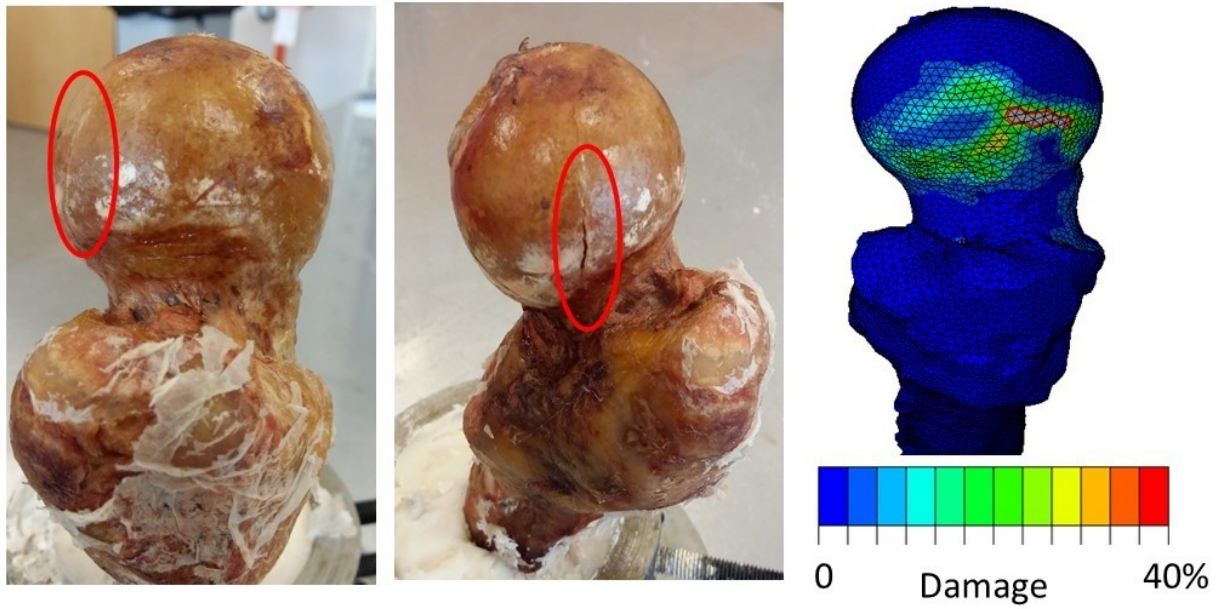


Figure 30 Cadaveric specimen 1 before (LEFT) and after (MIDDLE) testing. FE predictions of surface damage (RIGHT) did not match the location of the crack observed in the experiment. However, the crack appears to have nucleated along a pre-existing gouge in the bone.

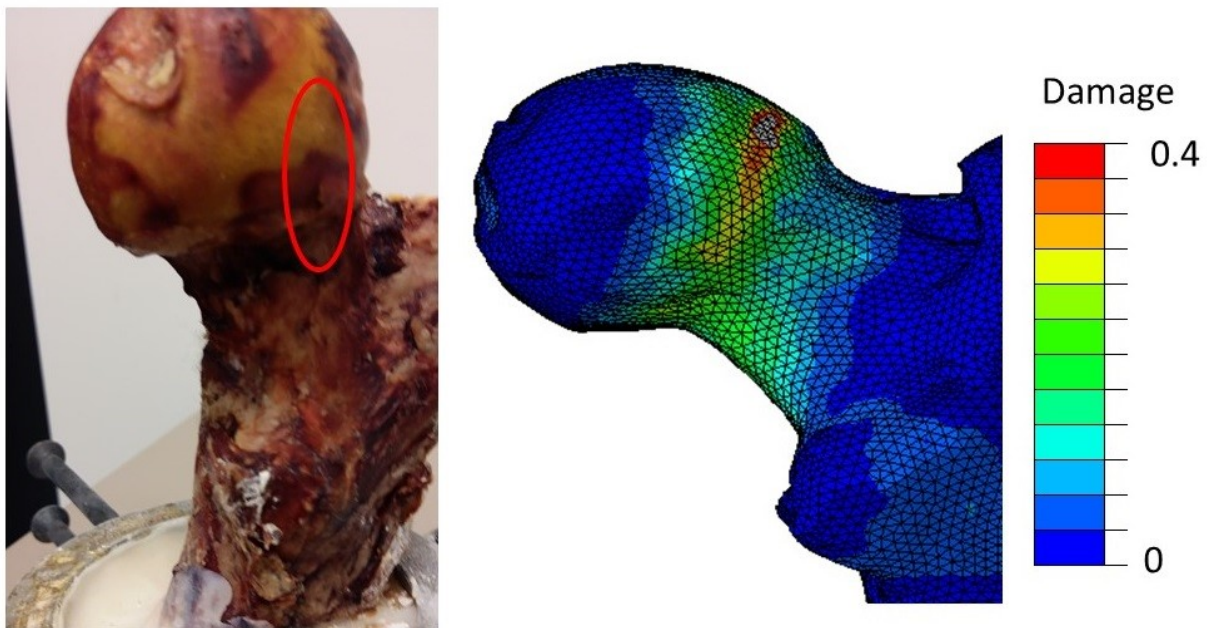


Figure 31 Experimentally determined fracture pattern (LEFT) compared to FE predicted fracture pattern (RIGHT) for Specimen 2. Damage was predicted to occur along the posterior edge of the subcapital bone; the experimentally observed surface damage occurred within this region.

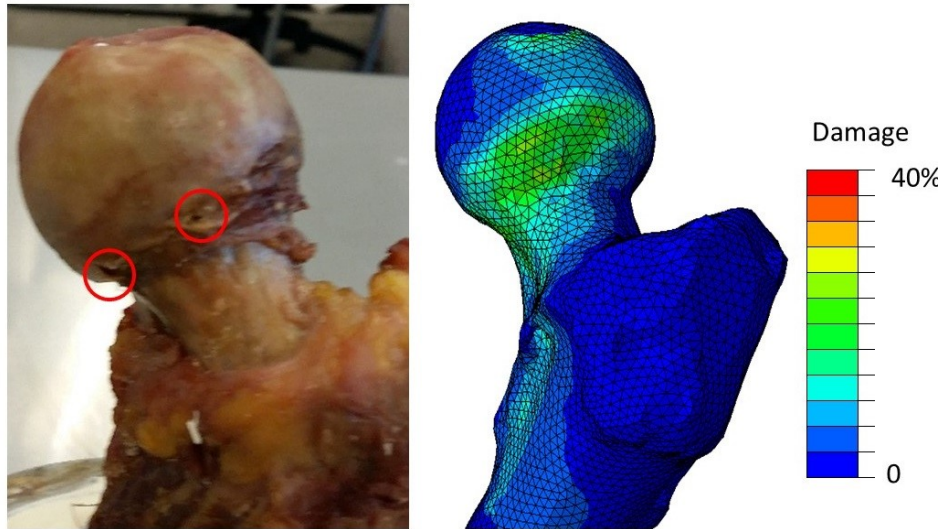


Figure 32 Experimentally determined fracture pattern (LEFT) compared to FE predicted fracture pattern (RIGHT) for Specimen 3. No simulation elements reached peak load, but surface damage was predicted to occur in the superior-anterior subcapital bone, which is consistent with the location of visible damage.

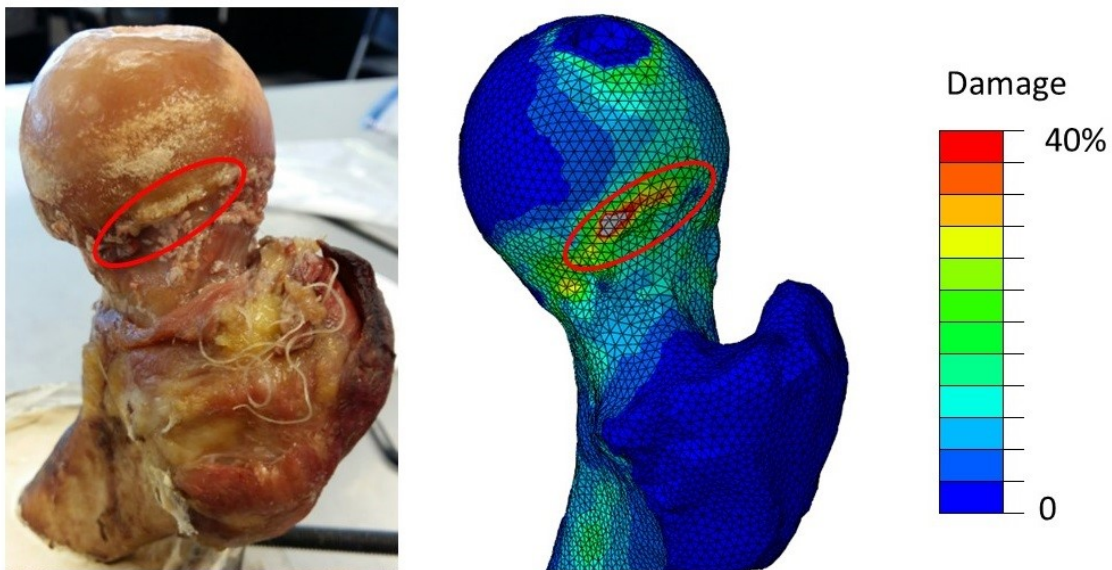


Figure 33 Experimentally determined fracture pattern (LEFT) compared to FE predicted fracture pattern (RIGHT) for Specimen 4. The predicted surface damage pattern closely matched the experimental result. While difficult to identify visually, the presence of the crack was confirmed by tactile inspection. Bone in the circled region was originally smooth to the touch, but felt jagged after loading.

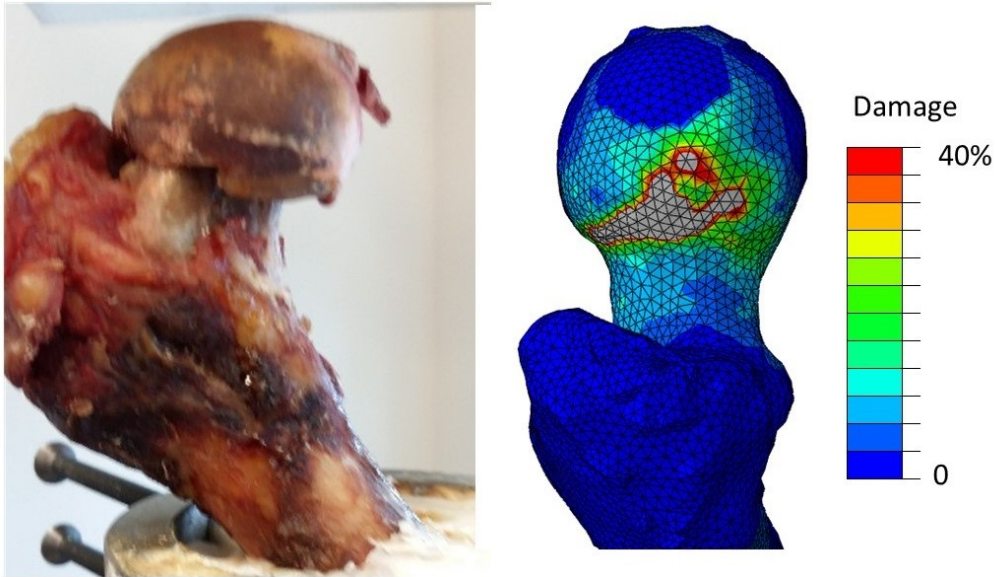


Figure 34 Experimentally determined fracture pattern (LEFT) compared to FE predicted fracture pattern (RIGHT) for Specimen 5. The model predicted failure of the superior subcapital region at the time of peak loaded. This specimen, however, was loaded long past that point (Figure 29) and experienced a complete collapse of subcapital bone.

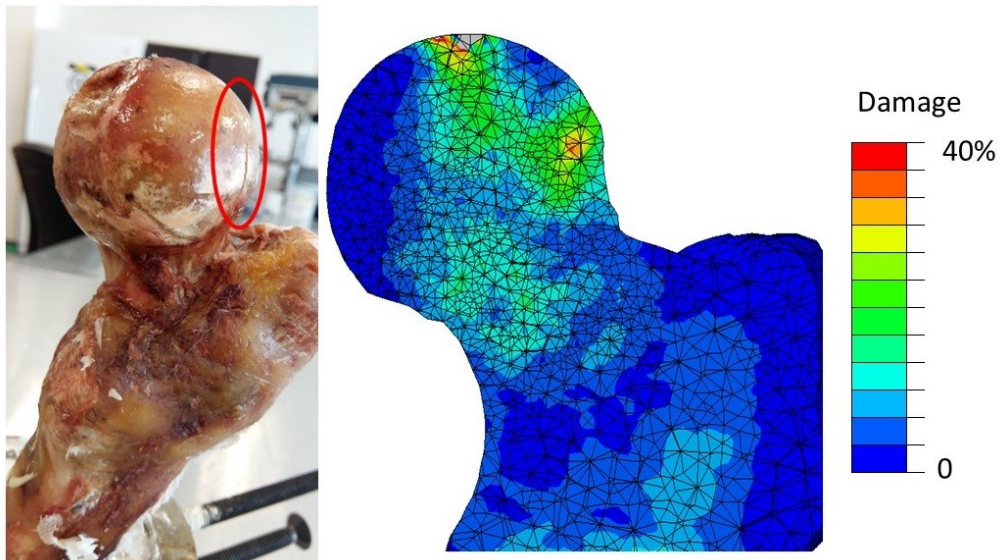


Figure 35 Experimentally determined fracture pattern (LEFT) compared to FE predicted fracture pattern (RIGHT) for Specimen 6. The FE model predicted a location of high damage in the superior subcapital bone, consistent with the location of the visible crack in the cadaveric specimen.

Specimen 5 was randomly selected to be the first specimen loaded during the experiment. This specimen experienced a total collapse of subcapital bone followed by compaction of the head into the femoral neck (Figure 29). While the model failed to converge soon after peak force was achieved, damage was predicted to occur in the subcapital region, consistent with the observed result. However, the experimentally observed failure pattern was obtained because the load was applied long after peak force had been achieved. This situation was unlikely to occur in vivo, as the applied forces occur due to the action of the muscles, which likely change once peak load (fracture) is reached and the patient reacts to the pain. As it is difficult to predict how forces may change after the fracture initiates, subsequent specimens were monitored and the applied displacement was stopped soon after peak load was reached. All subsequent tests (Figure 30- Figure 35) showed small, but visible, stress fractures in the superior subcapital region. The exact location of the surface fractures were difficult to predict. However, the general location (subcapital bone) and facing (superior vs. inferior, anterior vs. posterior) of the surface cracks were consistent with FE predictions. The only exception was specimen 1 (Figure 30), which failed at a pre-existing gouge in the bone, which likely occurred during specimen preparation but was too shallow to appear in the FE model.

In most cases, the surface damage appeared quite minor. However, a subsequent CT scan of three specimens showed that more significant damage had occurred in the trabecular bone under the cortex (Figure 36). In all three imaged cases, damage was identified in the proximal subcapital region, consistent with the FE predicted damage initiation site.

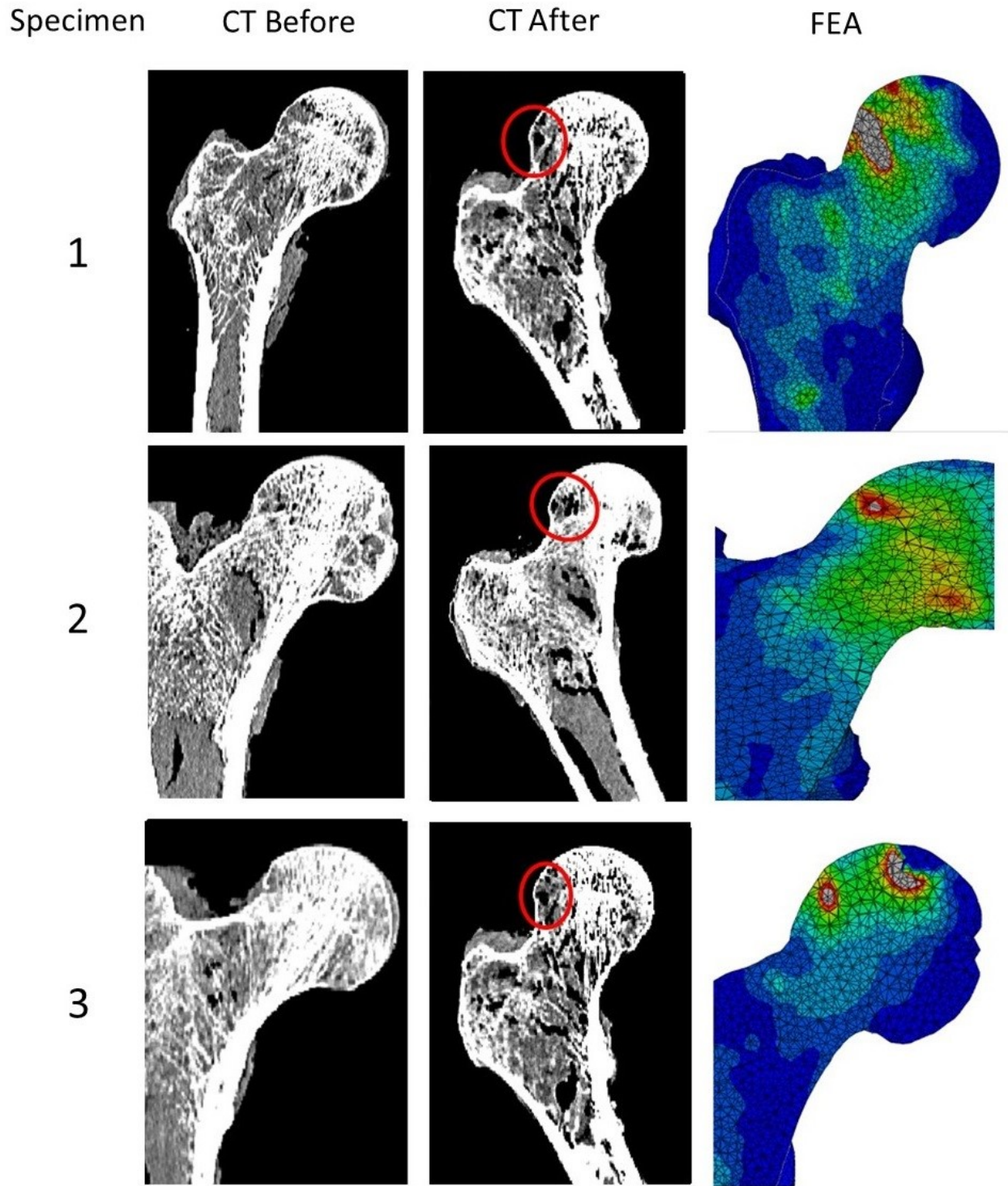


Figure 36 Comparisons of CT scans before fracture (LEFT), after fracture (MIDDLE), and FE predicted fracture patterns (RIGHT). In all three cases, damage was observed in the superior subcapital region, consistent with the FE predictions.

**5.4.** As expected, the LE models did not perform as well as the quasi-brittle model developed in this study. Average and peak fracture load prediction errors of the LE models were 33% and 70%, respectively. This was significantly worse than the quasi-brittle models, where average and peak errors were only 9.6% and 15%, respectively. **Discussion**

The purpose of this study was to develop and experimentally validate a nonlocal continuum damage model to predict hip fractures. Overall, the model presented in this study performed extremely well, with an average error of 9.6% and strong agreement between predicted and measured fracture patterns. This was a significant improvement over the simpler LE models, which had an average error of 33%. The model was developed based on previous work by Hambli et al., who showed that quasi-brittle damage modelling was a promising technique for prediction of bone fracture [80], [144]. This model presented in this study, however, overcomes some of the limitations in these previous works.

The most important limitation is related to mesh sensitivity, which is a well-documented challenge that is faced when using FE methods with quasi-brittle materials. As the mesh is refined, the failed region and predicted energy dissipation shrinks to physically unrealistic values [109]. Hambli et al. [80] adjusted the failure strain of each element based on element size, in an effort to correct for this effect. This was only partially effective as the predicted path of the crack remained quite sensitive to mesh refinement. The nonlocal damage model used in this present study, however, was previously shown to be very successful at eliminating this effect, with predicted fracture load, fracture pattern, and fracture initiation site all independent of mesh density [113]. Another important limitation of these previous quasi-brittle models is that accurate validation against multiple specimens was achieved by fitting model parameters based on experimental results [80]. In the present study, accurate (9.6% average error) fracture load and

fracture pattern predictions were obtained using material properties obtained *a-priori*, with no fitting or parameter adjustments made after the validation experiments.

To the best of the author's knowledge, no other studies use continuum damage mechanics to predict femoral fracture. However, other techniques involving both linear and nonlinear models are quite common in the literature. A recent review [16] found that the average percentage errors in predicted fracture load commonly range from 10%-20% in previously published studies, and fracture location is correctly predicted only 60-80% of the time. The results of this study appear to be superior, with an averaged error of only 9.6% and correct fracture pattern predictions for all test specimens.

Another important novelty of this study was that predicted trabecular damage patterns were validated through CT scans. All imaged specimens showed damage in the superior subcapital region consistent with the FE predictions (Figure 36). Some noteworthy discrepancies were found, however. In addition to subcapital damage, the imaged bones often showed additional trabecular bone damage at the inferior subcapital region and the intertrochanteric region. It is hypothesized that this may have occurred because the FE model fails just before peak force is reached, while the experiment cannot be stopped until slightly after peak force is reached (Figure 29). This behaviour was particularly apparent in specimens 1 and 3 (Figure 36), and made comparison to FE models challenging. These specimens suffered widespread trabecular damage, making it difficult to prove that the sites identified by the FE model were the first to fail. Specimen 2, however, suffered damage in only a small number of highly localized sites which correspond extremely well with FE prediction (Figure 36).

Damage to the surface of the bone was somewhat more difficult to predict. While the experimentally observed failure initiation site corresponded to FE predicted sites of diffuse surface damage, the exact crack initiation site was rarely identified. Again, this may be because the FE simulations failed to converge just before peak load was reached. However, it is also likely that surface damage patterns are influenced by small surface imperfections not visible in the FE model. These imperfections can be naturally occurring, but they also occur when the surface is damaged during specimen harvest and preparation. Cases of the latter were observed in all specimens. Limitations on CT scan resolution, combined with the potential for small errors in the automatic segmentation algorithm, make it difficult to incorporate these superficial imperfections into an FE model.

While previous studies commonly validate FE models in a stance loading configuration [17], [18], [73], [81], [96], this study chose to use a loading direction based on peak forces during stumbling. This may be more clinically significant as this loading scenario represents some of the highest hip contact forces measured *in-vivo* [30]. The experiments predicted failure to occur in the subcapital region, which is a commonly observed failure site in clinical settings [145], [146]. Specimen 5 (Figure 34) was loaded well past the peak force resulting in an undisplaced, impacted fracture. In a clinical setting, impacted fractures have been found to occur in approximately 20% of subcapital fracture cases [146]. However, this study also found that peak force could be exceeded with relatively little damage to the external cortex or change in profile shape (Figure 31-Figure 35), making the fracture difficult to detect on a radiograph. Furthermore, pain from the event may cause the patient to fall and produce an entirely different fracture pattern.

While these results are highly encouraging, the relatively small sample size of this study is an important limitation. Previous FE fracture validation studies have used between 3 and 72 femoral specimens [16], [88]. Though none of these investigations have provided mathematical justification for the number of specimens used, it may be beneficial to validate additional specimens in the future. In validating a physics-based model, however, diversity of the specimens is also an important consideration [147], [148]. Fracture load and pattern depends on a number of parameters related to density and morphology of the femur [13]. An important direction for future work may be to identify the most important parameters, and demonstrate that the model remains sufficiently accurate across different variations and permutations of these parameters.

## Chapter 6: Investigation of Risks due to Physiological loading and Damage Accumulation

### 6.1. Introduction

Significant attention has been given to falls as the primary cause of hip fracture [20]–[26], and medical studies commonly refer to hip fractures as ‘fall related injuries’ [149]. The assumption is based on evidence that the majority of hip fractures are associated with a fall [27], [28], and it is assumed that the patient falls and then breaks their hip from the impact. However, as discussed in section 2.1.3, large forces can occur in situations other than fall. The most dangerous of these appears to be stumbling, which may cause forces as high as 870% BW [30]. It is possible that these high loads cause a spontaneous fracture followed by a subsequent fall from pain or loss of joint stability. However, it remains unclear whether this hypothesized scenario occurs in reality. Patient questionnaires cannot reliably answer this question; fractures and falls occur very quickly and it is difficult to perceive which occurred first. This is compounded by the fact that many elderly patients experience mild delirium and memory loss following a fracture, and are unable to accurately recall the sequence of events leading up to the fracture [31].

While observational clinical studies cannot accurately determine the prevalence of spontaneous fractures, biomechanical modelling can still be used to determine whether such fractures are plausible. In particular, patient specific FE models can be used to simulate different physiological conditions and estimate the likelihood of suffering a fracture, though such studies are not commonly found in the literature. To the best of the author’s knowledge, only one previous study has attempted to determine the plausibility of spontaneous fractures. In 2012, Viceconti et al [31] used linear FE models to predict whether spontaneous fractures were possible due to walking loads. The study predicted fracture would occur only when the patient had both extreme

osteoporosis and extreme neuromotor degradation (abnormally high muscle forces). The study concluded that spontaneous fracture was plausible, but only 0.4% of the 80 year old population had a dangerous combination of osteoporosis and neuromotor degeneration. However, the study only considered walking loads. It is likely that other common, higher load, events would increase the likelihood of spontaneous fracture. This hypothesis is further supported by recent FE studies which compare fracture incidence in patients to FE predicted fracture loads in fall vs. stance like configurations. These studies have often found that fracture loads computed in stance-like loading configurations are better predictors of fracture risk, compared to fracture loads computed for falls [94], [140]. While these studies combined suggest the plausibility for clinically relevant spontaneous fractures, more detailed investigation is required.

Additionally, section 2.2.3 described how bone behaves as a quasi-brittle material. These materials are characterized by a progressive loss in stiffness as load increases (Equation 10). Damage is an irreversible process, and natural healing mechanisms take several days to repair bone damage [34]. It is plausible that high loads may leave the bone unfractured, but with enough accumulated damage to increase fracture risk for subsequent loading events. However, this hypothesis has not been adequately explored in the literature. Previous studies have investigated the effects repeated loading bone at the material level [33], [150]–[154], but it remains unclear how damage accumulation influences fracture load and fracture pattern at the organ level.

Thus, the purpose of this chapter is to use the quasi-brittle FE model, developed and validated in Chapter 5, to study the effects of physiological loading on fracture risk. It is hypothesized that physiological loading may play an important role in hip fracture risk; either by causing a spontaneous fracture directly, or by damaging the femur so that it is more susceptible to fracture from subsequent falls.

## 6.2. Methods

### 6.2.1. Stumbling Loads and the Effects of Worsening Osteoporosis

The first objective of this chapter was to assess the fracture risk from stumbling loads, and how it may be influenced by worsening osteoporosis. This was done using the six patient-specific FE models previously developed and validated in Chapter 5, following the procedures discussed in section 5.2.1. Unfortunately, patient weights were not available, making it difficult to determine load magnitudes. Instead, FE simulations were used to determine the maximum safe bodyweight beyond which the patient would suffer a fracture. This was compared to anthropomorphic reference data [155]; ‘fracture risk’ was estimated as the percentage of the age and gender matched population that would suffer a fracture from the event.

It was hypothesized that physiological loading would not be dangerous unless the patient is sufficiently osteoporotic. Given the relatively small sample size of this study, it was important to identify whether any of the specimens were osteopenic or osteoporotic. As DEXA scans were not available, this was done by comparing the femoral neck volumetric bone mineral density (vBMD), measured from the qCT scans described in 4.2.1. Precise definition for the region of interest (RoI) and baseline vBMD values were adopted from a previous study [156]. The mid-femoral neck was identified as the cross section, perpendicular to the femoral neck axis, where ratio of maximum to minimum diameters equaled 1.4. From this location, another slice was identified 5 mm medially along the femoral neck axis; together, these two slices formed the boundaries of the femoral neck RoI. Measurements of vBMD at this location were used to estimate a T-score, analogous to how T-score is commonly computed from DEXA measurements of aBMD [157] (section 2.2.4):

$$Tscore_{aBMD} \approx Tscore_{vBMD} = \frac{vBMD - \overline{vBMD}}{S} \quad (49)$$

Where  $vBMD$  is the femoral neck volumetric bone density measured for the individual patient,  $\overline{vBMD}$  is the corresponding average measurement for the healthy young population, and  $S$  is the standard deviation of  $vBMD$  for the entire population. Unfortunately, values for  $\overline{vBMD}$  and  $S$  were difficult to find in the literature. However, previous work [156] has reported DEXA based T-scores and average  $vBMD$  for two different age groups. Substituting these reported values into equation 49 resulted in a system of two equations with two unknowns ( $\overline{vBMD}$  and  $S$ ), which were easily solved.

These T-score values were used to simulate the effects of worsening osteoporosis, while keeping the bone density within clinically relevant limits. Previous studies on aging and bone loss have reported that cortical bone degrades by approximately 3-5% per decade while trabecular bone degrades at twice that rate, 6-10% per decade [158]. An apparent density of  $0.8 \text{ g/cm}^3$  was used to distinguish between the two types of bone [31], and the femoral neck RoI was degraded by these rates until a T-score of -3.5 (very osteoporotic) was reached; this identified a reasonable degree of bone loss, measured in decades aged. This value was used to then degrade element-averaged densities in the patient specific models in an equivalent manner:

$$BMD_{degraded} = \begin{cases} BMD_{element} \cdot 0.95^n, & \text{if } BMD_{element} \geq 0.8 \text{ g/cm}^3 \\ BMD_{element} \cdot 0.90^n, & \text{if } BMD_{element} < 0.8 \text{ g/cm}^3 \end{cases} \quad (50)$$

Where  $BMD_{element}$  is the original element volume averaged bone density, computed from qCT measured bone density (described in section 4.2.2),  $n$  is the number of decades to age the bone, estimated based on femoral neck T-score, and  $BMD_{degraded}$  is the final element average bone density used in the very osteoporotic model.

### **6.2.2. Effects of Previous Damage Accumulation on Fracture Load and Pattern**

Depending on patient weight and the loading phenomenon in question, a high risk event may leave the bone unfractured, but damaged. This phase of the study used FE models to assess the effect of previously accumulated damage on fracture risk and fracture pattern. The six previously validated quasi-brittle models (Chapter 5) were again used for this phase of the investigation. Three different scenarios, each with two consecutive loading events, were investigated: stumble followed by another stumble (Case S-S), fall followed by another fall (Case F-F), and stumble followed by a fall (Case S-F). Fracture load and pattern were compared to FE predictions if the femur failed in a single stumble (Case S) or single fall (Case F) loading event. While a multitude of loading patterns are plausible, these three were selected for further investigation as they were hypothesized to be very plausible and potentially dangerous.

For each binary event scenario (Cases S-S, F-F, and S-F), the first event was terminated at 80% of the specimen's fracture load. Damage pattern at this load was recorded and used as initial conditions for loading during the second event, which was allowed to proceed to failure. Boundary conditions for both stumble (Section 3.2.4) and fall (Section 3.2.2, case III) were described in previous sections.

## **6.3. Results**

### **6.3.1. Stumbling Loads and the Effects of Worsening Osteoporosis**

When compared to age and gender matched population weight distributions, the patient-specific FE models demonstrated a reasonable risk of fracture during stumbling (Figure 37). Moderate risk of fracture was found for four of the six specimens (1,3,5,and 6), where 37-55% of

the population group would have sufficient weight to exceed the FE predicted fracture strength. Risk was much lower for the remaining two specimens (2,4, both male), with less than 25% of the population having sufficient weight to cause a fracture. However, these risks increased dramatically when worsening osteoporosis was simulated. When bone density was degraded to a t-score of -3.5, five of six specimens were almost certain to fail (fracture risk >95%). It should be noted that the reference anthropomorphic data [155] reported weights between the 5<sup>th</sup> and 95<sup>th</sup> percentiles, thus fracture risk values lower than 5% or greater than 95% could not be estimated.

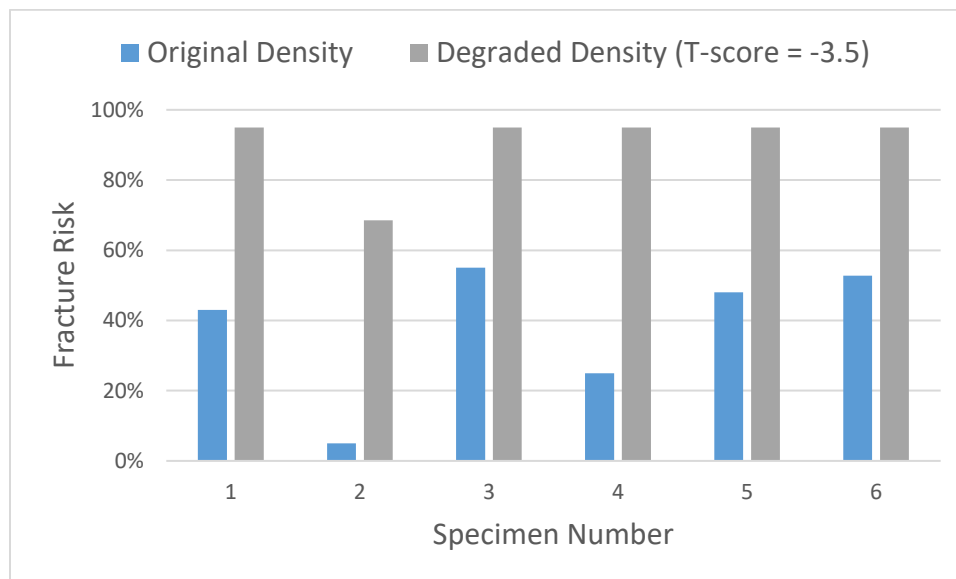


Figure 37 Risk of fracture during stumbling for specimens at original (blue) and degraded (grey) bone density levels. At original density levels, specimens 1,3,5, and 6 had a moderate risk of fracture (37-55%). When density was degraded to a T-score of -3.5, most specimens were almost certain to fracture (risk >95%).

All of the specimens in this study had below average bone density compared to that of a healthy young population. Two of the specimens were osteopenic (T-score near -1.3) while the other four were osteoporotic (T-scores between -2.5 and -3.0). However, T-score alone was a very poor indicator of fracture strength. As shown in shown in Figure 38 below, specimens 1 and 2 had the highest femoral neck vBMD and T-scores, but also had the lowest fracture strength.

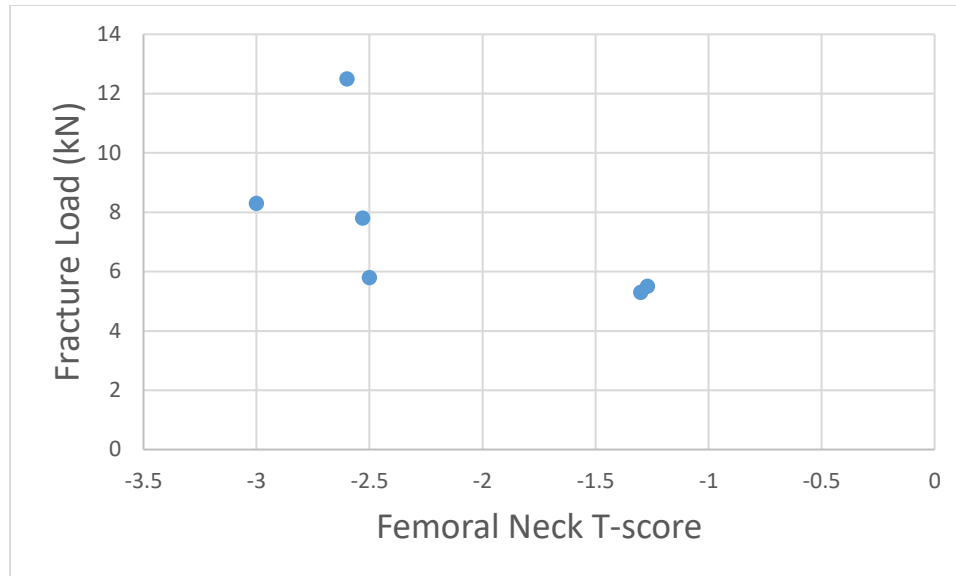


Figure 38 FE predictions of fracture load compared to T-score estimated with vBMD measured at the femoral neck. T-score alone was a poor predictor of fracture strength, and the two weakest specimens had the greatest bone density.

### 6.3.2. Effects of Previous Damage Accumulation on Fracture Load and Pattern

Figure 39 below compares fracture load predictions from each binary event load case (S-F, S-S, and F-F), to the corresponding load case where fracture occurred from a single event only (cases F, S, and F, respectively). Images showing the damage patterns from these cases are reported in Appendix C. Most specimens were extremely resilient to the effects of accumulated damage, showing little (<5%) change in fracture load from the binary event load compared to the single event load case.

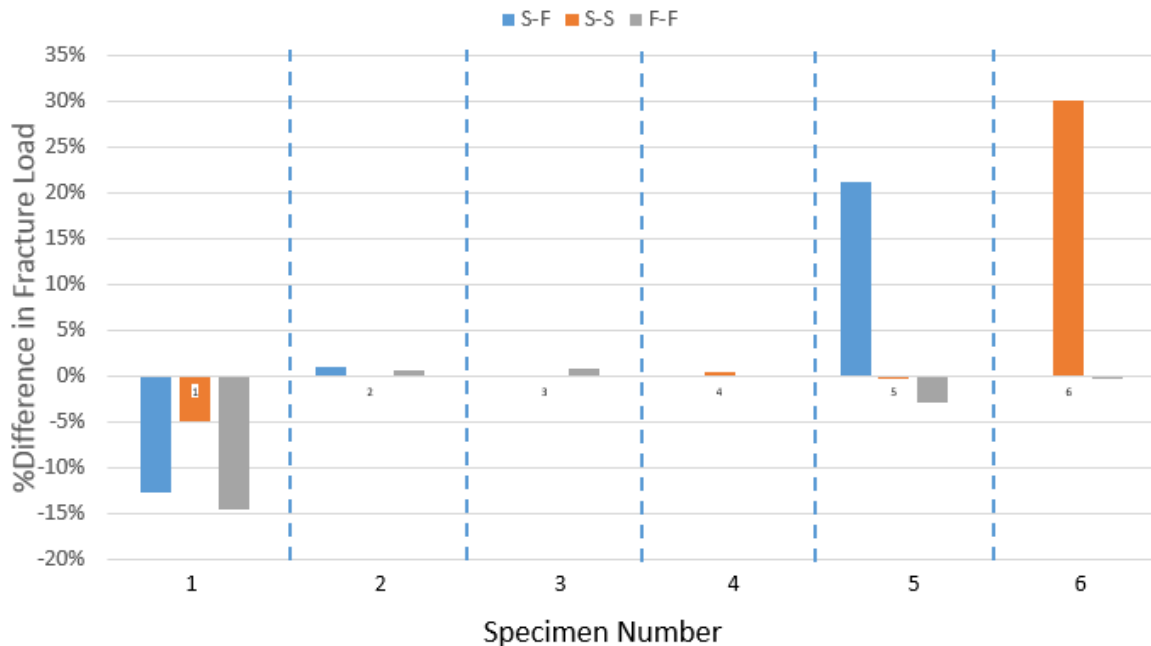


Figure 39 Percent difference in fracture load for binary loading cases S-F (blue), S-S (orange), and F-F (gray) compared to their equivalent single-event load case (F,S,and F respectively).

Surprisingly, two of the specimens experienced increases in fracture strength when loaded after previous damage accumulation. Case S-S of specimen 6, where the specimen was subject to a stumble to 80% of fracture load followed by a second stumble to complete failure, was the most prominent example of this; the specimen experienced a 30% increase in strength, compared to Case S where it was loaded to failure in a single stumble event. To explore the cause of this difference, damage patterns from Case S were compared to Case S-S. With the exception of specimen 6, damage patterns were identical between the two load cases; these patterns have been shown previously in Figure 30- Figure 35, and are also reported in Appendix C. For specimen 6, however, important differences were noted. In load case S, this specimen suffered damage in only the proximal subcapital region. In load case S-S, however, damage was more evenly distributed, with damage accumulation in both the proximal and distal subcapital region (Figure 40). This more even distribution of loading and damage likely accounts for the increased fracture

load seen in Case S-S compared to Case S, for specimen 6. A similar pattern was observed in specimen 5, where a strength increase was observed in Case S-F (stumble followed by fall) compared to Case F (fall), as shown in Figure 41.

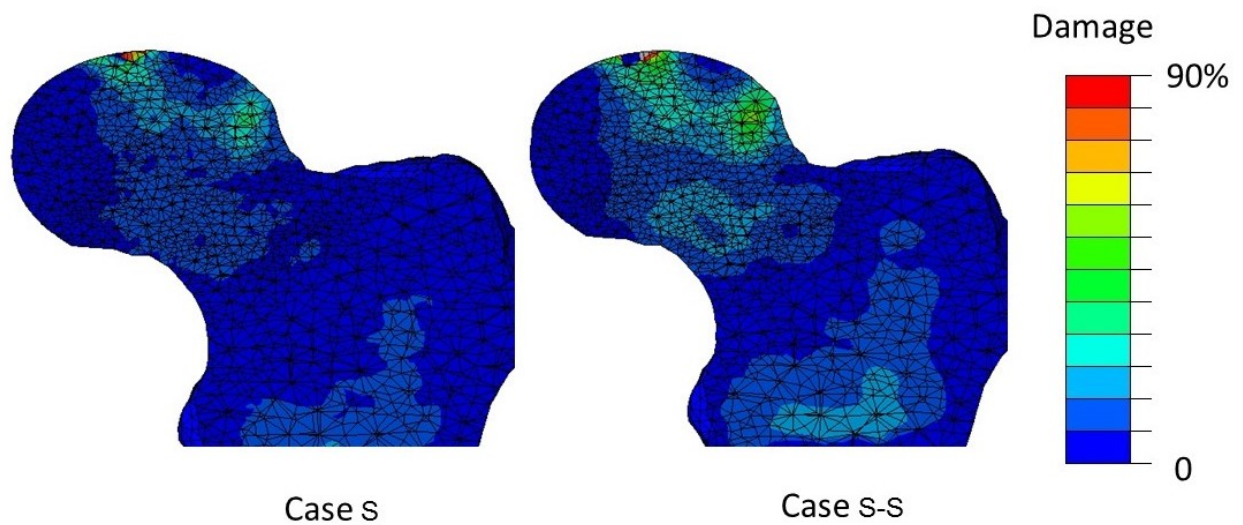


Figure 40 Pattern of damage distribution from load Case S (left) compared to Case S-S (right) for Specimen 6. In Case S, damage occurred primarily in the proximal subcapital region. In Case S-S, however, load was carried more evenly by the structure, with moderate to high damage at the inferior subcapital region as well.

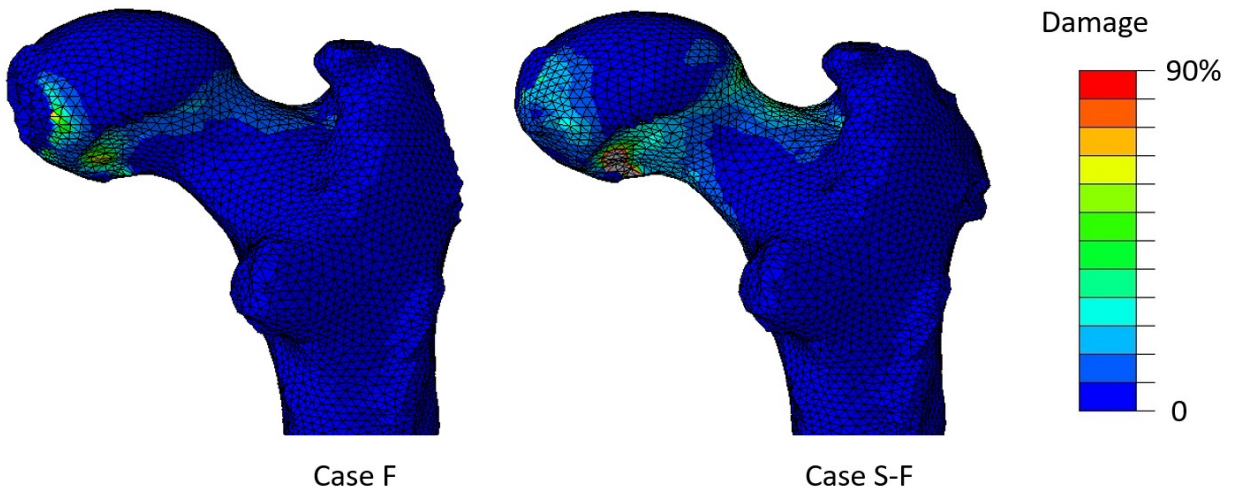


Figure 41 Pattern of damage distribution from load Case F (left) compared to Case S-F (right) for Specimen 5. In Case F, damage occurred primarily in the inferior subcapital region. In Case S-F, however, load was carried more evenly by the structure, with moderate damage throughout the superior aspect of the femoral neck as well.

For specimen 6, the mechanism behind this phenomenon becomes apparent when comparing damage patterns from Case S-S after only the first of the two stumbling events (Figure 42). In most specimens, this first event caused moderate damage (up to 60%), distributed over a large area of the cross section. The only exception was specimen 6, where the damage is highly localized. This caused a localized change in apparent stiffness (Equation 10), and this locally reduced stiffness may have caused alternate load paths to be favored when the specimen

was loaded again in the same direction (Figure 40).

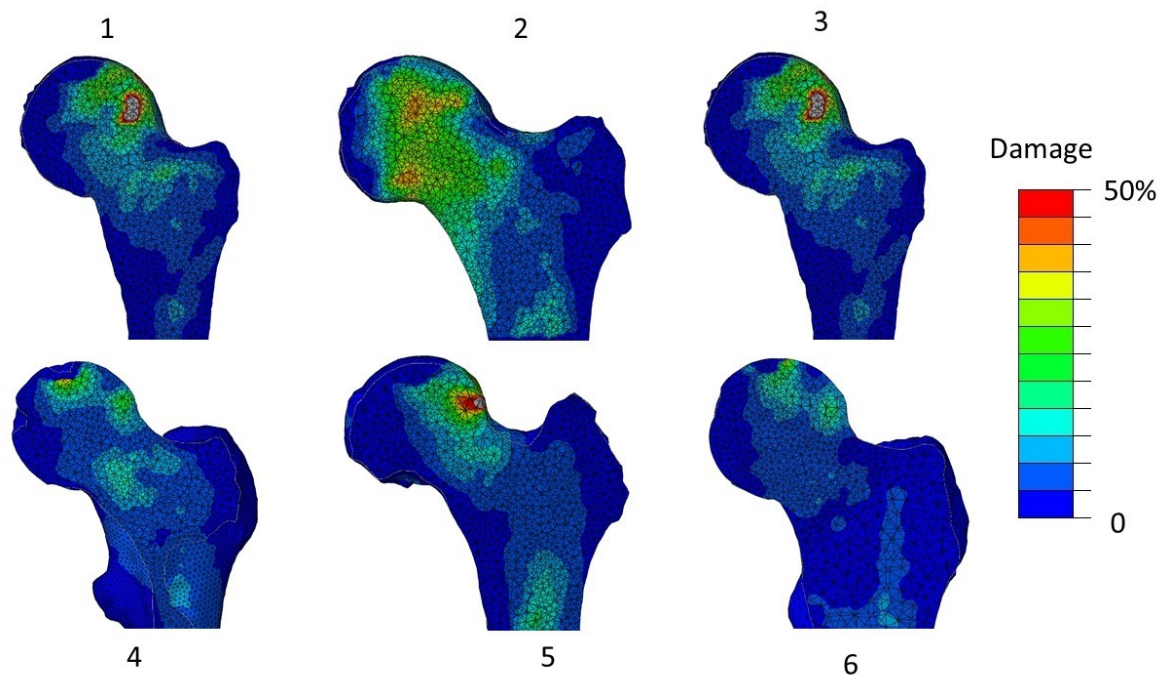


Figure 42 Patterns of damage accumulation after the first stumbling event of Case S-S. In specimens 1-5, relatively large areas of bone experience moderate damage (up to 60%). In case 6, however, damage is limited to the superior subcapital region.

Finally, specimen 1 was the only specimen to experience a loss of strength due to previous damage accumulation. However, it is unclear why this specimen alone experienced strength reductions from damage accumulation. The specimen was not notably weak nor strong, with a stumbling-direction fracture load of 7.8 kN compared to a study average of 7.4 kN. Femoral neck density was also unremarkable; the specimen had a femoral neck T-score of -2.5, which was similar to specimens 2 and 6 (T-scores of -2.6, and -2.5, respectively), and somewhat higher than specimen 4 (T-score of -3.0).

## 6.4. Discussion

### 6.3.3. Stumbling Loads and the Effects of Worsening Osteoporosis

The purpose of this phase of the study was to determine whether physiological loading can cause femoral fracture. In particular, this study evaluated the risk of fracture due to stumbling, as this event had the highest loads measured *in-vivo* [30]. Fracture risks were estimated using specimen specific FE models, which had been developed and validated in Chapter 5. Comparing fracture load predictions to population weight distributions, it was found that four of six specimens had a moderate risk of fracture (37-55%). However, the risk increased dramatically with simulated worsening osteoporosis. When bone density was degraded to a T-score of -3.5 (severe osteoporosis), five of the six specimens were almost certain to fail (risk >95%).

The findings are consistent with previous studies. Vinceoncti et al. [31] had reported that physiological loading could cause fracture, but only for severely osteoporotic patients (T-score <-4.5). However, their study was limited to walking loads, which are very low magnitude loading events [29]. Stumbling causes much larger hip contact forces, while still being clinically relevant. Thus, it is not surprising that this study found a large risk of fracture (>95%) at much lower osteoporosis severity (T-score -3.5). To the best of the author's knowledge, no other studies have demonstrated the plausibility of clinical relevant spontaneous fractures.

Somewhat surprisingly, this study did not find a strong discernable relationship between vBMD estimated T-score and FE predicted fracture load. However, this appears consistent with previous findings which report that 44% of hip fractures occur in patients who would not be classified as high risk [12]. Some previous studies have found moderate correlations ( $r^2 < 0.67$ ) between aBMD and fracture load in stance configuration [13], [159], but these relationships were found when looking at a large number of specimens (51-72) across a wide range of bone

densities. This study only had access to six specimens, all of which were osteoporotic or osteopenic.

While the results are realistic, this study has a few important limitations. FE models were made from a very small number of cadaveric specimens, and patient body weights were not available. As physiological loading is a function of patient body weight [29], [30], this makes it difficult to say with certainty whether a given specimen will fail. Instead, this study evaluated fracture as a risk based on the FE computed failure load compared to age and gender matched anthropomorphic data [155].

Another consequence of the small sample size is that the highest risk individuals in the population may not be represented in the data set. Previous studies have measured fracture loads as low as 3 kN [93], [160] while the weakest femur in this study was 5.3 kN. To overcome this challenge, this study attempted to simulate worsening osteoporosis. However, there is no widely accepted method for doing so. In their previous study, Viceconti et al. [31] used a small sample set of 24 femurs to develop an empirical relationship between whole bone density and T-score, then adjusted the density of their models by a constant factor to achieve a desired T-score. In this study, cortical and trabecular bone densities were degraded at different rates [158], based on previous measurements of bone loss. This may produce a more realistic distribution of bone density, but this has not been validated.

#### **6.3.4. Effects of Previous Damage Accumulation on Fracture Load and Pattern**

The second objective of this phase was to assess the effects of previously accumulated damage on fracture risk, from both stumbling and fall events. This was done by simulating an event to 80% of the fracture load, followed by a second event to complete fracture; fracture loads

from each binary event case were compared to fracture load of a specimen loaded to failure from a single event. Surprisingly, most of the specimens were found to be very resilient to the presence of previously accumulated damage. Three of six specimens showed no difference (<5%) in fracture load from any binary event load case compared to a single event load case, while two of the remaining specimens experienced an increase in strength (20-30%) in one of the three binary event load cases. Only one specimen was found to be susceptible to previous damage, with moderate strength reductions (5-15%) for all three of the binary event load cases.

Bone is a highly optimized structure, and damage tolerance may be a consequence of that optimization. In most specimens, the load was carried evenly by a large volume of the structure. In both load directions, forces up to 80% of the fracture load caused only low to moderate damage (<30%) to structurally critical elements, i.e., cortical bone and high density trabecular bone in the head-neck region. Only a small number of trabecular bone elements exceeded 40% damage (peak stress); however the comparisons to CT scans (Figure 36) showed that these initial damage sites occur in low density trabecular bone. It is likely that these low density sites do not contribute significantly to structural strength, even in their undamaged states. Thus, damage accumulation in these localized regions did not influence fracture load for the organ as a whole.

An exception to this pattern occurred in Specimen 1, for load cases S-S and S-F. In these cases the initial stumbling event resulted in high damage (>90%) to a small number of cortical bone elements in the superior subcapital region. As cortical bone is an important contributor to overall femoral strength [161], this resulted in 5-15% reduction in fracture load from subsequent loading, for cases S-S and S-F, respectively.

The largest reduction in fracture load was observed for Specimen 1, load case F-F, which suffered a 15% reduction in fracture load compared to case F. Unlike cases S-S and S-F, the mechanism for this is not readily apparent. The pattern of damage accumulation in case F-F is very similar to case F, but the simulation failed to converge at a lower applied load and less overall damage accumulation (Appendix C, Figure C-1). It is hypothesized that this may be the result of crack instability. In fall configuration, damage progresses most prominently in the inferior subcapital region, i.e., the region under tensile loading. Previous experimental studies by de Bakker et al. [21], which included high speed video footage, have demonstrated that this loading configuration is susceptible to periods of unstable crack growth, characterized by near instantaneous decreases in reaction force and rapid extension of the crack discontinuity. Damage evolution dissipates energy, promoting crack stability [162]. However, a pre-damaged element is able to absorb less energy than an undamaged one [77], [78]. Thus, it is plausible that specimen 1 experienced crack instability at a lower load, and lower crack size, during case F-F compared to case F.

To the best of the author's knowledge, this is the first study to look at the effects of damage accumulation on femoral fracture load and fracture pattern, making it difficult to compare these results to previous findings. However, it should be noted that the FE model used for this study was validated for stumbling configuration loading in Chapter 4. Unfortunately, due to a very limited number of available specimens, the model could not be validated in fall configuration as well. However the fracture patterns predicted by the model, i.e., failure in the inferior subcapital region often accompanied by damage or failure in the superior femoral neck, were consistent with previous experimental findings [21]. The fall configuration fracture loads predicted by this study (2.1-7 kN) were also consistent with previous findings [21], [40], [91], [140].

An important limitation of this study is that viscoelastic effects were ignored, even in fall configuration. The results of Chapter 3 demonstrated that these effects can have a non-negligible effect (3-15%) on predicted fracture load. However, the spatial distribution of strain, and thus damage, was largely unaffected. The purpose of this research was to compare different loading cases, and note relative changes in damage patterns and fracture loads changed. This small additional error in the absolute value of fracture load is unlikely to have a large detrimental effect on these comparisons.

## Chapter 7: Summary

This thesis examined the effects of damage accumulation and physiological loading on femoral fracture risk, using patient-specific FE models. An important component of this research focused on common simplifying assumptions, in order to ensure that the *in-vitro* studies matched the *in-vivo* condition as closely as possible. Factors which could plausibly affect the simulation of fall and physiological loads, but were not adequately explored in the current literature, were selected for further investigation. The remainder of this chapter will summarize the findings of this research, with particular emphasis on how these results expand the existing body of knowledge and represent significant contributions to the field. The study was divided into four major research tasks, detailed in the previous chapters:

- CHAPTER 3: A preliminary investigation of factors related to simulation of femoral fracture in fall configuration. The influence of BC selection and multiphysics effects were investigated in detail.
- CHAPTER 4: A preliminary investigation of factors related to the accurate simulation of femoral fracture in physiological (stumbling) configuration. The influence of muscle forces, and the importance of accurate specimen alignment, were investigated in detail.
- CHAPTER 5: Development and experimental validation of a gradient-enhanced, quasi-brittle FE model for the accurate prediction of fracture load and fracture pattern. Accuracy of these models were compared to previous work reported in the literature.
- CHAPTER 6: Investigation of the effects of physiological loading on femoral fracture risk. It was hypothesized that a femur could plausibly fail during high magnitude physiological events (stumbling). It was also hypothesized that previous damage accumulation from high

magnitude events (stumbling or fall), may leave the bone unfractured but susceptible to subsequent loading.

Chapter 3 was investigated using a patient-specific finite element model of the proximal femur. This phase of the study investigated the relative influence of different BCs, viscoelasticity, inertial dynamics, and biphasic (pore fluid) effects on simulation of femoral fracture load. All of these factors had the potential to influence FE predictions of fracture load, but were commonly neglected in previous FE investigations [19], [93], [94], [140]. To the best of the author's knowledge, however, the influence of these simplifying assumptions had never been well-quantified, before this study.

It was found that use of different plausible fall BCs could affect fracture load predictions by approximately 20%, however, fracture pattern was largely unaffected. Effects of viscoelasticity were also significant, causing predicted femoral strength to increase by 3% and 15%, when using uniform viscoelastic properties of cortical and trabecular bone, respectively. As real femurs are a combination of these two bone types, the true effect is expected to lie somewhere in between these two extremes. It was noted, however, that these changes in fracture strength occurred without significant changes to pattern of strain distribution. This phase of the study also looked at the influence of inertial dynamics and biphasic behavior. In both cases, however, effects were negligible under realistic load conditions (<3% difference compared to an equivalent quasi-static model).

Overall, the results of this task helped to justify modelling choices and simplifying assumptions made at later stages of this research. These findings were also considered novel in their own right, and have been successfully published in the journal of biomechanics [163].

Chapter 4 investigated issues related to accurate *in-vitro* modelling of femora in physiological load configurations. The first phase of this task investigated the potential influence of muscle loads on the simulation of femoral fracture during stumbling. This supplements previously work, which investigated the effects of a limited number of muscles under walking loads [48]. Stumbling is a more extreme event, compared to walking, and it was hypothesized to have higher muscle forces, resulting in a greater effect on FE simulation results. However, this study revealed that inclusion of these muscle forces had limited effect on fracture load (<3% difference) or fracture pattern during stumbling. As a result, these effects were neglected from future phases of this research.

This task also investigated the effect of accurate femoral alignment for *in-vitro* fracture testing. *In-vitro* experimental testing is a powerful tool, and is commonly used as a means to validate proposed FE models [15], [18], [80]. However, the accuracy of different alignment techniques, and their effect on fracture load predictions, had not been well explored in previous literature. For the first time, this study found that fracture load predictions could be extremely sensitive to small errors in load direction; errors in alignment targets of  $\pm 5^\circ$  could result in differences of up to 47% compared to a specimen aligned without error. Alignment by visual approximation was also found to be inadequate, highlighting the need for an accurate, repeatable, method of aligning femora during testing. In response to these findings, a novel method for specimen alignment was developed. An optical motion capture system was used to track the position of femoral landmarks in real time, which allowed the operator to achieve alignment targets with high repeatability.

This alignment technique was adopted for the next phase of this research, described in Chapter 5, which developed and experimentally validated a nonlinear FE model for the

prediction of femoral fracture. This work was based on recent publications by Hambli et al [80]–[82], who reported that bone fracture could be accurately simulated using a quasi-brittle continuum damage model. This previous work, however, had some important limitations. Their model had issues with spurious mesh sensitivity, and accurate fracture load predictions were by fitting model parameters based on experimental results [80]. The model developed as part of this research was able to effectively reduce the influence of spurious mesh sensitivity (Appendix A). This model also accurately predicted fracture load (9.6% error relative to experimental results) and fracture pattern using material properties obtained *a-priori*, with no fitting or parameter adjustments made after the validation experiments. Finally, qCT scans before and after failure were used to confirm FE model prediction trabecular damage.

The final phase of this research, described in Chapter 6, used this validated model to assess the risk of clinical fracture due to physiological loading events. As with previous chapters, this phase focused on stumbling events; these events were responsible for the highest hip contact forces measured *in-vivo*, but had not been adequately explored in the literature as a potential cause for spontaneous fracture.

This was done using the six FE models validated in Chapter 5. Unfortunately, patient body weights were not available, making it difficult to predict the magnitude of load acting on each specimen. Instead, FE predicted fracture loads were compared to age and gender matched distributions of population weight, from which a fracture risk was computed. Four of six specimens were found to have a moderate risk of fracture (37-55%), and this risk increased significantly with simulated worsening osteoporosis. When bone density was degraded to a t-score of -3.5, five of six specimens were nearly certain to fail (risk >95%).

It was also hypothesized that high load events, such as stumbling or falls, could damage bone without causing immediate femoral fracture; this accumulation of previous damage could leave the femur susceptible to fracture from subsequent loading. However, the effects of damage accumulation had never been explored at the organ level. The final phase of this research investigated repeat loadings, i.e., different combination of fall and stumble, and their effects of fracture pattern and load.

Most tested specimens were surprisingly resilient to the effects of accumulated damage, showing little (<5%) change in fracture load from the binary event load case, compared to the single event load case. Only one specimen experienced reductions in strength (5-15%) reductions in strength from all three binary load cases. Most surprisingly, two load cases experienced moderate (20-30%) increase in fracture load due to the presence of previous damage accumulation. It was noted that previous damage accumulation caused the load to be more evenly shared upon subsequent loading (Figure 40 and Figure 41). This was a highly novel, and unexpected finding.

## **7.1. Summary of Contributions to the Field**

For the first time, viscoelasticity, local inertial dynamics, and biphasic effects were evaluated regarding to their relative influence on accurate simulation of femoral fracture load. In the past, these effects had been hypothesized to play a potentially important role, but were not well-quantified in the literature. This study showed that only viscoelasticity had a non-negligible effect, under realistic loading conditions. However, the effects were relatively moderate, with a <15% difference in fracture load compared to an equivalent quasi-static model and no change in strain distribution pattern. Including viscoelastic effects may add significant computational

complexity to FE models, and these findings may help future researchers determine whether the additional complexity is warranted for their particular application.

This was also the first study to investigate the effects of different BCs on simulation of femoral fracture in fall configuration; these findings may be useful in interpreting data in the literature, as previous studies often use very different BCs, as discussed in Section 2.1.2. Differences in BCs were found to have moderate effect on predicted fracture loads (22% difference between vases), but little change in strain distribution pattern.

This study demonstrated, for the first time, that small differences in femoral alignment can have a large effect on fracture load prediction during physiological activities (stumbling). This creates a challenge, particularly if *in-vitro* experiments must be compared to FE simulation. To solve this issue, a novel method for specimen alignment was developed. Using an optical motion tracking system, this method allowed cadaveric specimens to be quickly and accurately oriented.

As part of this study we develop a novel, gradient-enhanced quasi brittle finite element model for the prediction of femoral fracture load and pattern; the model itself represents an important contribution to the field of biomechanics. For the first time, fracture pattern and patterns of underlying trabecular damage were well predicted in all observed cases. Moreover, accurate prediction of fracture load (9.6% average difference between model and experiment) was obtained with material parameters selected *a-priori*.

The model was used to demonstrate, for the first time, that stumbling loads can be associated with a significant risk of fracture, particularly if the patient is very osteoporotic. The model was also used to study the effects of repeated loading on femoral fracture patterns and strain, a phenomenon that had not been explored in the past. It was expected that damage accumulation

would result in decreases to overall fracture strength, and this was observed in some cases. However, damage accumulation was also found to cause increases in strength in a number of load cases (Figure 39). This was a novel finding had not been hypothesized in previous literature.

## **7.2. Future work**

This study demonstrated that stumbling events have the potential to cause hip fractures, but these events are poorly explored from a biomechanical standpoint. Previous works have investigated biomechanical techniques for fall prevention and risk management [164], and a similar approach may be taken to better understand the mechanics of stumbling, and develop techniques to mitigate fracture risk. Such results could be used to develop more effective preventative intervention strategies for management of osteoporotic hip fracture.

This was also the first study to investigate the effects of previous damage accumulation on fracture risk from subsequent loading. While the study found that many different responses were possible, i.e., weakening, strengthening, or no effect, the prevalence of each response is unclear, given the relatively small sample size in this study. This may justify a larger follow-up study. Such a study would also be better suited to identifying relationships between bone morphology and damage tolerance.

Finally, the quasi brittle FE model developed as part of this research may be a powerful tool for future investigations exploring the causes and mechanisms of hip fracture. With additional validation experiments, the model may also be suitable for FE studies of injuries involving other bones as well. There has also been recent interest in high resolution models, to simulate bone at the microstructure level. This can provide important insight into the failure mechanisms of bone, but previously published models have been limited to linear elastic material properties [165],

[166]. Recent studies have demonstrated that bone tissue within the trabeculae can also be modelled as quasi-brittle continuum [167]. With minor modification, the custom finite element implemented for this study could be used with these high resolution models. While a nonlinear high resolution model of the whole femur is likely to be computationally prohibitive, submodelling techniques [168]–[170] may be employed to study the microstructural response at key locations.

## References

- [1] D. Hanley and R. Josse, "Prevention and management of osteoporosis: consensus statements from the Scientific Advisory Board of the Osteoporosis Society of Canada. 1. Introduction.," *C. Can. Med. Assoc. J.*, vol. 155, no. 7, pp. 1995–1997, 1996.
- [2] R. Mittal and S. Banerjee, "Proximal femoral fractures: Principles of management and review of literature," *J. Clin. Orthop. Trauma*, vol. 3, no. 1, pp. 15–23, Jun. 2012.
- [3] J. Compston, a Cooper, C. Cooper, R. Francis, J. a Kanis, D. Marsh, E. V McCloskey, D. M. Reid, P. Selby, and M. Wilkins, "Guidelines for the diagnosis and management of osteoporosis in postmenopausal women and men from the age of 50 years in the UK.," *Maturitas*, vol. 62, no. 2, pp. 105–8, Feb. 2009.
- [4] J. E. Tarride, R. B. Hopkins, W. D. Leslie, S. Morin, J. D. Adachi, A. Papaioannou, L. Bessette, J. P. Brown, and R. Goeree, "The burden of illness of osteoporosis in Canada.," *Osteoporos. Int.*, Mar. 2012.
- [5] R. Baron, S. Ferrari, and R. G. G. Russell, "Denosumab and bisphosphonates: different mechanisms of action and effects.," *Bone*, vol. 48, no. 4, pp. 677–92, Apr. 2011.
- [6] R. G. G. Russell, "Bisphosphonates: the first 40 years.," *Bone*, vol. 49, no. 1, pp. 2–19, Jul. 2011.
- [7] A. Daroszewska, "Prevention and treatment of osteoporosis in women: an update," *Obstet. Gynaecol. Reprod. Med.*, vol. 22, no. 6, pp. 162–169, Jun. 2012.
- [8] J. P. Bilezikian, "Efficacy of Bisphosphonates in Reducing Fracture Risk in Postmenopausal Osteoporosis," *Am. J. Med.*, vol. 122, no. 2 SUPPL., pp. S14–S21, 2009.

- [9] L. Y. Park-Wyllie, M. M. Mamdani, D. N. Juurlink, G. a Hawker, N. Gunraj, P. C. Austin, D. B. Whelan, P. J. Weiler, and A. Laupacis, “Bisphosphonate use and the risk of subtrochanteric or femoral shaft fractures in older women.,” *JAMA*, vol. 305, no. 8, pp. 783–9, Feb. 2011.
- [10] V. Bottai, S. Giannotti, G. Dell’osso, G. De Paola, a Menconi, F. Falossi, G. Raffaetà, and G. Guido, “Atypical femoral fractures: retrospective radiological study of 319 femoral fractures and presentation of clinical cases.,” *Osteoporos. Int.*, vol. 25, no. 3, pp. 993–7, Mar. 2014.
- [11] B. Lentle, A. M. Cheung, D. a Hanley, W. D. Leslie, D. Lyons, A. Papaioannou, S. Atkinson, J. P. Brown, S. Feldman, A. B. Hodsman, A. S. Jamal, R. G. Josse, S. M. Kaiser, B. Kvern, S. Morin, and K. Siminoski, “Osteoporosis Canada 2010 guidelines for the assessment of fracture risk.,” *Can. Assoc. Radiol. J.*, vol. 62, no. 4, pp. 243–50, Nov. 2011.
- [12] S. C. . Schuit, M. van der Klift, a. E. a. . Weel, C. E. D. . de Laet, H. Burger, E. Seeman, a Hofman, a. . Uitterlinden, J. P. T. . van Leeuwen, and H. a. . Pols, “Fracture incidence and association with bone mineral density in elderly men and women: the Rotterdam Study,” *Bone*, vol. 34, no. 1, pp. 195–202, Jan. 2004.
- [13] D. D. Cody, G. J. Gross, F. J. Hou, H. J. Spencer, S. A. Goldstein, and D. P. Fyhrie, “Femoral strength is better predicted by finite element models than QCT and DXA,” *J. Biomech.*, vol. 32, no. 10, pp. 1013–1020, Oct. 1999.
- [14] K. K. Nishiyama, M. Ito, a Harada, and S. K. Boyd, “Classification of women with and without hip fracture based on quantitative computed tomography and finite element

- analysis.,” *Osteoporos. Int.*, vol. 25, no. 2, pp. 619–26, Feb. 2014.
- [15] J. H. Keyak, S. a Rossi, K. a Jones, and H. B. Skinner, “Prediction of femoral fracture load using automated finite element modeling.,” *J. Biomech.*, vol. 31, no. 2, pp. 125–33, Feb. 1998.
- [16] S. van den Munckhof and A. A. Zadpoor, “How accurately can we predict the fracture load of the proximal femur using finite element models?,” *Clin. Biomech. (Bristol, Avon)*, vol. 29, no. 4, pp. 373–80, Apr. 2014.
- [17] J. H. Keyak, “Improved prediction of proximal femoral fracture load using nonlinear finite element models.,” *Med. Eng. Phys.*, vol. 23, no. 3, pp. 165–73, Apr. 2001.
- [18] M. Bessho, I. Ohnishi, J. Matsuyama, T. Matsumoto, K. Imai, and K. Nakamura, “Prediction of strength and strain of the proximal femur by a CT-based finite element method.,” *J. Biomech.*, vol. 40, no. 8, pp. 1745–53, Jan. 2007.
- [19] H. Ridha and P. J. Thurner, “Finite element prediction with experimental validation of damage distribution in single trabeculae during three-point bending tests,” *J. Mech. Behav. Biomed. Mater.*, pp. 1–13, Jul. 2013.
- [20] S. L. Greenspan, E. R. Myers, L. a Maitland, N. M. Resnick, and W. C. Hayes, “Fall severity and bone mineral density as risk factors for hip fracture in ambulatory elderly.,” *JAMA*, vol. 271, no. 2, pp. 128–33, Jan. 1994.
- [21] P. M. de Bakker, S. L. Manske, V. Ebacher, T. R. Oxland, P. a Cripton, and P. Guy, “During sideways falls proximal femur fractures initiate in the superolateral cortex: evidence from high-speed video of simulated fractures.,” *J. Biomech.*, vol. 42, no. 12, pp.

1917–25, Aug. 2009.

- [22] A. Schwartz, J. Kelsey, and S. Sidney, “Characteristics of falls and risk of hip fracture in elderly men,” *Osteoporos. Int.*, vol. 8, no. 3, pp. 240–246, 1998.
- [23] a C. Courtney, E. F. Wachtel, E. R. Myers, and W. C. Hayes, “Age-related reductions in the strength of the femur tested in a fall-loading configuration.,” *J. Bone Joint Surg. Am.*, vol. 77, no. 3, pp. 387–95, Mar. 1995.
- [24] S. N. Robinovitch, T. a McMahan, and W. C. Hayes, “Force attenuation in trochanteric soft tissues during impact from a fall.,” *J. Orthop. Res.*, vol. 13, no. 6, pp. 956–62, Nov. 1995.
- [25] W. C. Hayes, E. R. Myers, S. N. Robinovitch, a Van Den Kroonenberg, a C. Courtney, and T. a McMahan, “Etiology and prevention of age-related hip fractures.,” *Bone*, vol. 18, no. 1 Suppl, p. 77S–86S, Jan. 1996.
- [26] T. O. Smith, E. Higson, M. Pearson, and M. Mansfield, “Is there an increased risk of falls and fractures in people with early diagnosed hip and knee osteoarthritis? Data from the Osteoarthritis Initiative,” *Int. J. Rheum. Dis.*, pp. 1–9, 2016.
- [27] J. Grisso, J. Kelsey, and B. Strom, “Risk factors for falls as a cause of hip fracture in women,” *N. Engl. J. Med.*, pp. 1326–1331, 1991.
- [28] M. Horii, H. Fujiwara, T. Ikeda, K. Ueshima, K. Ikoma, T. Shirai, M. Nagae, Y. Oka, K. Sawada, N. Kuriyama, and T. Kubo, “Differences in monthly variation , cause , and place of injury between femoral neck and trochanteric fractures : 6-year survey ( 2008-2013 ) in Kyoto prefecture , Japan,” pp. 19–24, 2016.

- [29] G. Bergmann, G. Deuretzbacher, M. Heller, F. Graichen, A. Rohlmann, J. Strauss, and G. N. Duda, "Hip contact forces and gait patterns from routine activities.," *J. Biomech.*, vol. 34, no. 7, pp. 859–71, Jul. 2001.
- [30] G. Bergmann, F. Graichen, and A. Rohlmann, "Hip joint contact forces during stumbling.," *Langenbecks. Arch. Surg.*, vol. 389, no. 1, pp. 53–9, Feb. 2004.
- [31] M. Viceconti, F. Taddei, L. Cristofolini, S. Martelli, C. Falcinelli, and E. Schileo, "Are spontaneous fractures possible? An example of clinical application for personalised, multiscale neuro-musculo-skeletal modelling.," *J. Biomech.*, vol. 45, no. 3, pp. 421–6, Feb. 2012.
- [32] U. Wolfram, H.-J. Wilke, and P. K. Zysset, "Damage accumulation in vertebral trabecular bone depends on loading mode and direction.," *J. Biomech.*, vol. 44, no. 6, pp. 1164–9, Apr. 2011.
- [33] Q. Luo, H. Leng, R. Acuna, X. N. Dong, Q. Rong, and X. Wang, "Constitutive relationship of tissue behavior with damage accumulation of human cortical bone.," *J. Biomech.*, vol. 43, no. 12, pp. 2356–61, Aug. 2010.
- [34] E. I. Waldorff, K. B. Christenson, L. A. Cooney, and S. A. Goldstein, "Microdamage repair and remodeling requires mechanical loading.," *J. bone Miner. Res.*, vol. 25, no. 4, pp. 734–45, Apr. 2010.
- [35] H. Gray, *Anatomy of the Human Body*, vol. 157, no. 5. Lea & Febiger, 1918.
- [36] N. Palastanga, *Anatomy and Human Movement: Structure and Function*, 6th ed. Edinburgh: Churchill Livingstone Elsevier, 2012.

- [37] C. Ethier and C. Simmons, *Introductory biomechanics: from cells to organisms*. Cambridge; New York: Cambridge University Press, 2007.
- [38] T. P. Pinilla, K. C. Boardman, M. L. Bouxsein, E. R. Myers, and W. C. Hayes, "Impact direction from a fall influences the failure load of the proximal femur as much as age-related bone loss.," *Calcif. Tissue Int.*, vol. 58, no. 4, pp. 231–5, Apr. 1996.
- [39] J. Parkkari, P. Kannus, M. Palvanen, and A. Natri, "Majority of hip fractures occur as a result of a fall and impact on the greater trochanter of the femur: a prospective controlled hip fracture study with 206 consecutive patients," *Calcif. Tissue Int.*, vol. 65, no. 3, pp. 183–187, 1999.
- [40] A. C. Courtney, E. F. Wachtel, E. R. Myers, and W. C. Hayes, "Effects of loading rate on strength of the proximal femur.," *Calcif. Tissue Int.*, vol. 55, no. 1, pp. 53–8, Jul. 1994.
- [41] B. J. Hayes and M. E. Goddard, "Hip impact velocities and body configurations for voluntary falls from standing height," *J. Anim. Sci.*, vol. 86, no. 9, pp. 2089–92, Sep. 2008.
- [42] S. Majumder, A. Roychowdhury, and S. Pal, "Simulation of hip fracture in sideways fall using a 3D finite element model of pelvis-femur-soft tissue complex with simplified representation of whole body.," *Med. Eng. Phys.*, vol. 29, no. 10, pp. 1167–78, Dec. 2007.
- [43] S. Majumder, A. Roychowdhury, and S. Pal, "Effects of trochanteric soft tissue thickness and hip impact velocity on hip fracture in sideways fall through 3D finite element simulations.," *J. Biomech.*, vol. 41, no. 13, pp. 2834–42, Sep. 2008.
- [44] F. Feldman and S. N. Robinovitch, "Reducing hip fracture risk during sideways falls:

- evidence in young adults of the protective effects of impact to the hands and stepping.,” *J. Biomech.*, vol. 40, no. 12, pp. 2612–8, Jan. 2007.
- [45] J. H. Keyak, S. a Rossi, K. a Jones, C. M. Les, and H. B. Skinner, “Prediction of fracture location in the proximal femur using finite element models.,” *Med. Eng. Phys.*, vol. 23, no. 9, pp. 657–64, Nov. 2001.
- [46] B. J. Roberts, E. Thrall, J. a Muller, and M. L. Bouxsein, “Comparison of hip fracture risk prediction by femoral aBMD to experimentally measured factor of risk.,” *Bone*, vol. 46, no. 3, pp. 742–6, Mar. 2010.
- [47] M. O. Heller, G. Bergmann, G. Deuretzbacher, L. Dürselen, M. Pohl, L. Claes, N. P. Haas, and G. N. Duda, “Musculo-skeletal loading conditions at the hip during walking and stair climbing.,” *J. Biomech.*, vol. 34, no. 7, pp. 883–93, Jul. 2001.
- [48] L. Cristofolini, M. Juszczuk, S. Martelli, F. Taddei, and M. Viceconti, “In vitro replication of spontaneous fractures of the proximal human femur.,” *J. Biomech.*, vol. 40, no. 13, pp. 2837–45, Jan. 2007.
- [49] F. Taddei, L. Cristofolini, S. Martelli, H. S. Gill, and M. Viceconti, “Subject-specific finite element models of long bones: An in vitro evaluation of the overall accuracy,” *J. Biomech.*, vol. 39, no. 13, pp. 2457–2467, 2006.
- [50] Julius Wolff Institute, “Orthoload Wiki: Hip Joint.” [Online]. Available: [http://www.wiki.orthoload.com/index.php?title=Hip\\_joint](http://www.wiki.orthoload.com/index.php?title=Hip_joint). [Accessed: 11-May-2016].
- [51] F. E. Zajac, R. R. Neptune, and S. a Kautz, “Biomechanics and muscle coordination of human walking. Part I: introduction to concepts, power transfer, dynamics and

- simulations.,” *Gait Posture*, vol. 16, no. 3, pp. 215–32, Dec. 2002.
- [52] A. Erdemir, S. McLean, W. Herzog, and A. J. van den Bogert, “Model-based estimation of muscle forces exerted during movements.,” *Clin. Biomech. (Bristol, Avon)*, vol. 22, no. 2, pp. 131–54, Feb. 2007.
- [53] D. A. Winter, *Biomechanics and motor control of human movement*. John Wiley & Sons, 2009.
- [54] R. a Brand, D. R. Pedersen, and J. a Friederich, “The sensitivity of muscle force predictions to changes in physiologic cross-sectional area.,” *J. Biomech.*, vol. 19, no. 8, pp. 589–96, Jan. 1986.
- [55] R. D. Crowninshield and R. a Brand, “A physiologically based criterion of muscle force prediction in locomotion.,” *J. Biomech.*, vol. 14, no. 11, pp. 793–801, Jan. 1981.
- [56] R. a Brand, D. R. Pedersen, D. T. Davy, G. M. Kotzar, K. G. Heiple, and V. M. Goldberg, “Comparison of hip force calculations and measurements in the same patient.,” *J. Arthroplasty*, vol. 9, no. 1, pp. 45–51, Feb. 1994.
- [57] J. a Szivek, J. B. Benjamin, and P. L. Anderson, “An experimental method for the application of lateral muscle loading and its effect on femoral strain distributions.,” *Med. Eng. Phys.*, vol. 22, no. 2, pp. 109–16, Mar. 2000.
- [58] J. P. Paul, “Influence of head constraint and muscle forces on the strain distribution within the intact femur.,” *Med. Eng. Phys.*, vol. 24, no. 3, p. 243, Apr. 2002.
- [59] L. Cristofolini, M. Viceconti, A. Toni, and A. Giunti, “Influence of thigh muscles on the axial strains in a proximal femur during early stance in gait,” *J. Biomech.*, vol. 28, no. 5,

1995.

- [60] G. N. Duda, M. Heller, J. Albinger, O. Schulz, E. Schneider, and L. Claes, “Influence of muscle forces on femoral strain distribution.,” *J. Biomech.*, vol. 31, no. 9, pp. 841–6, Sep. 1998.
- [61] A. D. Speirs, M. O. Heller, G. N. Duda, and W. R. Taylor, “Physiologically based boundary conditions in finite element modelling.,” *J. Biomech.*, vol. 40, no. 10, pp. 2318–23, Jan. 2007.
- [62] S. Cowin, *Bone mechanics handbook*, 2nd Editio. Boca Raton, London, New York, Washington D.C: CRC Press, 2001.
- [63] U. A. Gurkan and O. Akkus, “The Mechanical Environment of Bone Marrow: A Review,” *Ann. Biomed. Eng.*, vol. 36, no. 12, pp. 1978–1991, Oct. 2008.
- [64] T. M. Keaveny, E. F. Morgan, G. L. Niebur, and O. C. Yeh, “Biomechanics of trabecular bone.,” *Annu. Rev. Biomed. Eng.*, vol. 3, pp. 307–33, Jan. 2001.
- [65] B. Helgason, E. Perilli, E. Schileo, F. Taddei, S. Brynjólfsson, and M. Viceconti, “Mathematical relationships between bone density and mechanical properties: a literature review.,” *Clin. Biomech. (Bristol, Avon)*, vol. 23, no. 2, pp. 135–46, Feb. 2008.
- [66] E. F. Morgan, H. H. Bayraktar, and T. M. Keaveny, “Trabecular bone modulus–density relationships depend on anatomic site,” *J. Biomech.*, vol. 36, no. 7, pp. 897–904, Jul. 2003.
- [67] E. Schileo, F. Taddei, A. Malandrino, L. Cristofolini, and M. Viceconti, “Subject-specific finite element models can accurately predict strain levels in long bones.,” *J. Biomech.*, vol.

- 40, no. 13, pp. 2982–9, Jan. 2007.
- [68] T. Iyo, Y. Maki, N. Sasaki, and M. Nakata, “Anisotropic viscoelastic properties of cortical bone.,” *J. Biomech.*, vol. 37, no. 9, pp. 1433–7, Sep. 2004.
- [69] R. M. Guedes, J. a Simões, and J. L. Morais, “Viscoelastic behaviour and failure of bovine cancellous bone under constant strain rate.,” *J. Biomech.*, vol. 39, no. 1, pp. 49–60, Jan. 2006.
- [70] J. D. Currey, “Tensile yield in compact bone is determined by strain, post-yield behaviour by mineral content.,” *J. Biomech.*, vol. 37, no. 4, pp. 549–56, Apr. 2004.
- [71] D. L. Kopperdahl and T. M. Keaveny, “Yield strain behavior of trabecular bone.,” *J. Biomech.*, vol. 31, no. 7, pp. 601–8, Jul. 1998.
- [72] H. H. Bayraktar, A. Gupta, R. Y. Kwon, and T. M. Keaveny, “The modified super-ellipsoid criterion for human trabecular bone.,” *J. Biomech. Eng.*, vol. 126, no. 6, pp. 677–84, 2004.
- [73] E. Schileo, F. Taddei, L. Cristofolini, and M. Viceconti, “Subject-specific finite element models implementing a maximum principal strain criterion are able to estimate failure risk and fracture location on human femurs tested in vitro.,” *J. Biomech.*, vol. 41, no. 2, pp. 356–67, Jan. 2008.
- [74] P. Zioupos, U. Hansen, and J. D. Currey, “Microcracking damage and the fracture process in relation to strain rate in human cortical bone tensile failure.,” *J. Biomech.*, vol. 41, no. 14, pp. 2932–9, Oct. 2008.
- [75] Z. Seref-Ferlengez, O. D. Kennedy, and M. B. Schaffler, “Bone microdamage, remodeling

- and bone fragility: how much damage is too much damage?," *Bonekey Rep.*, vol. 4, no. September 2014, p. 644, 2015.
- [76] D. R. Carter, G. H. Schwab, and D. M. Spengler, "Tensile Fracture of Cancellous Bone," *Acta Orthop Scand*, vol. 51, no. 5, pp. 733–741, 1980.
- [77] G. Z. Voyiadjis and P. I. Kattan, *Damage mechanics*. Boca Raton: Taylor & Francis, 2005.
- [78] J. Lemaitre and R. Desmorat, *Engineering damage mechanics: ductile, creep, fatigue and brittle failures*. Springer, 2005.
- [79] R. H. J. Peerlings, W. A. M. Brekelmans, and J. H. . de Vree, "Gradient enhanced damage for quasi-brittle materials," *Int. J. Numer. ...*, vol. 39, pp. 3391–3403, 1996.
- [80] R. Hambli and S. Allaoui, "A Robust 3D Finite Element Simulation of Human Proximal Femur Progressive Fracture Under Stance Load with Experimental Validation.," *Ann. Biomed. Eng.*, no. Cdm, Jul. 2013.
- [81] R. Hambli, "A quasi-brittle continuum damage finite element model of the human proximal femur based on element deletion.," *Med. Biol. Eng. Comput.*, vol. 51, no. 1–2, pp. 219–31, Feb. 2013.
- [82] R. Hambli, A. Bettamer, and S. Allaoui, "Finite element prediction of proximal femur fracture pattern based on orthotropic behaviour law coupled to quasi-brittle damage," *Med. Eng. Phys.*, vol. 34, no. 2, pp. 202–210, 2012.
- [83] S. Grampp and J. Adams, *Radiology of osteoporosis*, vol. 2nd rev. e. Berlin: Springer, 2008.

- [84] J. a Kanis, "Diagnosis of osteoporosis and assessment of fracture risk.," *Lancet*, vol. 359, no. 9321, pp. 1929–36, Jun. 2002.
- [85] J. C. Lotz, E. J. Cheal, and W. C. Hayes, "Fracture prediction for the proximal femur using finite element models: Part II--Nonlinear analysis.," *J. Biomech. Eng.*, vol. 113, no. 4, pp. 361–5, Nov. 1991.
- [86] J. C. Lotz, E. J. Cheal, and W. C. Hayes, "Fracture prediction for the proximal femur using finite element models: Part I--Linear analysis.," *J. Biomech. Eng.*, vol. 113, no. 4, pp. 353–60, Nov. 1991.
- [87] N. Wakao, A. Harada, Y. Matsui, M. Takemura, H. Shimokata, M. Mizuno, M. Ito, Y. Matsuyama, and N. Ishiguro, "The effect of impact direction on the fracture load of osteoporotic proximal femurs.," *Med. Eng. Phys.*, vol. 31, no. 9, pp. 1134–9, Nov. 2009.
- [88] L. Grassi, E. Schileo, F. Taddei, L. Zani, M. Juszczuk, L. Cristofolini, and M. Viceconti, "Accuracy of finite element predictions in sideways load configurations for the proximal human femur.," *J. Biomech.*, vol. 45, no. 2, pp. 394–9, Jan. 2012.
- [89] M. Mirzaei, M. Keshavarzian, and V. Naeini, "Analysis of strength and failure pattern of human proximal femur using quantitative computed tomography (QCT)-based finite element method," *Bone*, pp. 1–7, Apr. 2014.
- [90] J. E. M. Koivumäki, J. Thevenot, P. Pulkkinen, V. Kuhn, T. M. Link, F. Eckstein, and T. Jämsä, "Ct-based finite element models can be used to estimate experimentally measured failure loads in the proximal femur," *Bone*, vol. 50, no. 4, pp. 824–829, 2012.
- [91] D. Dragomir-Daescu, J. Op Den Buijs, S. McEligot, Y. Dai, R. C. Entwistle, C. Salas, L.

- J. Melton, K. E. Bennet, S. Khosla, and S. Amin, "Robust QCT/FEA models of proximal femur stiffness and fracture load during a sideways fall on the hip.," *Ann. Biomed. Eng.*, vol. 39, no. 2, pp. 742–55, Feb. 2011.
- [92] M. Qasim, G. Farinella, J. Zhang, X. Li, L. Yang, R. Eastell, and M. Viceconti, "Patient-specific finite element estimated femur strength as a predictor of the risk of hip fracture: the effect of methodological determinants.," *Osteoporos. Int.*, 2016.
- [93] J. H. Keyak, S. Sigurdsson, G. S. Karlsdottir, D. Oskarsdottir, A. Sigmarsdottir, J. Kornak, T. B. Harris, G. Sigurdsson, B. Y. Jonsson, K. Siggeirsdottir, G. Eiriksdottir, V. Gudnason, and T. F. Lang, "Effect of finite element model loading condition on fracture risk assessment in men and women: The AGES-Reykjavik study.," *Bone*, vol. 57, no. 1, pp. 18–29, Jul. 2013.
- [94] C. Falcinelli, E. Schileo, L. Balistreri, F. Baruffaldi, B. Bordini, M. Viceconti, U. Albisinni, F. Ceccarelli, L. Milandri, A. Toni, and F. Taddei, "Multiple loading conditions analysis can improve the association between finite element bone strength estimates and proximal femur fractures: A preliminary study in elderly women," *Bone*, vol. 67, pp. 71–80, 2014.
- [95] K. H. Huebner, E. A. Thornton, and T. G. Byrom, *The finite element method for engineers*, vol. 3rd ed. New York: Wiley, 1995.
- [96] E. Schileo, L. Balistreri, L. Grassi, L. Cristofolini, and F. Taddei, "To what extent can linear finite element models of human femora predict failure under stance and fall loading configurations?," *J. Biomech.*, vol. 47, no. 14, pp. 3531–3538, 2014.

- [97] E. Tanck, J. B. van Aken, Y. M. van der Linden, H. W. B. Schreuder, M. Binkowski, H. Huizenga, and N. Verdonschot, "Pathological fracture prediction in patients with metastatic lesions can be improved with quantitative computed tomography based computer models," *Bone*, vol. 45, no. 4, pp. 777–783, 2009.
- [98] J. D. Bryant, "On the Mechanical Function of Marrow in Long Bones," *Eng. Med.*, vol. 17, no. 2, pp. 55–58, 1988.
- [99] M. A. K. Liebschner and T. S. Keller, "Hydraulic Strengthening Affects the Stiffness and Strength of Cortical Bone," *Ann. Biomed. Eng.*, vol. 33, no. 1, pp. 26–38, Jan. 2005.
- [100] J. D. Bryant, "Letter to the editor: On hydraulic strengthening of bones. Kafka, V. (1993)," *J. Biomech.*, vol. 28, no. 3, pp. 353–354, 1995.
- [101] D. R. Carter and W. C. Hayes, "The compressive behaviour of bone as a two-phase porous structure," *J. Bone Jt. Surg. Am.*, vol. 59, pp. 954–962, 1977.
- [102] J. A. Ochoa, T. W. Kiesler, J. P. Toombs, K. D. Brandt, B. M. Hillberry, D. A. Heck, and A. P. Sanders, "In Vivo Observations of Hydraulic Stiffening in the Canine Femoral Head," *J. Biomech. Eng.*, vol. 119, no. 1, pp. 103–108, Feb. 1997.
- [103] V. C. Mow, S. C. Kuei, W. M. Lai, and C. G. Armstrong, "Biphasic Creep and Stress Relaxation of Articular Cartilage in Compression: Theory and Experiments," *J. Biomech. Eng.*, vol. 102, no. 1, pp. 73–84, Feb. 1980.
- [104] K. A. Athanasiou and R. M. Natoli, *Introduction to Continuum Biomechanics*, vol. 3, no. 1. 2008.
- [105] J. Z. Wu, W. Herzog, and M. Epstein, "Evaluation of the finite element software

- ABAQUS for biomechanical modelling of biphasic tissues.,” *J. Biomech.*, vol. 31, no. 2, pp. 165–9, Feb. 1998.
- [106] J. L. Humar, *Dynamics of structures*. Exton PA: CRC Press, 2002.
- [107] H. Hilber and T. Hughes, “Collocation, dissipation and for time integration schemes in structural dynamics,” ... *Eng. Struct. Dyn.*, vol. 6, no. December 1976, pp. 99–117, 1978.
- [108] J. Sun, K. Lee, and H. Lee, “Comparison of implicit and explicit finite element methods for dynamic problems,” *J. Mater. Process. Technol.*, vol. 105, 2000.
- [109] W. A. M. Brekelmans and J. H. P. Vree, “Reduction of mesh sensitivity in continuum damage mechanics,” *Acta Mech.*, vol. 110, no. 1–4, pp. 49–56, Mar. 1995.
- [110] S. Murakami, *Continuum Damage Mechanics: A Continuum Mechanics Approach to the Analysis of Damage and Fracture*, vol. 185. Springer, 2012.
- [111] M. Charlebois, M. Jirásek, and P. K. Zysset, “A nonlocal constitutive model for trabecular bone softening in compression.,” *Biomech. Model. Mechanobiol.*, vol. 9, no. 5, pp. 597–611, Oct. 2010.
- [112] R. H. J. Peerlings, M. G. D. Geers, R. de Borst, and W. A. M. Brekelmans, “A critical comparison of nonlocal and gradient-enhanced softening continua,” *Int. J. Solids Struct.*, vol. 38, no. 44–45, pp. 7723–7746, Nov. 2001.
- [113] R. H. J. Peerlings, R. De Borst, W. A. M. Brekelmans, and M. G. D. Geers, “Gradient-enhanced damage modelling of concrete fracture,” *Mech. Cohes.-Frict. Matter.*, vol. 342, no. March 1997, pp. 323–342, 1998.

- [114] J. Yamashita, B. R. Furman, H. R. Rawls, X. Wang, and C. M. Agrawal, "The use of dynamic mechanical analysis to assess the viscoelastic properties of human cortical bone.," *J. Biomed. Mater. Res.*, vol. 58, no. 1, pp. 47–53, Jan. 2001.
- [115] R. Pelker and S. Saha, "Stress wave propagation in bone," *J. Biomech.*, 1983.
- [116] T. Krauthammer, "Dynamic Response and Analysis," in *Modern Protective Structures*, CRC Press, 2008, pp. 237–289.
- [117] J. Humar, "Response to general dynamic loading and transient response," in *Dynamics of Structures*, 2nd ed., CRC Press, 1990, pp. 317–354.
- [118] J. H. Keyak, "Prediction of femoral fracture load using finite element models: an examination of stress- and strain-based failure theories," *J. Biomech.*, vol. 33, no. 2, pp. 209–214, Feb. 2000.
- [119] T. Elgin, "Finite Element Analysis of Bone Remodelling Around an Uncemented Resurfaced Femoral Head," Carleton, 2010.
- [120] J. H. Keyak, I. Y. Lee, and H. B. Skinner, "Correlations between orthogonal mechanical properties and density of trabecular bone: Use of different densitometric measures," *J. Biomed. Mater. Res.*, vol. 28, no. 11, pp. 1329–1336, 1994.
- [121] S. C. Cowin, "Bone poroelasticity.," *J. Biomech.*, vol. 32, no. 3, pp. 217–38, Mar. 1999.
- [122] E. A. Nauman, K. E. Fong, and T. M. Keaveny, "Dependence of intertrabecular permeability on flow direction and anatomic site.," *Ann. Biomed. Eng.*, vol. 27, no. 4, pp. 517–24, 1999.

- [123] E. F. Morgan and T. M. Keaveny, “Dependence of yield strain of human trabecular bone on anatomic site.,” *J. Biomech.*, vol. 34, no. 5, pp. 569–77, May 2001.
- [124] W. J. Choi, P. A. Crompton, and S. N. Robinovitch, “Effects of hip abductor muscle forces and knee boundary conditions on femoral neck stresses during simulated falls,” *Osteoporos. Int.*, vol. 26, no. 1, pp. 291–301, 2014.
- [125] S. N. Robinovitch, W. C. Hayes, and T. a McMahon, “Prediction of femoral impact forces in falls on the hip.,” *J. Biomech. Eng.*, vol. 113, no. 4, pp. 366–374, 1991.
- [126] S. Pashah, M. Massenzio, and E. Jacquelin, “Prediction of structural response for low velocity impact,” *Int. J. Impact Eng.*, vol. 35, no. 2, pp. 119–132, Feb. 2008.
- [127] R. Olsson, “Mass criterion for wave controlled impact response of composite plates,” *Compos. Part A Appl. Sci. Manuf.*, vol. 31, no. 8, pp. 879–887, Aug. 2000.
- [128] T. B. Khalil, D. C. Viano, and L. A. Taber, “Vibrational Characteristics of the Embalmed Human Femur,” *J. Sound Vib.*, vol. 75, no. 3, pp. 417–436, 1981.
- [129] B. Couteau, M. C. Hobatho, R. Darmana, J. C. Brignola, and J. Y. Arlaud, “Finite element modelling of the vibrational behaviour of the human femur using CT-based individualized geometrical and material properties.,” *J. Biomech.*, vol. 31, no. 4, pp. 383–6, Apr. 1998.
- [130] U. Hansen, P. Zioupos, R. Simpson, J. D. Currey, and D. Hynd, “The effect of strain rate on the mechanical properties of human cortical bone.,” *J. Biomech. Eng.*, vol. 130, no. 1, p. 11011, Feb. 2008.
- [131] V. Kafka and J. Jírová, “A structural mathematical model for the viscoelastic anisotropic behaviour of trabecular bone.,” *Biorheology*, vol. 20, no. 6, pp. 795–805, 1983.

- [132] J. A. Ochoa, A. P. Sanders, D. A. Heck, and B. M. Hillberry, "Stiffening of the femoral head due to inter-trabecular fluid and intraosseous pressure.," *J. Biomech. Eng.*, vol. 113, no. 3, pp. 259–262, 1991.
- [133] C. B. Ruff and W. C. Hayes, "Cross-sectional geometry of Pecos Pueblo femora and tibiae - A biomechanical investigation: I. Method and general patterns of variation," *Am. J. Phys. Anthropol.*, vol. 60, no. 3, pp. 359–381, 1983.
- [134] S. L. Delp, J. P. Loan, M. G. Hoy, F. E. Zajac, E. L. Topp, and J. M. Rosen, "An interactive graphics-based model of the lower extremity to study orthopaedic surgical procedures.," *IEEE Trans. Biomed. Eng.*, vol. 37, no. 8, pp. 757–67, Aug. 1990.
- [135] I. T. Haider, A. D. Speirs, P. E. Beaulé, and H. Frei, "Influence of ingrowth regions on bone remodelling around a cementless hip resurfacing femoral implant.," *Comput. Methods Biomech. Biomed. Engin.*, vol. 18, no. April 2014, pp. 37–41, 2014.
- [136] M. Krcah, G. Székely, and R. Blanc, "Fully automatic and fast segmentation of the femur bone from 3D-CT images with no shape prior," in *Biomedical Imaging: From Nano to Micro, 2011 IEEE International Symposium*, 2011.
- [137] Q. Fang and D. A. Boas, "Tetrahedral mesh generation from volumetric binary and gray-scale images," *2009 Int. Symp. Biomed. Imaging From Nano to Micro*, 2009.
- [138] J. Schöberl, "NETGEN An advancing front 2D/3D-mesh generator based on abstract rules," *Comput. Vis. Sci.*, vol. 52, pp. 41–52, 1997.
- [139] G. Duda, E. Schneider, and E. Chao, "Internal forces and moments in the femur during walking," *J. Biomech.*, vol. 30, no. 9, 1997.

- [140] J. H. Keyak, S. Sigurdsson, G. Karlsdottir, D. Oskarsdottir, A. Sigmarsdottir, S. Zhao, J. Kornak, T. B. Harris, G. Sigurdsson, B. Y. Jonsson, K. Siggeirsdottir, G. Eiriksdottir, V. Gudnason, and T. F. Lang, “Male-female differences in the association between incident hip fracture and proximal femoral strength: a finite element analysis study.,” *Bone*, vol. 48, no. 6, pp. 1239–45, Jun. 2011.
- [141] D. L. Kopperdahl and T. M. Keaveny, “Yield strain behavior of trabecular bone.,” *J. Biomech.*, vol. 31, no. 7, pp. 601–8, Jul. 1998.
- [142] J. de Vree, W. Brekelmans, and M. Van Gils, “Comparison of nonlocal approaches in continuum damage mechanics,” *Comput. Struct.*, vol. 7949, no. 94, 1995.
- [143] S. van den Munckhof and a a Zadpoor, “How accurately can we predict the fracture load of the proximal femur using finite element models?,” *Clin Biomech (Bristol, Avon)*, vol. 29, pp. 373–380, 2014.
- [144] R. Hambli, H. Katerchi, and C.-L. Benhamou, “Multiscale methodology for bone remodelling simulation using coupled finite element and neural network computation.,” *Biomech. Model. Mechanobiol.*, vol. 10, no. 1, pp. 133–45, Feb. 2011.
- [145] J. S. Kang, K. H. Moon, J. S. Shin, and E. H. Shin, “Clinical Results of Internal Fixation of Subcapital Femoral Neck Fractures,” pp. 146–152, 2016.
- [146] R. Barnes, J. Brown, and R. Garden, “Subcapital Fractures of the Femur,” *JBJS(Br)*, vol. 58–B, pp. 2–24, 1976.
- [147] a E. Anderson, B. J. Ellis, and J. a Weiss, “Verification, Validation and Sensitivity Studies in Computational Biomechanics,” *Comput. Methods Biomech. Biomed. Engin.*,

- vol. 10, no. 3, pp. 1171–184, 2012.
- [148] L. Schwer, H. Mair, and R. Crane, “Guide for verification and validation in computational solid mechanics,” *Am. Soc. Mech. Eng. ASME ...*, 2006.
- [149] L. Harvey, R. Mitchell, H. Brodaty, B. Draper, and J. Close, “Differing trends in fall-related fracture and non-fracture injuries in older people with and without dementia,” *Arch. Gerontol. Geriatr.*, vol. 67, pp. 61–67, 2016.
- [150] K. Endo, S. Yamada, M. Todoh, M. Takahata, N. Iwasaki, and S. Tadano, “Structural strength of cancellous specimens from bovine femur under cyclic compression.,” *PeerJ*, vol. 4, p. e1562, 2016.
- [151] R. Hambli, S. Frikha, H. Toumi, and J. M. R. S. Tavares, “Finite element prediction of fatigue damage growth in cancellous bone.,” *Comput. Methods Biomech. Biomed. Engin.*, vol. 19, no. 5, pp. 563–70, 2016.
- [152] P. Purcell, S. Tiernan, F. McEvoy, and S. Morris, “Strong similarities in the creep and damage behaviour of a synthetic bone model compared to human trabecular bone under compressive cyclic loading,” *J. Mech. Behav. Biomed. Mater.*, vol. 48, pp. 51–59, 2015.
- [153] F. M. Lambers, A. R. Bouman, C. M. Rimnac, and C. J. Hernandez, “Microdamage caused by fatigue loading in human cancellous bone: relationship to reductions in bone biomechanical performance.,” *PLoS One*, vol. 8, no. 12, p. e83662, Jan. 2013.
- [154] L. Rapillard, M. Charlebois, and P. K. Zysset, “Compressive fatigue behavior of human vertebral trabecular bone.,” *J. Biomech.*, vol. 39, no. 11, pp. 2133–9, Jan. 2006.
- [155] M. McDowell, C. Fryar, C. Ogden, and K. Flegal, “Anthropometric reference data for

- children and adults: United States, 2003-2006,” *Natl. Health Stat. Report.*, no. 10, pp. 2003–2006, 2008.
- [156] K. E. S. Poole, P. M. Mayhew, C. M. Rose, J. K. Brown, P. J. Bearcroft, N. Loveridge, and J. Reeve, “Changing structure of the femoral neck across the adult female lifespan,” *J. Bone Miner. Res.*, vol. 25, no. 3, pp. 482–91, Mar. 2010.
- [157] A. El Maghraoui and C. Roux, “DXA scanning in clinical practice,” *Qjm*, vol. 101, no. 8, pp. 605–617, 2008.
- [158] R. B. Mazess, “On aging bone loss,” *Clin Orthop*, no. 165, pp. 239–252, 1982.
- [159] E. Dall’ara, B. Luisier, R. Schmidt, M. Pretterklieber, F. Kainberger, P. Zysset, and D. Pahr, “DXA predictions of human femoral mechanical properties depend on the load configuration,” *Med. Eng. Phys.*, May 2013.
- [160] J. H. Keyak, J. M. Meagher, H. B. Skinner, and C. D. Mote, “Automated three-dimensional finite element modelling of bone: a new method,” *J. Biomed. Eng.*, vol. 12, no. 5, pp. 389–397, 1990.
- [161] V. Bousson, A. Le Bras, F. Roqueplan, Y. Kang, D. Mitton, S. Kolta, C. Bergot, W. Skalli, E. Vicaud, W. Kalender, K. Engelke, and J. D. Laredo, “Volumetric quantitative computed tomography of the proximal femur: Relationships linking geometric and densitometric variables to bone strength. Role for compact bone,” *Osteoporos. Int.*, vol. 17, no. 6, pp. 855–864, 2006.
- [162] Z. Bazant and J. Planas, *Fracture and Size Effect in Concrete and Other Quasibrittle Materials*. Boca Raton, Boston, London, New York, Washington D.C: CRC Press, 1997.

- [163] I. T. Haider, A. D. Speirs, and H. Frei, “Effect of boundary conditions, impact loading and hydraulic stiffening on femoral fracture strength.,” *J. Biomech.*, vol. 46, no. 13, pp. 2115–21, Sep. 2013.
- [164] S. N. Robinovitch, E. T. Hsiao, R. Sandler, J. Cortez, Q. Liu, and G. D. Paiement, “Prevention of falls and fall-related fractures through biomechanics.,” *Exerc. Sport Sci. Rev.*, vol. 28, no. 2, pp. 74–79, 2000.
- [165] S. Nawathe, H. Akhlaghpour, M. L. Bouxsein, and T. M. Keaveny, “Microstructural failure mechanisms in the human proximal femur for sideways fall loading.,” *J. bone Miner. Res.*, pp. 1–29, Jul. 2013.
- [166] E. Verhulp, B. van Rietbergen, and R. Huiskes, “Comparison of micro-level and continuum-level voxel models of the proximal femur.,” *J. Biomech.*, vol. 39, no. 16, pp. 2951–7, Jan. 2006.
- [167] R. Hambli, “Micro-CT finite element model and experimental validation of trabecular bone damage and fracture.,” *Bone*, vol. 56, no. 2, pp. 363–74, Oct. 2013.
- [168] Dassault-Systemes, “Submodelling,” in *ABAQUS Analysis User’s Manual (6.11)*, Vélizy-Villacoublay, France.
- [169] M. Giglio, “FEM submodelling fatigue analysis of a complex helicopter component,” *Int. J. Fatigue*, vol. 21, no. 5, pp. 445–455, May 1999.
- [170] N. K. Mandal and M. Dhanasekar, “Sub-modelling for the ratchetting failure of insulated rail joints,” *Int. J. Mech. Sci.*, vol. 75, pp. 110–122, 2013.

## Appendix A: Verification of the Gradient Enhanced Quasi-Brittle Finite Element Code

The gradient enhanced quasi-brittle finite element, described by Equation 37 and first used in Chapter 5, was implemented as a custom subroutine in the commercial finite element package, ABAQUS. The mathematical implementation was originally described by Peerlings et al [79], [113], who also compared their simulation results against experimental evidence. One of these simulations was recreated in order to verify that the code written for this thesis worked as intended.

The simulation predicted damage evolution of a notched specimen loaded in tension (Figure A-1). The material was modeled as concrete, with an elastic modulus of 18 GPa and poisson's ratio of 0.2. Damage evolution was computed based on the modified von Mises strain (equation 44), with a compressive/tensile strength ratio of 10.

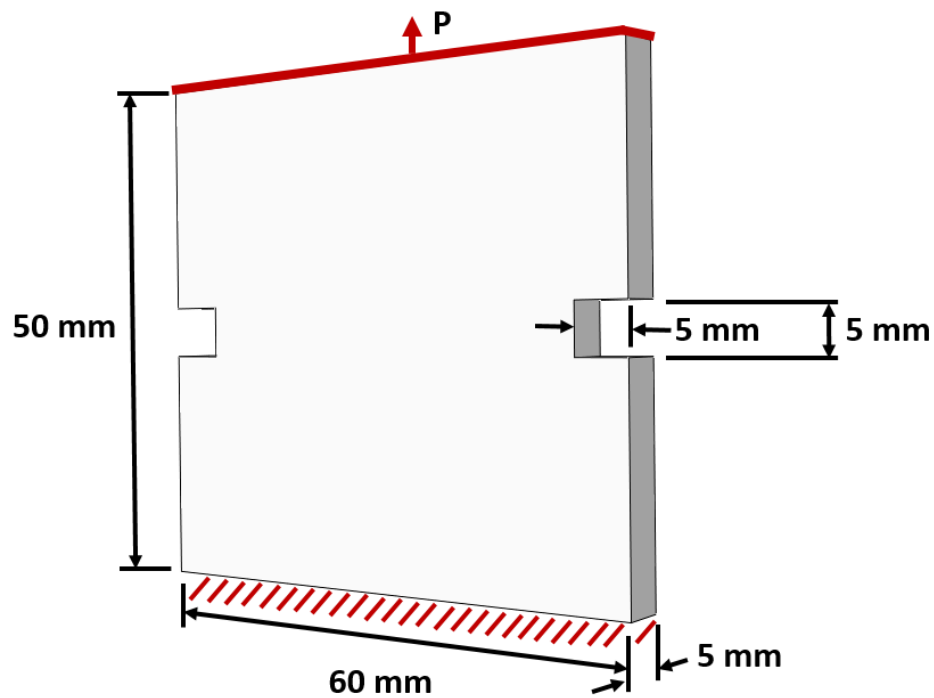


Figure A-1 Dimensions and BCs of simulated test coupon used for code verification. The coupon was fixed along bottom surface and a distributed load (P) was applied to the top surface.

The final version of the code implemented for this thesis is provided at the end of this Appendix. The code was able to closely match Peerling's previously validated results; peak stress was predicted to within 2% and the pattern of damage evolution matched closely (Figure A-2). Additional simulations were performed in order to explore the effect of gradient enhancement on simulation results. The mesh was refined, from 16000 to 31000 elements and the simulation was repeated. As shown in Figure A-3, mesh refinement had little influence on the results if gradient-enhancement remained enabled. However, the results changed significantly if gradient enhancement was disabled, i.e., damage evolution was computed as a function of local strains only. In this case, damage became limited to a narrow band, exactly two elements wide.

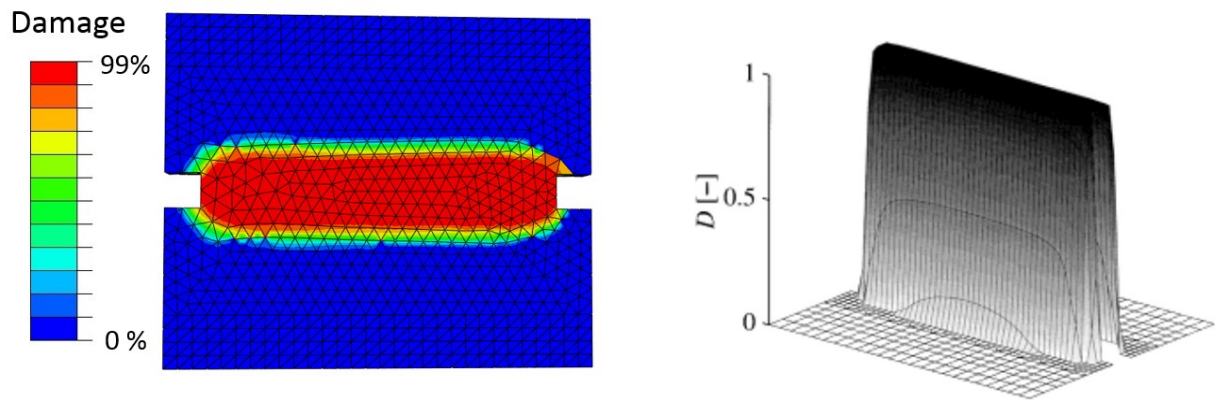


Figure A-2 Damage evolution pattern predicted by the gradient-enhanced FE code implemented in this thesis (LEFT) compared to previously published simulation results (RIGHT). In both cases, damage occurred in a 10 mm wide band between the notches.

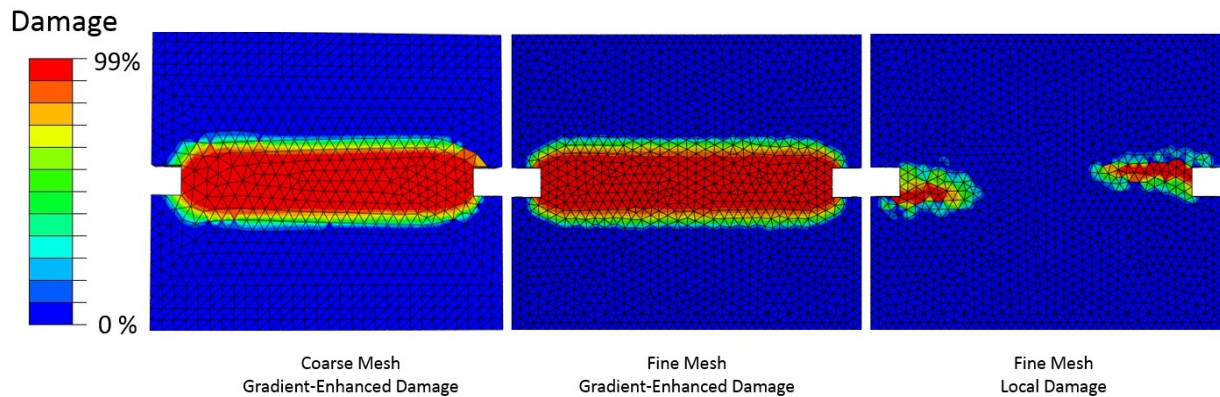


Figure A-3 Influence of mesh refinement and gradient enhancement. When the gradient-enhanced damage model was used, both coarse (LEFT) and fine (MIDDLE) mesh densities resulted in identical predictions of damage pattern. Using a local damage model resulted in damage evolution limited to a narrow band, exactly two elements wide (RIGHT).

### FORTRAN Implementation of the Quasi-Brittle Element

```

SUBROUTINE UEL(RHS,AMATRX,SVARS,ENERGY,NDOFEL,NRHS,NSVARS, &
PROPS,NPROPS,COORDS,MCRD,NNODE,U,DU,V,A,JTYPE,TIME,DTIME, &
KSTEP,KINC,JELEM,PARAMS,NDLOAD,JDLTYP,ADLMAG,PREFEF,NPREFD, &
LFLAGS,MLVARX,DDL MAG,MDLOAD,PNEWDT,JPROPS,NJPROP,PERIOD)

```

!

```

INCLUDE 'ABA_PARAM.INC'

```

```

!
DIMENSION RHS(MLVARX,*),AMATRIX(NDOFEL,NDOFEL),PROPS(*), &
SVARS(*),ENERGY(8),COORDS(MCRD,NNODE),U(NDOFEL), &
DU(MLVARX,*),V(NDOFEL),A(NDOFEL),TIME(2),PARAMS(*), &
JDLTYP(MDLOAD,*),ADLMAG(MDLOAD,*),DDL MAG(MDLOAD,*), &
PREDEF(2,NPREDF,NNODE),LFLAGS(*),JPROPS(*)

! U - default [U1x, U1y, U1z,U1e, ..... U10e]
! AMATRIX - tangent matrix such that AMATRIX*dU= R
! SVARS - 1-4 = max damage at integration points 1-4
! 5 = element density (kg/m3)
! 6 = element characteristic length
! 7 = ignore damage flag 2000=ignore damage effects, otherwise do not
! 8-11 = failure flag - 0 = not failed
! - 1 = tension failure
! - 2 = compression failure

! initialize vars

Real*8 charlength, ignoreflag, dummyYoung

Real*8, Dimension(4,4) :: Kee,KeeTemp,IPquad
Real*8, Dimension(30,30) :: Kuu,KuuTemp
Real*8, Dimension(6,30) :: Bquad
Real*8, Dimension(4) :: curlIPcoords
Real*8, Dimension(6,6) :: D, DunDam
Real*8, Dimension(30,4) :: Kue,KueTemp
Real*8, Dimension(1,4) :: Nlinear
Real*8, Dimension(6,1) :: strains,Stress,S
Real*8, Dimension(4,30) :: Keu,KeuTemp
Real*8, Dimension(3,4) :: Blin
Real*8, Dimension(4,1) :: Fe,Eeq,test
Real*8, Dimension(30,1) :: Fu,FuTemp, KuuU
Real*8, Dimension(4) :: IPlin,maxdam
Real*8, Dimension(10,3) :: dummycoords
Real*8, Dimension(1,1) :: EeqScalarTemp
Real*8, Dimension(30,1)::U2d
Real*8 Dnew,q, Jdet, EeqScalar, density,failflag, nonlocalscale,L

! initialize variables, just in case

D(:,:)=0.
Bquad(:,:)=0.

```

```
curlPcoords(:)=0.  
Nlinear(:,:)=0.  
strains(:,:)=0.  
Blin(:,:)=0.  
Fe(:,:)=0.  
IPquad(:,:)=0.  
IPlin(:)=0.  
U2d(:,:)=0.  
S(:,:)=0.  
Eeq(:,:)=0.  
test(:,:)=0.  
dummyYoung=0.  
dummycoords(:,:)=0.  
EeqScalar=0.
```

```
Kuu(:,:)=0.  
Kue(:,:)=0.  
Keu(:,:)=0.  
KuuTemp(:,:)=0.  
KueTemp(:,:)=0.  
KeuTemp(:,:)=0.  
KeeTemp(:,:)=0.  
FuTemp(:,:)=0.  
Fu(:,:)=0.
```

```
Kuu(:,:)=0.  
Kue(:,:)=0.  
Keu(:,:)=0.  
Kee(:,:)=0.  
Fu(:,:)=0.  
Stress(:,:)=0.  
strains(:,:)=0.
```

```
q=0.  
Dnew=0.  
Jdet=0.
```

```
density=SVARS(5)  
maxdam(:)=SVARS(1:4)  
charlength=SVARS(6)  
ignoreflag=SVARS(7)  
!failflag=SVARS(8)
```

```
! ***** following section builds kuu kue matries using 4 pnt gauss  
integration *****
```

```

!if (TIME == 0) then
  !OPEN(8, FILE = "C:\research\uelDamage\2elementRiks\DEBUG.txt", ACCESS =
'APPEND')
  !WRITE(8,*) "DOF#: ", NDOFEL
  !Close(8)
!end if

! use quadratic element integration points
IPquad(1,1)=0.58541020
IPquad(2,1)=0.13819660
IPquad(3,1)=0.13819660
IPquad(4,1)=0.13819660

IPquad(1,2)=0.13819660
IPquad(2,2)=0.58541020
IPquad(3,2)=0.13819660
IPquad(4,2)=0.13819660

IPquad(1,3)=0.13819660
IPquad(2,3)=0.13819660
IPquad(3,3)=0.58541020
IPquad(4,3)=0.13819660

IPquad(1,4)=0.13819660
IPquad(2,4)=0.13819660
IPquad(3,4)=0.13819660
IPquad(4,4)=0.58541020
dummycoords=transpose(COORDS)

! loop through each quadratic integration point. Calculate Kuu, Kue, Keu, and
! Residual force

Do i=1,4

! OPEN(8, FILE = "D:\Ifaz\Study2muscle\FemurFracture\uelDama
! &ge\DEBUG.txt", ACCESS = 'APPEND')

! WRITE(8,*) "*****i: "
! WRITE(8,*) i
! Close(8)

!update guass point coords
Do j=1,4
  curIPcoords(j)=IPquad(j,i)
end do

```

!initialize matrices. Get Bquad and elasticity matrix, using damage from previous increment

```
!Bmatrix,Jdet,NodeCoords,NatCoords  
call createBQuad(Bquad,Jdet,dummycoords,curIPcoords)
```

```
!Calculat Fu  
U2d(:,1)=U(1:30)  
Strains=MATMUL(Bquad, U2d )
```

```
!evaluate nonlocal strain for use in damage evolution/stress computaion  
call createNLinear(Nlinear, curIPcoords)  
Eq(:,1)=U(31:34)
```

```
EeqScalarTemp=MATMUL(Nlinear,Eeq)  
EeqScalar=EeqScalarTemp(1,1)
```

!Stress, Strains, MaxDam,density, ignoreFlag, damIncreasesFlag, damaged elasticity matrix

```
call CalcStress(Stress,Strains,maxdam(i),density,ignoreflag,q,D, EeqScalar,failflag)  
!UPDATE STIFFNESS and STATE Variable  
!D=D*(1.0-maxdam(i))  
SVARS(i)=maxdam(i)
```

```
!Calculate nodal reaction forces by integrating stress  
FuTemp= MATMUL( transpose(Bquad),Stress)  
FuTemp= FuTemp*0.25*(Jdet/6.)  
Fu=Fu+FuTemp
```

```
!Calculate Kuu
```

\*\*\*\*\*

```
! call createBQuad(Bquad,Jdet,transpose(Coords), curIPcoords)
```

```
KuuTemp=MATMUL(transpose(Bquad),MATMUL(D,Bquad))
```

! Guass wieght is 0.25 for all points, need to multiply by Jdet/6 due to conversion from dxdydz into dC1 dC2... etc in volume integral

```
KuuTemp=0.25*KuuTemp*(Jdet/6.)
```

```
Kuu=Kuu+KuuTemp
```

```
!Calculate Kue
```

\*\*\*\*\*

\*\*\*\*\*

```
call createNLinear(Nlinear,curIPcoords)
```

```
U2d(:,1)=U(1:30)
```

```

      strains=MATMUL(Bquad, U2d )
!      strains=MATMUL(D,Bquad )

      !recalculate undamaged modulus
      dummyYoung=6.95*( (density/1000.)**1.49)*1000000000.
      call createDelastic(DunDam,density,dummyYoung)

      KueTemp= MATMUL(transpose(Bquad), MATMUL(DunDam,
MATMUL(strains,q*Nlinear) ) )
      !Gauss weight is 0.25 for all points, negative as per def of Kue, again need to include
Jdet/6 =volume
      KueTemp= -0.25*KueTemp*(Jdet/6.)

      Kue=Kue+KueTemp

      !Calculate Keu
*****
*****
      call CalcS( S, strains)

      KeuTemp=MATMUL(transpose(Nlinear), MATMUL(transpose(S),Bquad))
      KeuTemp=-0.25*KeuTemp*(Jdet/6.)

      Keu=Keu+KeuTemp

end do

!FU=KuuU

! use one point rule to evaluate Kee and Fe, which are based on linear shape functions
! the integration point for 1 pnt rule:
IPlin(1)=0.25
IPlin(2)=0.25
IPlin(3)=0.25
IPlin(4)=0.25

! Compute Kee

call createBLinear(Blin,dummycoords)

call createNLinear(Nlinear, IPlin)

      Kee= (MATMUL(transpose(Nlinear), Nlinear) + MATMUL( transpose(Blin),Blin))*
charlength ) * (Jdet/6.)

! build Fe

```

```

! evaluate strains at linear integration point, compute equivalent strain

! compute Fe using one point guass integration rule
! call calcEquivalentStrain(strains,EeqScalar)
! Eeq(:,1)=U(31:34)
! EeqScalar=MATMUL(Nlinear,Eeq)

! now build stiffness and residual vectors for ABAQUS, update SVARS as needed

dummycoords=transpose(COORDS)
call createBQuad(Bquad,Jdet, dummycoords, IPlin)
strains=MATMUL(Bquad, U2d)
call calcEquivalentStrain(strains, EeqScalar)

! Fe = MATMUL(transpose(Nlinear), MATMUL(Nlinear,Eeq))*(Jdet/6.)
Fe = transpose(Nlinear)*EeqScalar* (Jdet/6.)
Eeq(:,1)=U(31:34)
test= Fe-MATMUL(Kee,Eeq)

if(ignoreFlag .GT. 1500.0) then
test(:,:)=0.0
Kue(:,:)=0.0
Kee(:,:)=0.0
Keu(:,:)=0.0
end if

L= ( (Jdet/6.)*6.0*sqrt(2.0) )**(1.0/3.0)
dummyYoung=6.95*( (density/1000.)**1.49)*1000000000.
nonlocalscale= (dummyYoung/L)* (1.0-(
(SVARS(1)+SVARS(2)+SVARS(3)+SVARS(4))/4.0 ) )

RHS(1:30,1)= -1.0*Fu(1:30,1)
RHS(31:34,1)= test(:,1)*nonlocalscale

AMATRX(1:30,1:30)=Kuu
AMATRX(1:30,31:34)=Kue
AMATRX(31:34,1:30)=Keu*nonlocalscale
AMATRX(31:34,31:34)=Kee*nonlocalscale

IF (NRHS.EQ.2) THEN
RHS(:,2) = RHS(:,2)
END IF

```

```
RETURN
END
```

```
!*****
```

```
subroutine calcEquivalentStrain(STRAN, EeqScalar)
implicit none
```

```
Real*8, Dimension(6,1) :: STRAN
Real*8 EeqScalar, E1,E2,E3,E4,E5,E6
```

```
E1=STRAN(1,1)
E2=STRAN(2,1)
E3=STRAN(3,1)
E4=STRAN(4,1)
E5=STRAN(5,1)
E6=STRAN(6,1)
```

```
EeqScalar=0.0
```

```
EeqScalar = 0.2884615385D0 * E1 + 0.2884615385D0 * E2 + 0.2884615385D0 * E3 +
0.3846153846D0 * sqrt(0.5625000000D0 * (E1 + E2 + E3) ** 2 +0.3076923077D1 * E1 ** 2 +
0.3076923077D1 * E2 ** 2 + 0.3076923077D1 * E3 ** 2 - 0.3076923077D1 * E1 * E2 -
0.3076923077D1 * E2 * E3 - 0.3076923077D1 * E3 * E1 + 0.2307692308D1 * E4 ** 2 +
0.2307692308D1 * E6 ** 2 + 0.2307692308D1 * E5 ** 2)
```

```
RETURN
END
```

```
!*****
```

```
*****
```

```
subroutine CalcStress(Stress, Strains, MaxDam,density, ignoreFlag, q,DDSDDE,
EeqScalar,failflag)
implicit none
```

```
Real*8, Dimension(6,1) :: Stress, Strains
Real*8, Dimension(6,6) :: DDSDDE
Real*8, Dimension(15) :: ARRAY, JARRAY
Real*8 density, ignoreFlag, MaxDam
integer i
integer K1
integer K2
Real*8 Dnew
Real*8 k ! damage parameter, defined in Hambli
Real*8 n ! damage exponent
```

```

Real*8 Dct !-critical damage, tension
Real*8 Dcc !-critical damage, compression
Real*8 Dc
Real*8 EeqScalar !- Equivalent strain as defined in Hambli
Real*8 Efc !-fracture strains in compression and tension
Real*8 HydroS
Real*8 Eft
Real*8 Ef !-fracture strain for current stress state
Real*8 Ey !- yield strain
Real*8 pois ! poisson's ratio
Real*8 Young ! young's modulus
CHARACTER*3 FLGRAY(15)
Real*8 a !placeholder variable
Real*8 b
Real*8 c
Real*8 q
Real*8 failflag, alpha

Young=6.95*( (density/1000.)**1.49)*1000000000.
pois=0.3
! Check if material is cortical or trabecular bone, assign properties accordingly

if (density .GE. 725.0) then
  Ef=0.
  Eft=0.0157
  Efc=0.025
  Ey=0
  n=1.25
  Dcc=0.99
  Dct=0.99
  !Dct=0.5
else
  Ef=0.
  Eft=0.025
  Efc=0.04
  Ey=0
  n=1.25
  Dcc=0.99
  Dct=0.99
end if

alpha=100.0

Ef=Eft
Dc=Dct

```

```

! update damage unless element is flagged as ignored
Dnew=0.0
if (ignoreFlag .LT. 1500.0) then

    if (EeqScalar .LT. Ey) then
        Dnew=0.
    elseif ( EeqScalar .LT. Ef) then
        Dnew=alpha*( (EeqScalar)**n)
    else
        Dnew=Dc
    end if

end if

! make sure damage can't exceed the failure damage!
if (Dnew .GT. Dc) then
    Dnew = Dc
end if

!check if the calculated damage is higher than the highest damage seen, at this point, so far
!update variables accordingly
if (Dnew .LE. MaxDam) then
    Dnew=MaxDam ! new damage is lower or equal to previous max damage; keep old,
highest damage
    q=0.0
else
    MaxDam=Dnew !new damage is higher than previous; update state(2) to track Dnew as the
highest damage seen
    q= (alpha*n)* ( (EeqScalar)**(n-1.) )
end if

!check if material has failed based on current strains
!for failure in tension, reduce stiffness to ~zero
!for failure in compression, let stiffness remain at ~50% to model self contact (consolidation)
!in both instances damage is no longer increasing so set q=0
!if no failure is detected, simply degrade young's modulus by the damage instead

if ( (Dnew .GE. Dct).and.(ignoreflag .LT. 1500.0) ) then

    !Young=0.0
    Dnew=Dct
    Young=(1.-Dnew)*6.95*( (density/1000.)**1.49)*1000000000.
    q=0.0
    ! failflag=1.0

```

```

elseif ( (ignoreflag) .LT. 1500.0) then
  Young=(1.-Dnew)*6.95*( (density/1000.)**1.49)*1000000000.
end if

```

```

!check if failflag says material has failed based on failflag
!if (failflag .GE. 1.5) then !compression failure
! Dnew=Dcc
! Young=(1.-Dnew)*6.95*( (density/1000.)**1.49)*1000000000.
! q=0.0
! failflag =2.0
!elseif (failflag .GE. 0.5) then !tension failure
! Dnew=Dct
! Young=(1.-Dnew)*6.95*( (density/1000.)**1.49)*1000000000.
! q=0.0
! failflag=1.0
!end if

```

```

!Build elastic matrix
call createDelastic(DDSDDE, density, Young)

```

```

!Stress = stiffness*strain
Stress= MATMUL(DDSDDE, Strains)

```

```

RETURN
END

```

```

!*****

```

```

subroutine CalcS( S, STRAN)
implicit none

```

```

Real*8, Dimension(6,1) :: S, STRAN
Real*8 EeqScalar
EeqScalar=0.

```

```

!S exists only for nonzero strains, otherwise treat it as zero

```

```

if (EeqScalar .GT. 0.00001 ) then

```

```

  S(1,1) = 0.3879310345D0 + 0.1724137931D0 * (0.1265625000D1 * (STRAN(1,1) +
STRAN(2,1) &
  + STRAN(3,1)) ** 2 + 0.3431952662D1 * STRAN(1,1) ** 2 + 0.3431952662D1 *
STRAN(2,1) ** 2 &

```

$$\begin{aligned}
& + 0.3431952662D1 * STRAN(3,1) ** 2 - 0.3431952662D1 * STRAN(1,1) * STRAN(2,1) - \\
& 0.3431952662D1 * \& \\
& STRAN(2,1) * STRAN(3,1) - 0.3431952662D1 * STRAN(3,1) * STRAN(1,1) + \\
& 0.2573964497D1 * STRAN(4,1) ** \& \\
& 2 + 0.2573964497D1 * STRAN(6,1) ** 2 + 0.2573964497D1 * STRAN(5,1) ** 2) ** (- \\
& 0.1D1 / 0.2D1) \& \\
& * (0.9395155324D1 * STRAN(1,1) - 0.900702662D0 * STRAN(2,1) - 0.900702662D0 * \\
& STRAN(3,1))
\end{aligned}$$

$$\begin{aligned}
S(2,1) = & 0.3879310345D0 + 0.1724137931D0 * (0.1265625000D1 * (STRAN(1,1) + \\
& STRAN(2,1) \& \\
& + STRAN(3,1)) ** 2 + 0.3431952662D1 * STRAN(1,1) ** 2 + 0.3431952662D1 * \\
& STRAN(2,1) ** 2 \& \\
& + 0.3431952662D1 * STRAN(3,1) ** 2 - 0.3431952662D1 * STRAN(1,1) * STRAN(2,1) - \\
& 0.3431952662D1 \& \\
& * STRAN(2,1) * STRAN(3,1) - 0.3431952662D1 * STRAN(3,1) * STRAN(1,1) + \\
& 0.2573964497D1 * STRAN(4,1) ** 2 \& \\
& + 0.2573964497D1 * STRAN(6,1) ** 2 + 0.2573964497D1 * STRAN(5,1) ** 2) ** (-0.1D1 \\
& / 0.2D1) \& \\
& * (-0.900702662D0 * STRAN(1,1) + 0.9395155324D1 * STRAN(2,1) - 0.900702662D0 * \\
& STRAN(3,1))
\end{aligned}$$

$$\begin{aligned}
S(3,1) = & 0.3879310345D0 + 0.1724137931D0 * (0.1265625000D1 * (STRAN(1,1) + \\
& STRAN(2,1) \& \\
& + STRAN(3,1)) ** 2 + 0.3431952662D1 * STRAN(1,1) ** 2 + 0.3431952662D1 * \\
& STRAN(2,1) ** 2 \& \\
& + 0.3431952662D1 * STRAN(3,1) ** 2 - 0.3431952662D1 * STRAN(1,1) * STRAN(2,1) - \\
& 0.3431952662D1 \& \\
& * STRAN(2,1) * STRAN(3,1) - 0.3431952662D1 * STRAN(3,1) * STRAN(1,1) + \\
& 0.2573964497D1 * STRAN(4,1) ** 2 \& \\
& + 0.2573964497D1 * STRAN(6,1) ** 2 + 0.2573964497D1 * STRAN(5,1) ** 2) ** (-0.1D1 \\
& / 0.2D1) \& \\
& * (-0.900702662D0 * STRAN(1,1) - 0.900702662D0 * STRAN(2,1) + 0.9395155324D1 * \\
& STRAN(3,1))
\end{aligned}$$

$$\begin{aligned}
S(4,1) = & 0.8875739645D0 * (0.1265625000D1 * (STRAN(1,1) + STRAN(2,1) + \\
& STRAN(3,1)) ** 2 + 0.3431952662D1 \& \\
& * STRAN(1,1) ** 2 + 0.3431952662D1 * STRAN(2,1) ** 2 + 0.3431952662D1 \& \\
& * STRAN(3,1) ** 2 - 0.3431952662D1 * STRAN(1,1) * STRAN(2,1) - 0.3431952662D1 * \\
& STRAN(2,1) * STRAN(3,1) - \& \\
& 0.3431952662D1 * STRAN(3,1) * STRAN(1,1) + 0.2573964497D1 * STRAN(4,1) ** 2 + \\
& 0.2573964497D1 \& \\
& * STRAN(6,1) ** 2 + 0.2573964497D1 * STRAN(5,1) ** 2) ** (-0.1D1 / 0.2D1) * \\
& STRAN(4,1)
\end{aligned}$$

```

S(5,1) = 0.8875739645D0 * (0.1265625000D1 * (STRAN(1,1) + STRAN(2,1) +
STRAN(3,1)) ** 2 + 0.3431952662D1 &
* STRAN(1,1) ** 2 + 0.3431952662D1 * STRAN(2,1) ** 2 + 0.3431952662D1 &
* STRAN(3,1) ** 2 - 0.3431952662D1 * STRAN(1,1) * STRAN(2,1) - 0.3431952662D1 *
STRAN(2,1) * STRAN(3,1) - &
0.3431952662D1 * STRAN(3,1) * STRAN(1,1) + 0.2573964497D1 * STRAN(4,1) ** 2 +
0.2573964497D1 &
* STRAN(6,1) ** 2 + 0.2573964497D1 * STRAN(5,1) ** 2) ** (-0.1D1 / 0.2D1) *
STRAN(5,1)

```

```

s(6,1) = 0.8875739645D0 * (0.1265625000D1 * (STRAN(1,1) + STRAN(2,1) +
STRAN(3,1)) ** 2 + 0.3431952662D1 &
* STRAN(1,1) ** 2 + 0.3431952662D1 * STRAN(2,1) ** 2 + 0.3431952662D1 &
* STRAN(3,1) ** 2 - 0.3431952662D1 * STRAN(1,1) * STRAN(2,1) - 0.3431952662D1 *
STRAN(2,1) * STRAN(3,1) - &
0.3431952662D1 * STRAN(3,1) * STRAN(1,1) + 0.2573964497D1 * STRAN(4,1) ** 2 +
0.2573964497D1 &
* STRAN(6,1) ** 2 + 0.2573964497D1 * STRAN(5,1) ** 2) ** (-0.1D1 / 0.2D1) *
STRAN(6,1)

```

```

else
  S(:,:)=0
end if

```

```

RETURN
END

```

```

!*****

```

```

! Delastic = [output] 6x6 elasticity matrix
! density = density at point, in kg/m3

```

```

subroutine createDelastic(DDSDDE, density, Young)
implicit none

```

```

Real*8, Dimension(6,6):: DDSDDE
Real*8 Young, pois,b,a,c
Real*8, INTENT(IN) :: density

```

```

pois=0.3

```

!if zero young's modulus was passed into the function, calc young's mod for an undamaged material (this mode used by main program to get kue)

!otherwise use the value given to the function (this mode used by calcStress to make a 6x6 elasticity matrix)

!if ( Young .LT. 1 ) then

! Young=6.95\*( ( density/1000.0)\*\*1.49 ) \*1000000000.0

!end if

a=Young/( (1.+pois)\*(1.-(2.\*pois)) )

b=1.-pois

c=(1.-(2.\*pois))/2.

DDSDDE(1,1)=b\*a

DDSDDE(1,2)=pois\*a

DDSDDE(1,3)=pois\*a

DDSDDE(1,4)=0.

DDSDDE(1,5)=0.

DDSDDE(1,6)=0.

DDSDDE(2,1)=pois\*a

DDSDDE(2,2)=b\*a

DDSDDE(2,3)=pois\*a

DDSDDE(2,4)=0.

DDSDDE(2,5)=0.

DDSDDE(2,6)=0.

DDSDDE(3,1)=pois\*a

DDSDDE(3,2)=pois\*a

DDSDDE(3,3)=b\*a

DDSDDE(3,4)=0.

DDSDDE(3,5)=0.

DDSDDE(3,6)=0.

DDSDDE(4,1)=0.

DDSDDE(4,2)=0.

DDSDDE(4,3)=0.

DDSDDE(4,4)=c\*a

DDSDDE(4,5)=0.

DDSDDE(4,6)=0.

DDSDDE(5,1)=0.

DDSDDE(5,2)=0.

DDSDDE(5,3)=0.

```
DDSDDE(5,4)=0.  
DDSDDE(5,5)=c*a  
DDSDDE(5,6)=0.
```

```
DDSDDE(6,1)=0.  
DDSDDE(6,2)=0.  
DDSDDE(6,3)=0.  
DDSDDE(6,4)=0.  
DDSDDE(6,5)=0.  
DDSDDE(6,6)=c*a
```

```
RETURN  
END
```

```
!*****
```

```
! Creates the B matrix for linear tet  
! Bmatrix = [output] 3x4 matrix of partial derivatives WRT global coords  
! NodeCoords = 10x3 matrix of nodal coordinates [node, coordindex]  
! for linear tet, B is constant within the tet
```

```
subroutine createBLinear(Bmatrix, NodeCoords)
```

```
implicit none
```

```
Real*8, Dimension(3,4) :: Bmatrix(3,4)  
Real*8, Dimension(10,3) :: NodeCoords
```

```
Real*8 x1, x2,x3,y1,y2,y3,z1,z2,z3,x21,y23,z34,y34,z23,x32, z12,y12,x43,V,x4,y4,z4,  
a1,b1,c1,a2,b2,c2,a3,b3,c3,a4,b4,c4  
Real*8  
y42,z32,y32,z42,x42,y31,z43,z13,z31,x13,x31,y43,x34,y13,y24,z14,y14,z24,x14,x24,z21,y21,x  
12, Jdet, x23, x41, y41, z41
```

```
x1=NodeCoords(1,1)  
x2=NodeCoords(2,1)  
x3=NodeCoords(3,1)  
x4=NodeCoords(4,1)
```

```
y1=NodeCoords(1,2)  
y2=NodeCoords(2,2)  
y3=NodeCoords(3,2)
```

y4=NodeCoords(4,2)

z1=NodeCoords(1,3)

z2=NodeCoords(2,3)

z3=NodeCoords(3,3)

z4=NodeCoords(4,3)

! example contents dNdx = [dN1dx dN2dx dN3dx ..... dN10dx]

x12=x1-x2

x13=x1-x3

x14=x1-x4

x23=x2-x3

x24=x2-x4

x34=x3-x4

x21=-1.0\*x12

x31=-1.0\*x13

x41=-1.0\*x14

x32=-1.0\*x23

x42=-1.0\*x24

x43=-1.0\*x34

y12=y1-y2

y13=y1-y3

y14=y1-y4

y23=y2-y3

y24=y2-y4

y34=y3-y4

y21=-1.0\*y12

y31=-1.0\*y13

y41=-1.0\*y14

y32=-1.0\*y23

y42=-1.0\*y24

y43=-1.0\*y34

z12=z1-z2

z13=z1-z3

z14=z1-z4

z23=z2-z3

z24=z2-z4

z34=z3-z4

z21=-1.0\*z12

z31=-1.0\*z13

z41=-1.0\*z14  
z32=-1.0\*z23  
z42=-1.0\*z24  
z43=-1.0\*z34

!had these from before

x21=x2-x1  
y23=y2-y3  
z34=z3-z4  
y34=y3-y4  
z23=z2-z3  
x32=x3-x2

y34=y3-y4  
z23=z2-z3  
x32=x3-x2  
z12=z1-z2  
y12=y1-y2  
x43=x4-x3

! note Jdet=6V

Jdet=x21\*(y23\*z34-y34\*z23)+x32\*(y34\*z12-y12\*z34)+x43\*(y12\*z23-y23\*z12)

V=Jdet/6.0

a1=y42\*z32-y32\*z42  
b1=x32\*z42-x42\*z32  
c1=x42\*y32-x32\*y42  
a2=y31\*z43-y34\*z13  
b2=x43\*z31-x13\*z34  
c2=x31\*y43-x34\*y13  
a3=y24\*z14-y14\*z24  
b3=x14\*z24-x24\*z14  
c3=x24\*y14-x14\*y24  
a4=y13\*z21-y12\*z31  
b4=x21\*z13-x31\*z12  
c4=x13\*y21-x12\*y31

Bmatrix(:,:)=0.

Bmatrix(1,1)=a1/(6.0\*V)

Bmatrix(1,2)=a2/(6.0\*V)

Bmatrix(1,3)=a3/(6.0\*V)

Bmatrix(1,4)=a4/(6.0\*V)

Bmatrix(2,1)=b1/(6.0\*V)

Bmatrix(2,2)=b2/(6.0\*V)

```
Bmatrix(2,3)=b3/(6.0*V)
Bmatrix(2,4)=b4/(6.0*V)
```

```
Bmatrix(3,1)=c1/(6.0*V)
Bmatrix(3,2)=c2/(6.0*V)
Bmatrix(3,3)=c3/(6.0*V)
Bmatrix(3,4)=c4/(6.0*V)
```

```
RETURN
END
```

```
!*****
```

```
! Nmatrix = [output] 1x4 matrix of shape functions
! C(4) = 4 element vector of natural coordinates at point of interest
```

```
subroutine createNLinear(Nmatrix, C)
```

```
Real*8, Dimension(1,4) :: Nmatrix
Real*8, Dimension(4) :: C(4)
```

```
Nmatrix(1,1)= C(1)
Nmatrix(1,2)= C(2)
Nmatrix(1,3)= C(3)
Nmatrix(1,4)= C(4)
```

```
RETURN
END
```

```
! Nmatrix = [output] 3x30 matrix of shape functions
! C(4) = 4 element vector of natural coordinates at point of interest
subroutine createNQuad(Nmatrix, C)
```

```
Real*8, Dimension(10) :: N
Real*8, Dimension(3,30) :: Nmatrix
```

```
N(1)= C(1)*(2.0*C(1)-1)
N(2)= C(2)*(2.0*C(2)-1)
N(3)= C(3)*(2.0*C(3)-1)
N(4)= C(4)*(2.0*C(4)-1)
```

```
N(5)=4*C(1)*C(2)
N(6)=4*C(2)*C(3)
N(7)=4*C(3)*C(1)
N(8)=4*C(1)*C(4)
N(9)=4*C(2)*C(4)
```

$N(10)=4*C(3)*C(4)$

```
! initialize Nmatrix
Do i=1,3
  Do j=1,30
    Nmatrix(i,j)=0
  End do
End do

! loop through and place N(i) in it's correct position in the shape function matrix
Do i =1,10
  x= ((i-1)*3)+1;

  Nmatrix(1,x)=N(i)
  Nmatrix(2,x+1)=N(i)
  Nmatrix(3,x+2)=N(i)

End Do

RETURN
END
```

!\*\*\*\*\*

```
! Bmatrix =[output] 6x30 matrix of shape function derivatives
! Jdet = [output] Jacobian Determinant
! NodeCoords = 10x3 matrix of nodal coordinates [node, coordindex]
! NatCoords = 4 term vector of natural coordinates where B is evaluated
```

```
subroutine createBQuad(Bmatrix,Jdet,NodeCoords,NatCoords)
implicit none
```

```
Real*8, Dimension(6,30) :: Bmatrix
Real*8, Dimension(10,3) :: NodeCoords
Real*8, Dimension(4) :: NatCoords, a, b ,c
Real*8, Dimension(10):: dNdx, dNdy, dNdz
```

```
Real*8 Jdet,Jx1,Jy1,Jz1,Jx2,Jy2,Jz2,Jx3,Jy3,Jz3, Jx4, Jy4, Jz4, &
  Jx12, Jx13,Jx14,Jx21,Jx23,Jx24,Jx31,Jx32,Jx34,Jx41,Jx42,Jx43, &
  Jy12,Jy13,Jy14,J21,Jy23,Jy24, Jy31, Jy32, Jy34, Jy41, Jy42, &
  Jy43, Jz12, Jz13, Jz14, Jz21, Jz23, Jz24, Jz31, Jz32, Jz34, &
  Jz41, Jz42, Jz43, Jy21
```

integer i,j,k, m, col

```
! OPEN(8, FILE = "D:\Ifaz\Study2muscle\FemurFracture\uelDama
! &ge\DEBUG.txt", ACCESS = 'APPEND')
```

```
! WRITE(8,*) "starting Bqad"
! WRITE(8,*) "NodeCoords"
! WRITE(8,*) NodeCoords(1,1),NodeCoords(1,2),NodeCoords(1,3)
! WRITE(8,*) "NatCoords"
! WRITE(8,*) NatCoords
```

```
! Close(8)
```

```
! example contents dNdx = [dN1dx dN2dx dN3dx ..... dN10dx]
```

$$Jx1=4.0*(NodeCoords(1,1)*(NatCoords(1)-0.25)+NodeCoords(5,1)*NatCoords(2)+NodeCoords(7,1)*NatCoords(3)+NodeCoords(8,1)*NatCoords(4))$$
$$Jy1=4.0*(NodeCoords(1,2)*(NatCoords(1)-0.25)+NodeCoords(5,2) * NatCoords(2)+NodeCoords(7,2)*NatCoords(3)+NodeCoords(8,2)*NatCoords(4))$$
$$Jz1=4.0*(NodeCoords(1,3)*(NatCoords(1)-0.25)+NodeCoords(5,3) * NatCoords(2)+NodeCoords(7,3)*NatCoords(3)+NodeCoords(8,3)*NatCoords(4))$$
$$Jx2=4.0*(NodeCoords(5,1)*NatCoords(1)+NodeCoords(2,1)*(NatCoords(2)-0.25)+NodeCoords(6,1)*NatCoords(3)+NodeCoords(9,1)*NatCoords(4))$$
$$Jy2=4.0*(NodeCoords(5,2)*NatCoords(1)+NodeCoords(2,2)*(NatCoords(2)-0.25)+NodeCoords(6,2)*NatCoords(3)+NodeCoords(9,2)*NatCoords(4))$$
$$Jz2=4.0*(NodeCoords(5,3)*NatCoords(1)+NodeCoords(2,3)*(NatCoords(2)-0.25)+NodeCoords(6,3)*NatCoords(3)+NodeCoords(9,3)*NatCoords(4))$$
$$Jx3=4.0*(NodeCoords(7,1)*NatCoords(1)+NodeCoords(6,1)*NatCoords(2)+NodeCoords(3,1)*(NatCoords(3)-0.25)+NodeCoords(10,1)*NatCoords(4))$$
$$Jy3=4.0*(NodeCoords(7,2)*NatCoords(1)+NodeCoords(6,2)*NatCoords(2)+NodeCoords(3,2)*(NatCoords(3)-0.25)+NodeCoords(10,2)*NatCoords(4))$$
$$Jz3=4.0*(NodeCoords(7,3)*NatCoords(1)+NodeCoords(6,3)*NatCoords(2)+NodeCoords(3,3)*(NatCoords(3)-0.25)+NodeCoords(10,3)*NatCoords(4))$$

```
Jx4=4.0*(NodeCoords(8,1)*NatCoords(1)+NodeCoords(9,1)*NatCoords(2)+NodeCoords(10,1)
*NatCoords(3)+NodeCoords(4,1)*(NatCoords(4)-0.25))
```

```
Jy4=4.0*(NodeCoords(8,2)*NatCoords(1)+NodeCoords(9,2)*NatCoords(2)+NodeCoords(10,2)
*NatCoords(3)+NodeCoords(4,2)*(NatCoords(4)-0.25))
```

```
Jz4=4.0*(NodeCoords(8,3)*NatCoords(1)+NodeCoords(9,3)*NatCoords(2)+NodeCoords(10,3)
*NatCoords(3)+NodeCoords(4,3)*(NatCoords(4)-0.25))
```

```
! OPEN(8, FILE = "D:\Ifaz\Study2muscle\FemurFracture\uelDama
! &ge\block\DEBUG.txt", ACCESS = 'APPEND')
```

```
! WRITE(8,*) "Jz defined"
```

```
! Close(8)
```

```
Jx12=Jx1-Jx2
```

```
Jx13=Jx1-Jx3
```

```
Jx14=Jx1-Jx4
```

```
Jx23=Jx2-Jx3
```

```
Jx24=Jx2-Jx4
```

```
Jx34=Jx3-Jx4
```

```
Jy12=Jy1-Jy2
```

```
! OPEN(8, FILE = "D:\Ifaz\Study2muscle\FemurFracture\uelDama
! &ge\DEBUG.txt", ACCESS = 'APPEND')
```

```
! WRITE(8,*) "Jy12", Jy12
```

```
! Close(8)
```

```
Jy13=Jy1-Jy3
```

```
Jy14=Jy1-Jy4
```

```
Jy23=Jy2-Jy3
```

```
Jy24=Jy2-Jy4
```

```
Jy34=Jy3-Jy4
```

```
Jz12=Jz1-Jz2
```

```
Jz13=Jz1-Jz3
```

```
Jz14=Jz1-Jz4
```

```
Jz23=Jz2-Jz3
```

```
Jz24=Jz2-Jz4
```

```
Jz34=Jz3-Jz4
```

```
! OPEN(8, FILE = "D:\Ifaz\Study2muscle\FemurFracture\uelDama
```

```

! &ge\DEBUG.txt", ACCESS = 'APPEND')

!     WRITE(8,*) "Jz34", Jz34
!     Close(8)

Jx21=-1.0*Jx12
Jx31=-1.0*Jx13
Jx41=-1.0*Jx14
Jx32=-1.0*Jx23

Jx42=-1.0*Jx24
Jx43=-1.0*Jx34
Jy21=-1.0*Jy12
Jy31=-1.0*Jy13
Jy41=-1.0*Jy14
Jy32=-1.0*Jy23
Jy42=-1.0*Jy24

! OPEN(8, FILE = "D:\Ifaz\Study2muscle\FemurFracture\uelDama
! &ge\DEBUG.txt", ACCESS = 'APPEND')

!     WRITE(8,*) "Jy42", Jy42
!     Close(8)

Jy43=-1.0*Jy34
Jz21=-1.0*Jz12
Jz31=-1.0*Jz13
Jz41=-1.0*Jz14
Jz32=-1.0*Jz23
Jz42=-1.0*Jz24
Jz43=-1.0*Jz34

! OPEN(8, FILE = "D:\Ifaz\Study2muscle\FemurFracture\uelDama
! &ge\DEBUG.txt", ACCESS = 'APPEND')

!     WRITE(8,*) "Jz43", Jz43
!     Close(8)

Jdet=Jx21*(Jy23*Jz34-Jy34*Jz23)+Jx32*(Jy34*Jz12-Jy12*Jz34)+Jx43*(Jy12*Jz23 -
Jy23*Jz12)

! OPEN(8, FILE = "D:\Ifaz\Study2muscle\FemurFracture\uelDama
! &ge\DEBUG.txt", ACCESS = 'APPEND')

```

```

!      WRITE(8,*) "Jdet", Jdet
!      Close(8)

! calculate shape function derivatives

a(1)=Jy42*Jz32-Jy32*Jz42
a(2)=Jy31*Jz43-Jy34*Jz13
a(3)=Jy24*Jz14-Jy14*Jz24
a(4)=Jy13*Jz21-Jy12*Jz31

b(1)=Jx32*Jz42-Jx42*Jz32
b(2)=Jx43*Jz31-Jx13*Jz34
b(3)=Jx14*Jz24-Jx24*Jz14
b(4)=Jx21*Jz13-Jx31*Jz12

c(1)=Jx42*Jy32-Jx32*Jy42
c(2)=Jx31*Jy43-Jx34*Jy13
c(3)=Jx24*Jy14-Jx14*Jy24
c(4)=Jx13*Jy21-Jx12*Jy31

! OPEN(8, FILE = "D:\Ifaz\Study2muscle\FemurFracture\uelDama
! &ge\DEBUG.txt", ACCESS = 'APPEND')

!      WRITE(8,*) "c(4)", c(4)
!      Close(8)

! -----x-----
dNdx(1) =(4.0*NatCoords(1)-1.0)*a(1)/Jdet
dNdx(2)= (4.0*NatCoords(2)-1.0)*a(2)/Jdet
dNdx(3)= (4.0*NatCoords(3)-1.0)*a(3)/Jdet
dNdx(4)= (4.0*NatCoords(4)-1.0)*a(4)/Jdet

dNdx(5) = (a(1)*NatCoords(2)+a(2)*NatCoords(1) )*(4.0/Jdet)
dNdx(6) = (a(2)*NatCoords(3)+a(3)*NatCoords(2) )*(4.0/Jdet)
dNdx(7) = (a(3)*NatCoords(1)+a(1)*NatCoords(3) )*(4.0/Jdet)
dNdx(8) = (a(1)*NatCoords(4)+a(4)*NatCoords(1) )*(4.0/Jdet)
dNdx(9) = (a(2)*NatCoords(4)+a(4)*NatCoords(2) )*(4.0/Jdet)
dNdx(10)= (a(3)*NatCoords(4)+a(4)*NatCoords(3) )*(4.0/Jdet)

! -----y-----
dNdy(1) =(4.0*NatCoords(1)-1.0)*b(1)/Jdet
dNdy(2)= (4.0*NatCoords(2)-1.0)*b(2)/Jdet
dNdy(3)= (4.0*NatCoords(3)-1.0)*b(3)/Jdet
dNdy(4)= (4.0*NatCoords(4)-1.0)*b(4)/Jdet

```

```

dNdy(5) = (b(1)*NatCoords(2)+b(2)*NatCoords(1) )*( 4.0/Jdet)
dNdy(6) = (b(2)*NatCoords(3)+b(3)*NatCoords(2) )*( 4.0/Jdet)
dNdy(7) = (b(3)*NatCoords(1)+b(1)*NatCoords(3) )*( 4.0/Jdet)
dNdy(8) = (b(1)*NatCoords(4)+b(4)*NatCoords(1) )*( 4.0/Jdet)
dNdy(9) = (b(2)*NatCoords(4)+b(4)*NatCoords(2) )*( 4.0/Jdet)
dNdy(10) = (b(3)*NatCoords(4)+b(4)*NatCoords(3) )*( 4.0/Jdet)

```

```
! -----z-----
```

```

dNdz(1) =(4.0*NatCoords(1)-1.0)*c(1)/Jdet
dNdz(2)= (4.0*NatCoords(2)-1.0)*c(2)/Jdet
dNdz(3)= (4.0*NatCoords(3)-1.0)*c(3)/Jdet
dNdz(4)= (4.0*NatCoords(4)-1.0)*c(4)/Jdet

```

```

dNdz(5) = (c(1)*NatCoords(2)+c(2)*NatCoords(1) )*( 4.0/Jdet)
dNdz(6) = (c(2)*NatCoords(3)+c(3)*NatCoords(2) )*( 4.0/Jdet)
dNdz(7) = (c(3)*NatCoords(1)+c(1)*NatCoords(3) )*( 4.0/Jdet)
dNdz(8) = (c(1)*NatCoords(4)+c(4)*NatCoords(1) )*( 4.0/Jdet)
dNdz(9) = (c(2)*NatCoords(4)+c(4)*NatCoords(2) )*( 4.0/Jdet)
dNdz(10) = (c(3)*NatCoords(4)+c(4)*NatCoords(3) )*( 4.0/Jdet)

```

```
! OPEN(8, FILE = "D:\Ifaz\Study2muscle\FemurFracture\uelDama
! &ge\DEBUG.txt", ACCESS = 'APPEND')
```

```
! WRITE(8,*) "dNdz(10)", dNdz(10)
! Close(8)
```

```
! Build B matrix
```

```

Do i=1,6
Do j=1,30
Bmatrix(i,j)=0
End do
End do

```

```
Do m=1,10
```

```

col=(3.0*(m-1) )+1.0
Bmatrix(1, col) = dNdx(m)
Bmatrix(2, col+1) = dNdy(m)
Bmatrix(3, col+2) = dNdz(m)

```

```
Bmatrix(4, col) =dNdy(m)
```

```
Bmatrix(4, col+1) = dNdx(m)
```

```
Bmatrix(5, col+1) = dNdz(m)
```

```
Bmatrix(5, col+2) = dNdy(m)
```

```
Bmatrix(6, col) = dNdz(m)
```

```
Bmatrix(6, col+2) = dNdx(m)
```

```
End Do
```

```
! OPEN(8, FILE = "D:\Ifaz\Study2muscle\FemurFracture\uelDama  
! &ge\DEBUG.txt", ACCESS = 'APPEND')
```

```
! WRITE(8,*) "Bmatrix(1,1):"
```

```
! WRITE(8,*) Bmatrix
```

```
! Close(8)
```

```
RETURN
```

```
END
```

## Appendix B: Mesh Sensitivity

A mesh sensitivity study was performed in order to determine an adequate mesh density for the specimen-specific models used in Chapters 5 and 6. Specimen 6 was randomly selected for this investigation. Three models were created, with an average tetrahedral element edge length of 3.5 mm, 2.5 mm, and 1.5 mm, resulting in models with 25 000, 61 000, and 130 000 elements, respectively (Figure B-1). To conserve computational resources, mesh refinement was limited to the head-neck region. Outside this region, strain gradients were quite moderate and damage evolution did not occur.

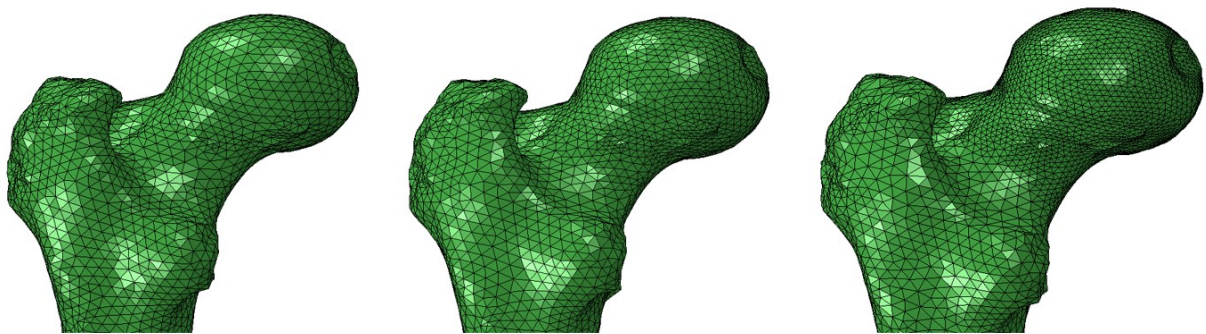


Figure B-1 Specimen 6 modeled with three different mesh densities. Average edge length in the head-neck region was 3.5 mm (LEFT), 2.5 mm (MIDDLE) and 1.5 mm (RIGHT). The final meshes had 25 000, 61 000, and 130 000 elements, respectively.

As shown in Figure B-2 **Error! Reference source not found.**, this study found that the 61 000 element (2.5 mm average edge length) model was sufficient, as further refinement resulted in minimal changes to predicted fracture load (<2%).

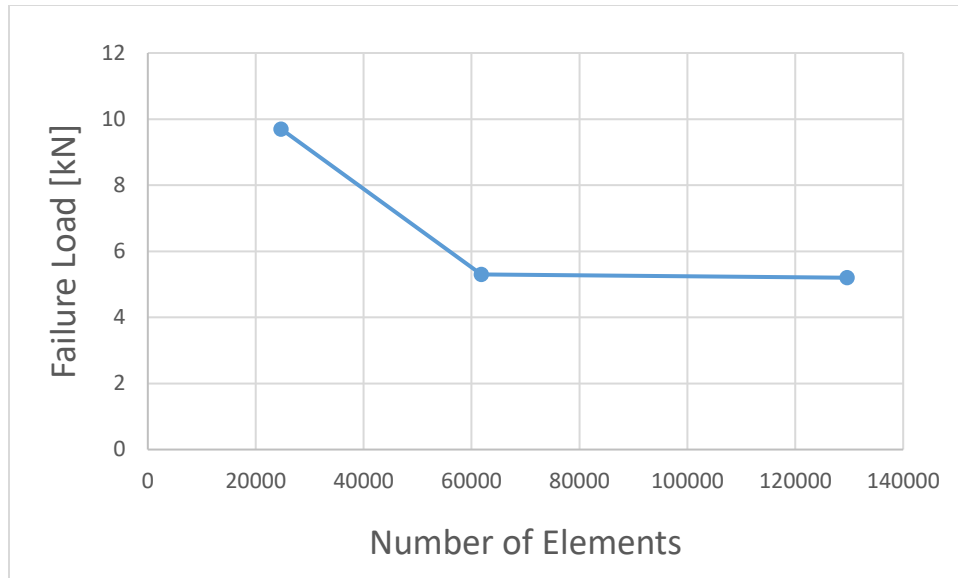


Figure B-2 Influence of mesh refinement on FE predicted fracture load. Refinement beyond 61 000 elements (average edge length 2.5 mm) resulted in only minor differences to FE predicted fracture load (<2% difference).

## Appendix C: Visualized Damage Patterns from Repeated Loading Scenarios

The Figures below show visualized damage accumulation and fracture patterns from the repeated loading scenarios discussed in greater detail in Section 6.2.2 and 6.3.2.

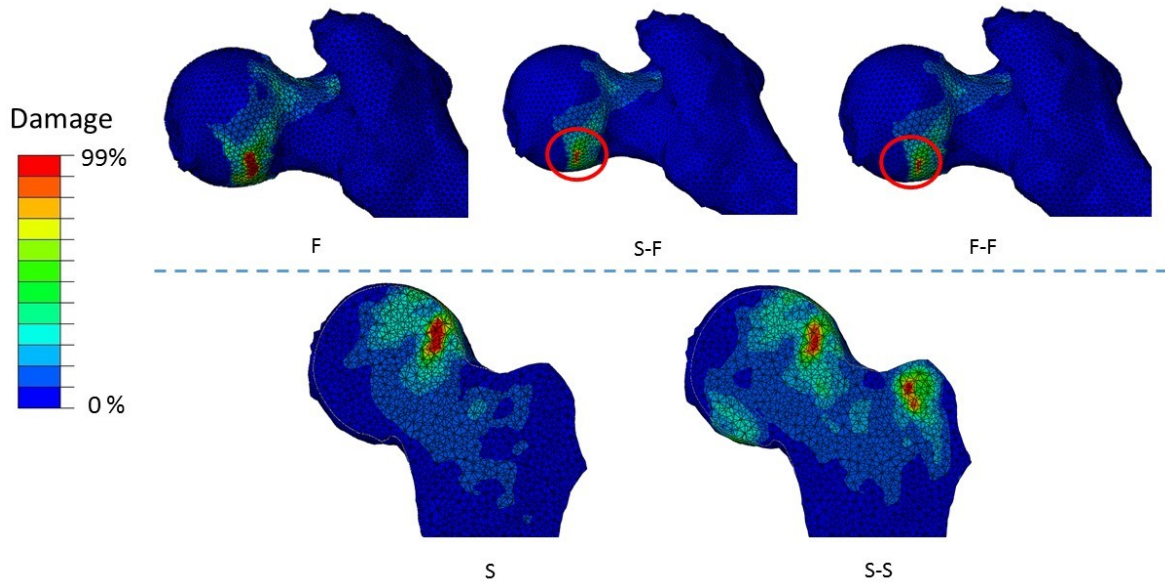


Figure C-1 Damage accumulation patterns for Specimen 1. Fracture from a single fall event (TOP LEFT) resulted in a crack along the inferior subcapital region. This pattern was also seen in the compound loading cases S-F (TOP MIDDLE) and F-F (TOP RIGHT), but the model failed to converge at a smaller overall crack size. When loaded to failure from a single stumbling event (BOTTOM LEFT), the femur experienced a crack in the superior subcapital region. A similar pattern of damage was seen in the compound load case S-S (BOTTOM RIGHT), but additional damage was observed near the greater trochanter and the inferior aspect of the neck.

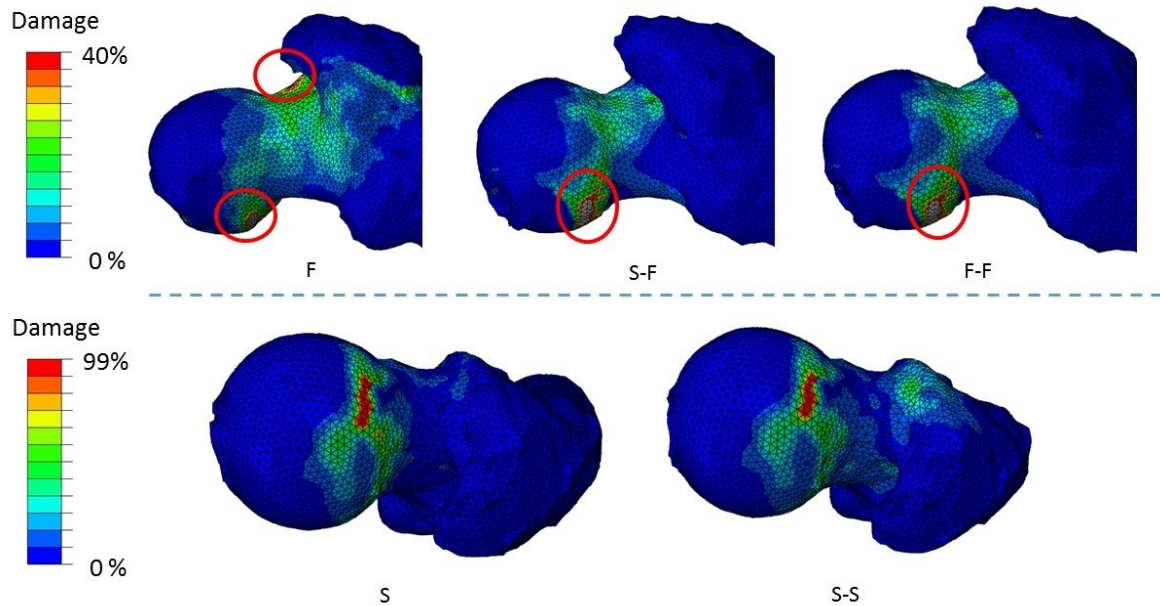


Figure C-2 Damage accumulation patterns for Specimen 2. Fracture from a single fall event (TOP LEFT) resulted in high damage at the inferior subcapital region and the superior aspect of the femoral neck. Similar damage patterns were observed during compound load cases S-F (TOP MIDDLE) and F-F (TOP RIGHT). However, damage in the superior aspect of the neck was less severe. When loaded to failure from a single stumbling event (BOTTOM LEFT), the femur experienced a crack in the superior subcapital region. A similar pattern of damage was seen in the compound load case S-S (BOTTOM RIGHT).

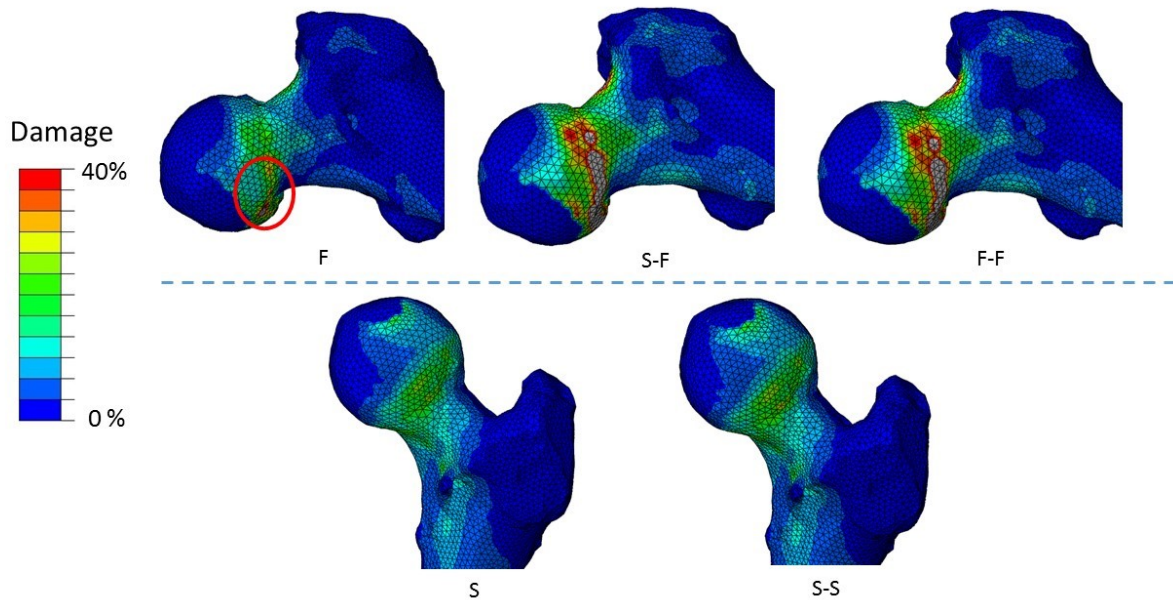


Figure C-3 Damage accumulation patterns for Specimen 3. Fracture from a single fall event (TOP LEFT) resulted in high damage at the inferior subcapital region. Similar damage patterns were observed during compound load cases S-F (TOP MIDDLE) and F-F (TOP RIGHT), but damage progressed to a much greater extent. However, this resulted in minimal changes to peak load (Figure 39). When loaded to failure from a single stumbling event (BOTTOM LEFT), only minimal surface damage was predicted, in the superior-anterior subcapital region. The damage pattern was nearly identical in the compound load case S-S (BOTTOM RIGHT).

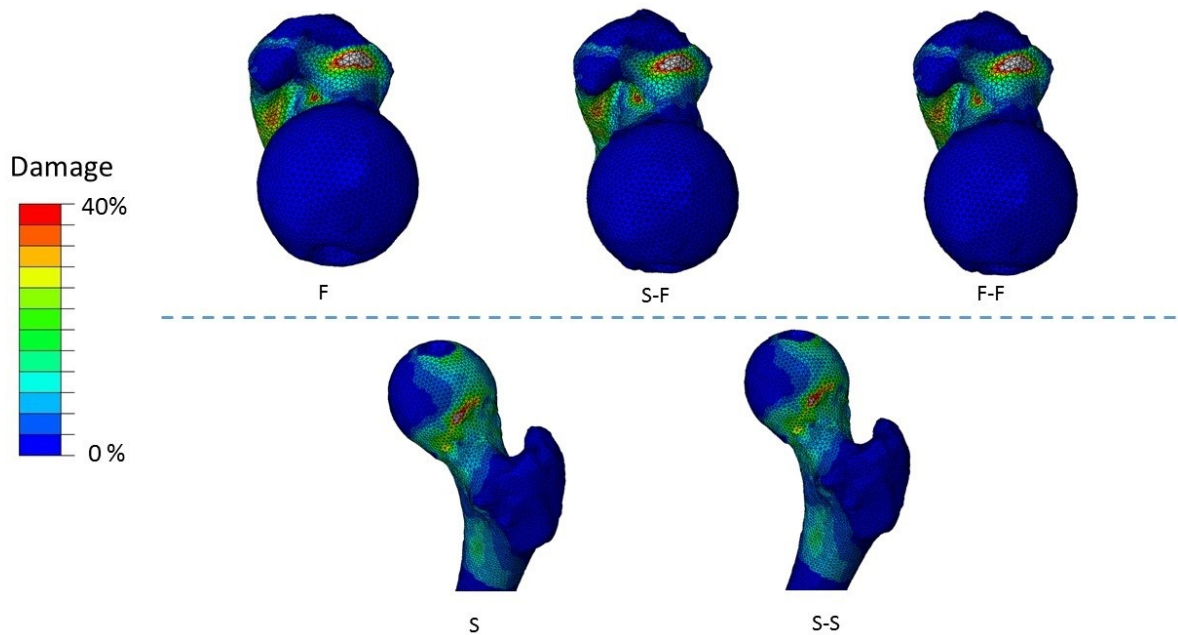


Figure C-4 Damage accumulation patterns for Specimen 4. Fracture from a single fall event (TOP LEFT) resulted in high damage in the superior aspect of the neck. Nearly identical damage patterns were observed during compound load cases S-F (TOP MIDDLE) and F-F (TOP RIGHT). When loaded to failure from a single stumbling event (BOTTOM LEFT), damage occurred in the superior subcapital region. Again, the damage pattern from the compound load case S-S (BOTTOM RIGHT) was nearly identical.

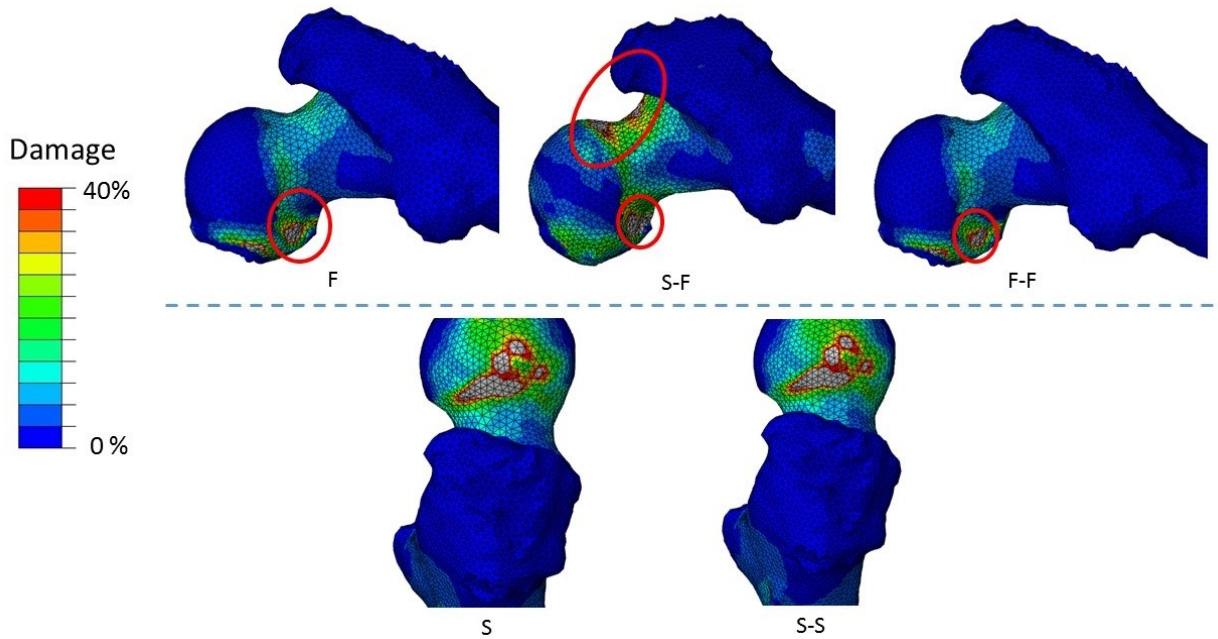


Figure C-5 Damage accumulation patterns for Specimen 5. Fracture from a single fall event (TOP LEFT) resulted in high damage to the inferior aspect of the neck, with a nearly identical damage pattern in compound load case F-F (TOP RIGHT). However, the pattern of damage changed significantly in load case S-F (TOP MIDDLE), which also suffered damage to the superior subcapital region and superior aspect of the neck. When loaded to failure from a single stumbling event (BOTTOM LEFT), damage occurred in the superior subcapital region, and the damage pattern from the compound load case S-S (BOTTOM RIGHT) was nearly identical.

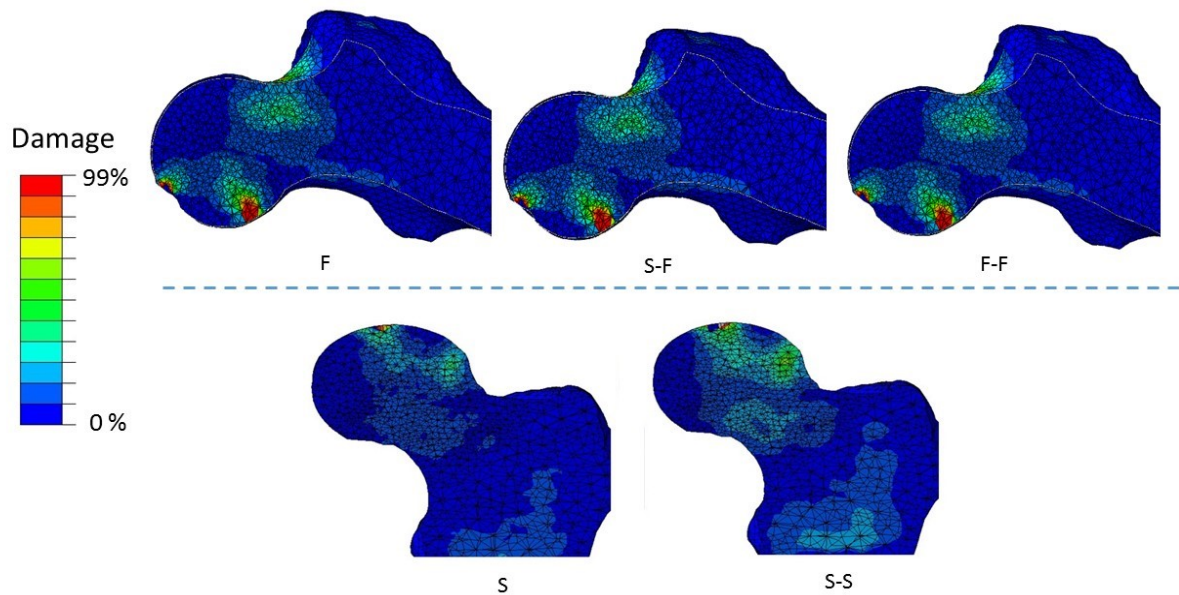


Figure C-6 Damage accumulation patterns for Specimen 6. Fracture from a single fall event (TOP LEFT) resulted in high damage to the inferior aspect of the neck, with some additional damage of the superior femoral neck. Nearly identical damage patterns were predicted from the compound load cases S-F (TOP MIDDLE) and F-F (TOP RIGHT). When loaded to failure from a single stumbling event (BOTTOM LEFT), damage occurred in the superior subcapital region. However, the compound load case S-S (BOTTOM RIGHT) experienced additional damage to the inferior subcapital region.

## Appendix D: Musculoskeletal Model Results

This Appendix discusses the results of the musculoskeletal model, first described in section 4.3.1, used to estimate muscle forces during stumbling. For the reader's convenience, results have been separated into two tables. Table D-1 reports computed forces for all muscles that cross the hip joint. As expected, a large number of muscles were active during stumbling. Bergman hypothesized that large hip contact force during stumbling was due to co-contraction of the hip muscles, as an attempt to stabilize the joint. These findings are consistent with this hypothesis. Large forces were predicted in 19 of the 28 muscles, where the predicted force was greater than 40% of the maximum force achievable by the muscle.

Table D-1 Summary of predicted forces, in muscles that cross the hip. As expected, forces were large in 16 of 21 muscles (>40% of max achievable force).

<b>Muscle Name</b>	<b>Predicted Force [N]</b>	<b>Maximum Achievable Force [N]</b>	<b>Percent of Max Force</b>
<b>Gluteus Medius (Anterior Compartment)</b>	415	546	76%
<b>Gluteus Medius (Middle Compartment)</b>	244	382	64%
<b>Gluteus Medius (Posterior Compartment)</b>	367	435	84%
<b>Gluteus Minimus (Anterior Compartment)</b>	59	180	33%
<b>Gluteus Minimus (Middle Compartment)</b>	84	190	44%
<b>Gluteus Minimus (Posterior Compartment)</b>	152	215	71%
<b>Biceps Femoris (Long Head)</b>	567	717	79%
<b>Adductor Longus</b>	399	418	95%
<b>Adductor Brevis</b>	239	286	83%
<b>Adductor Magnus (Superior Component)</b>	346	346	100%

<b>Adductor Magnus (Middle Component)</b>	308	312	99%
<b>Adductor Magnus (Inferior Component)</b>	274	444	62%
<b>Pectineus</b>	84	177	47%
<b>Gluteus Maximus (Superior Component)</b>	368	382	96%
<b>Gluteus Maximus (Middle Component)</b>	352	546	64%
<b>Gluteus Maximus (Inferior Component)</b>	348	368	95%
<b>Iliacus</b>	34	429	8%
<b>Psoas</b>	127	371	34%
<b>Quadratus Femoris</b>	63	254	25%
<b>Gemelli</b>	17	109	16%
<b>Periformis</b>	296	296	100%
<b>Rectus Femoris</b>	0	779	0%
<b>Tensor Facia Latae</b>	35	155	23%
<b>Gracilis</b>	17	108	16%
<b>Semimembranosus</b>	692	1030	67%
<b>Semitendinosus</b>	141	328	43%
<b>Bicep Femoris (Long Head)</b>	347	717	48%
<b>Sartorius</b>	9	104	9%

Table D-2 summarizes the predicted forces in the remaining muscles. These values are somewhat more difficult to validate, as stumbling configurations have not been closely considered in the past. It was somewhat surprising that many muscles had little to no predicted force. These

results, however, are consistent with the findings reported by Crowninshield and Brand [55] who predicted similar patterns during the mid-stance phase of gait.

Table D-2 Summary of predicted forces, in muscles that do not cross the hip. As expected, forces were large in 16 of 21 muscles (>40% of max achievable force).

<b>Muscle Name</b>	<b>Predicted Force [N]</b>	<b>Maximum Achievable Force [N]</b>	<b>Percent of Max Force</b>
<b>Vastus Lateralis</b>	0	1871	0
<b>Vastus Intermedius</b>	0	1365	0
<b>Vastus Medialis</b>	0	1294	0
<b>Bicep Femoris (Short Head)</b>	37	402	9
<b>Peroneus Tertius</b>	0	90	0
<b>Peroneus Longus</b>	0	754	0
<b>Peroneus Brevis</b>	192	348	55
<b>Tibialis Anterior</b>	173	603	29
<b>Tibialis Posterior</b>	202	1270	16
<b>Soleus</b>	447	2839	16
<b>Gastrocnemius (Lateral Head)</b>	0	488	0
<b>Gastrocnemius (Medial Head)</b>	412	1113	37
<b>Extensor Hallucis Longus</b>	0	108	0
<b>Extensor Digitorum Longus</b>	36	341	11
<b>Flexor Hallucis Longus</b>	30	322	9
<b>Flexor Digitorus Longus</b>	47	310	15

## Appendix E: Specimen Alignment using Optical Motion Tracking

This Appendix described the practical implantation of the novel specimen alignment procedure first described in Section 4.2.2, which used optical motion tracking equipment to identify specimen alignment in real-time.

The motion tracking system used an infrared camera to track a rigid body marker, which was secured to the femur using dental floss and cyanoacrylate (Figure E-1). A second marker with a probe tip, known as a digitizing probe, was used to identify the location of important bone landmarks relative to the secured ridged body marker. This procedure required landmarks on the proximal femur, only (Figure E-2). Points were selected on the femoral head (15 points), the thinnest part of the neck (8 points), and two planes of the shaft (8 points each). The camera tracks the position and rotation of the attached rigid body marker, from which the system reports the position of each digitized landmark. A custom Matlab script was written to stream this data in real-time. As described in Section 4.2.2, these points were used to identify the neck and shaft axis, from which specimen orientation was identified and reported to the user. For the reader's convenience, a copy of the Matlab script is included at the end of this Appendix. However, significant credit goes to Suzan Bsat, a doctoral candidate who coded a similar algorithm to track the motion of acetabular specimens. Only minor modifications were made to adopt the code for this research.

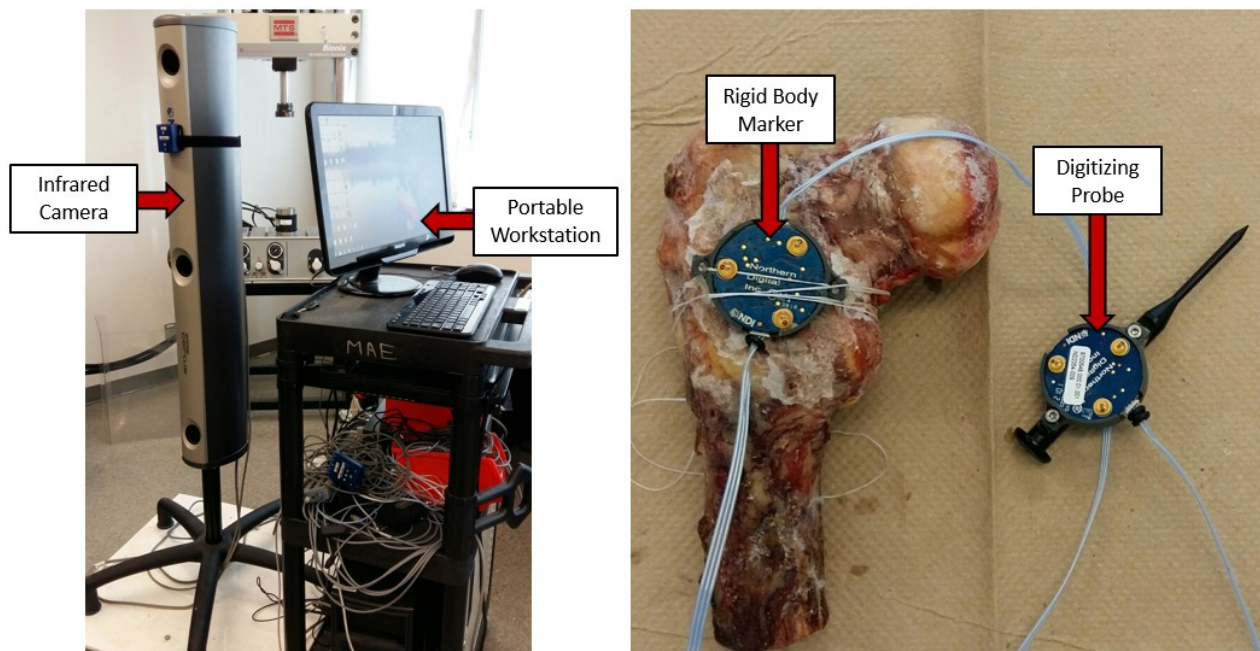


Figure E-1 Equipment used for specimen alignment. The infrared camera (LEFT) tracks the motion of a ridged body marker secured to the test specimen (MID-RIGHT). A digitizing probe (RIGHT) was used to identify the locations of femoral landmarks relative to the ridged body marker.

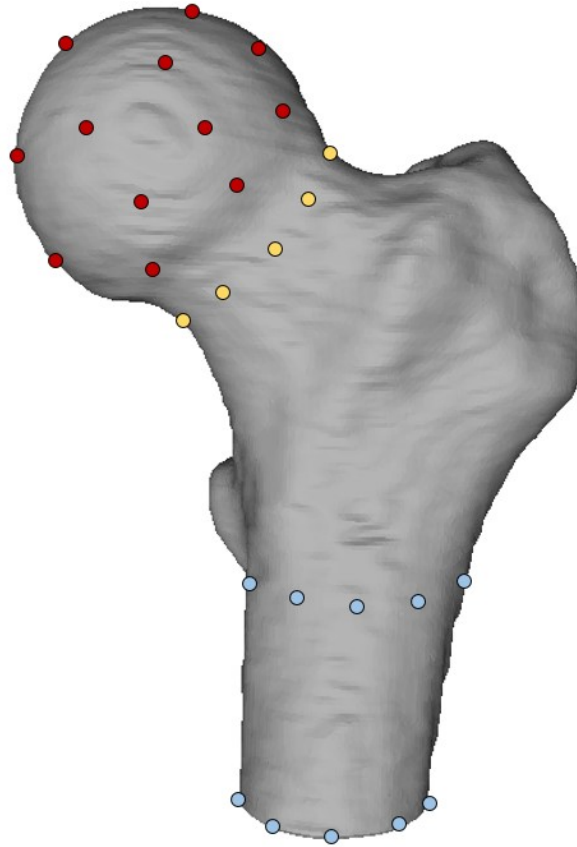


Figure E-2 Schematic representation of landmark selection. Points were selected on the femoral head (RED), femoral neck (YELLOW), and two planes of the femoral shaft (BLUE). Some landmark selections are hidden.

### Matlab Code Used To Stream Specimen Alignment in Real-Time

```

%% Real Time Data Stream Plotting Example
function real_time_data_stream_plotting_femur
%%
% This example demonstrates how to automatically read a set number of data bytes as and
% when they are available. This MATLAB(R) script also generates a real time plot of streaming
% data collected from the TCPIP server.
%
% The script may be updated to use any instrument/device/TCPIP server
% to collect real time data. You may need to update the IP address and
% port.
%
% To generate a report of this entire script, you may use the PUBLISH
% command at the MATLAB(R) command line as follows:

```

```

%
% publish(real_time_data_plot);

% Author: Ankit Desai
% Copyright 2010 - The MathWorks, Inc.

% motified for First Principles by Melanie Scholz, 2010, Northern Digital Inc

%% Create the interface object

interfaceObject = tcpip('optotrakmae',3020);
set (interfaceObject, 'InputBufferSize',5000);
%%
% Setup a figure window and define a callback function for close operation
figureHandle = figure('NumberTitle','off',...
    'Name','Live Data Stream Plot',...
    'Color',[0 0 0],...
    'CloseRequestFcn',{@localCloseFigure,interfaceObject});

%%
% Setup the axes
axesHandle = axes('Parent',figureHandle,...
    'YGrid','on',...
    'YColor',[0.9725 0.9725 0.9725],...
    'XGrid','on',...
    'XColor',[0.9725 0.9725 0.9725],...
    'Color',[0 0 0]);
set(gca, 'XTick',1:2, 'XTickLabel',{'AV' 'AB'})

xlabel(axesHandle,'Orientation');
ylabel(axesHandle,'Angle');

%%
% Initialize the plot and hold the settings on
hold on;
plotHandle = plot(axesHandle,0,'og','LineWidth',1);

%% Setup interface object to read chunks of data
% Set the number of bytes to read at a time
bytesToRead = 500;

%%
% Define a callback function to be executed when desired number of bytes
% are available in the input buffer
interfaceObject.BytesAvailableFcn = {@localReadAndPlot,plotHandle,bytesToRead};
interfaceObject.BytesAvailableFcnMode = 'byte';

```

```

interfaceObject.BytesAvailableFcnCount = bytesToRead;

%%
% Open the interface object
fopen(interfaceObject);
%fwrite (interfaceObject, fpcommand('SendCurrentFrame AllFrames All'),'uint8');
fwrite (interfaceObject, fpcommand('StreamFrames AllFrames all'),'uint8');

pause(3);
snapnow;

%% Implement the bytes available callback
function localReadAndPlot(interfaceObject,~,figureHandle,bytesToRead)

%%
% Read the desired number of data bytes

%data = fread(interfaceObject,bytesToRead);
header =fread(interfaceObject,4);
size=swapbytes(typecast(uint8(header(1:4)),'uint32'));
size=double(size);
packet = fread(interfaceObject,size-4);

out=readpacket([header; packet]);
% out=readpacket([header; packet]);
%

%digitize B1, B2, B3 (global CS)
%Attach 1 RB to the femur and record data for 10s at 100Hz
%Attach 1 RB as the probe

%there are 3 markers/RB
%3d data output/marker: x y z residual
%There are 3 markers- probe, femur
%3d Data- 1-4 (Marker 1) 5-8 (Marker 2) 9-12 (Marker 3) 13-16 (Marker 4) 17-20
%(Marker 5) 21-24 (Marker 6) 25-84 (1-15 femoral head) 85-116 (1-8 neck) 117-148 (1-8 shaft
1)
%149-180 (1-8 shaft 2)

%6d data output/RB: Qo Qx Qy Qz x y z error
%to get the rotation matrix convert quaternion

data1=0;
angles=0;
CS=0;
if packet(4)==3 %data packet

```

```

    data1=out.data3d; %can be data3d, data6d or analog
%%
%Calculating Spherefit
%points around the rim of the acetabulum
%Pts is a mx3 array (m points, one point per row, 3 columns)
    X=[data1(25:27)'; data1(29:31)'; data1(33:35)'; data1(37:39)'; data1(41:43)'; data1(45:47)';
data1(49:51)'; data1(53:55)'; data1(57:59)'; data1(61:63)'; data1(65:67)'; data1(69:71)';
data1(73:75)'; data1(77:79)';data1(81:83)'];

    % Input:
% X: n x 3 matrix of cartesian data
% Outputs:
% Center: Center of sphere
% Radius: Radius of sphere
% Author:
% Alan Jennings, University of Dayton

A=[mean(X(:,1).*(X(:,1)-mean(X(:,1))))), ...
    2*mean(X(:,1).*(X(:,2)-mean(X(:,2))))), ...
    2*mean(X(:,1).*(X(:,3)-mean(X(:,3))))); ...
    0, ...
    mean(X(:,2).*(X(:,2)-mean(X(:,2))))), ...
    2*mean(X(:,2).*(X(:,3)-mean(X(:,3))))); ...
    0, ...
    0, ...
    mean(X(:,3).*(X(:,3)-mean(X(:,3))))];
A=A+A.';
B=[mean((X(:,1).^2+X(:,2).^2+X(:,3).^2).*(X(:,1)-mean(X(:,1)))));...
    mean((X(:,1).^2+X(:,2).^2+X(:,3).^2).*(X(:,2)-mean(X(:,2)))));...
    mean((X(:,1).^2+X(:,2).^2+X(:,3).^2).*(X(:,3)-mean(X(:,3))))];
sphCenter=(A\B).'; %Sphere center

%%

% Circle fit for neck

p1=[data1(85:87)'; data1(89:91)'; data1(93:95)'; data1(97:99)'; data1(101:103)'; data1(105:107)';
data1(109:111)'; data1(113:115)'];
centern=mean(p1,1);

%%
%Circle fit 1 for shaft

```

```

p2=[data1(117:119)'; data1(121:123)'; data1(125:127)'; data1(129:131)'; data1(133:135)';
data1(137:139)'; data1(141:143)'; data1(145:147)'];

centers1=mean(p2,1);
%%
%Circle fit 2 for shaft

p3=[data1(149:151)'; data1(153:155)'; data1(157:159)'; data1(161:163)'; data1(165:167)';
data1(169:171)'; data1(173:175)'; data1(177:179)'];

centers2=mean(p3,1);
%%
%Calculating shaft angle AD and AV

NA= sphCenter-centern; %neck axis
AV=atan(NA(3)/NA(1)); %anteversion
AD=atan (NA(2)/NA(1)); %adduction

SA=centers1-centers2; %shaft axis
FE=atan(SA(3)/SA(2)); %flex-ext

angles=[(AV*180/pi) (AD*180/pi) (FE*180/pi)] %desired for neutral [12 45 9]
          %desired for stumbling [8 64 16]

fid2=fopen('anglefemur.txt','a');
fprintf(fid2,'%f\n',angles);
fclose (fid2);

end

% out.data3d is a vector with all the marker x y z data piled on top
% of each other [x1 y1 z1 r1 x2 y2 z2 r2 ...], see RTC3D protocol. similar
% for out.data6d and out.analog.
%RB6

%%
% Update the plot
set(figureHandle,'Ydata',angles);
%set(figureHandle,'Ydata',out);

%% Implement the close figure callback

```

```
function localCloseFigure(figureHandle,~,interfaceObject)
%%
% Clean up the interface object
fclose(interfaceObject);
delete(interfaceObject);
clear interfaceObject;
%%
% Close the figure window
delete(figureHandle);
```